ANNUAL REPORT

April 1,2002 – March 31, 2003

TANDEM ACCELERATOR CENTER
UNIVERSITY OF TSUKUBA

http://www.tac.tsukuba.ac.jp/

PREFACE

This annual report describes research activities in UTTAC during the period from April 2002 to March 2003. The 12UD Pelletron tandem accelerator was successfully operated until the end of February 2003. Total beam time used for experiments was 1663 hours. During the scheduled maintenance performed at the end of March 2003, the structure in the terminal stripping channel was modified to improve the performance of the AMS system. A new project was initiated with the 1 MV tandetron accelerator. It is aimed at the investigation of interaction between low-energy cluster ions and atoms or molecules at the surface of materials. Carbon cluster ions Cn (n ≤ 8) were successfully extracted at 20 keV/amu with intensities sufficiently available in experiment.

In nuclear physics, investigations were continued on the proton polarization in the $^{208}Pb(d,p)^{209}Pb_{gs}$ reaction at 20 MeV, the analyzing powers in the $^{6}Li(d,p)^{7}Li$ reaction at 90 keV, the total-reaction cross section for protons on Si nuclei near the (p,n) threshold and CDCC analysis. Measurements of spin-correlation parameters with a polarized-deuteron target and polarized-deuteron beam were started in collaboration with Nagoya University.

Steady progress was made on ion- and cluster-induced secondary electron spectroscopy, the charge state of heavy ions through Be, atomic cluster physics, NMR studies on electronic states of $3d$ transition-metal oxides, Moessbauer experiments and the elastic property of metals after proton irradiation. A new technique was developed on the production of 3D nano-structures with heavy ion bombardment on TiO_2.

The microprobe system for hydrogen analysis was finished. The measurement of the hydrogen concentration in melt inclusions was initiated for samples taken at some places near Zao volcano in Miyagi prefecture Japan. The final data for the neutron dosimetry of Hiroshima atomic bomb provided by our AMS group were in good agreement with data reported by Munich and Livermore groups, and with the results obtained from residual activity measurements. The measurement of [36]Cl produced in concrete shields of various accelerator facilities began as a new subject of AMS.

The director of the Tandem Accelerator Center changed from Prof. Kohei Furuno to Prof. Hiroshi Kudo on April 1, 2003.

Kohei Furuno

K. Furuno

CONTENTS

1. ACCELERATOR AND EXPERIMENTAL FACILITIES

2. NUCLEAR PHYSICS

3. ATOMIC AND SOLID STATE PHYSICS, AND CLUSTER SCIENCE

4. ION BEAM APPLICATION

1.1 Accelerator operation 2002

K. Sasa, S. Ishii, H. Kimura, H. Oshima, Y. Tajima, T. Takahashi, Y. Yamato,

M. Yamaguchi, T. Komatsubara, K. Shima and K. Furuno

[1] The 12UD Pelletron tandem accelerator

The total operating time and the experimental beam time were 2011.6 and 1662.8 hours, respectively. The operating time was about 90.5 % as compared with that in 2001. Fig.1 shows the distribution of operation hours every month. The beam time at various terminal voltages is shown in Fig.2. Fig.3 presents the summary of accelerated ions and fractions of their beam time for three ion sources. Fig.4 shows the percentage of experimental beam times for each research field. The voltage around 10 MV was used most frequently for experiments in comparison with other terminal voltages. In the year of 2002, the research fields of atomic and solid state physics, AMS and earth science increased the share of experimental beam time, while the research field of nuclear physics decreased it as compared with that in the last year.
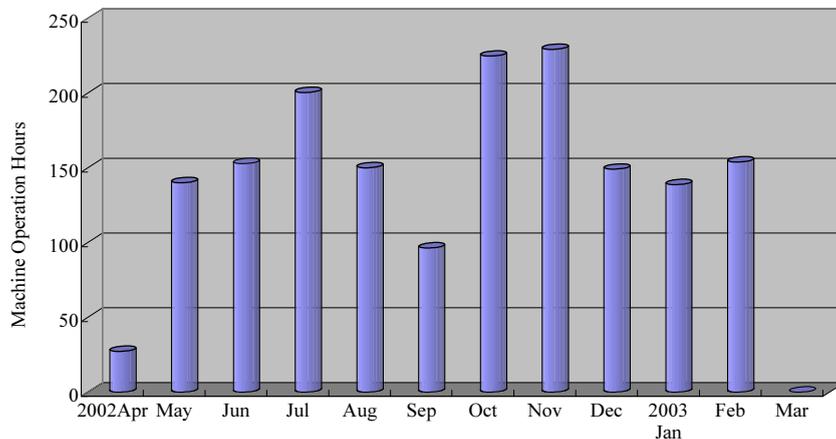
Fig.1. Accelerator operation hours per month from April in 2002 to March in 2003.
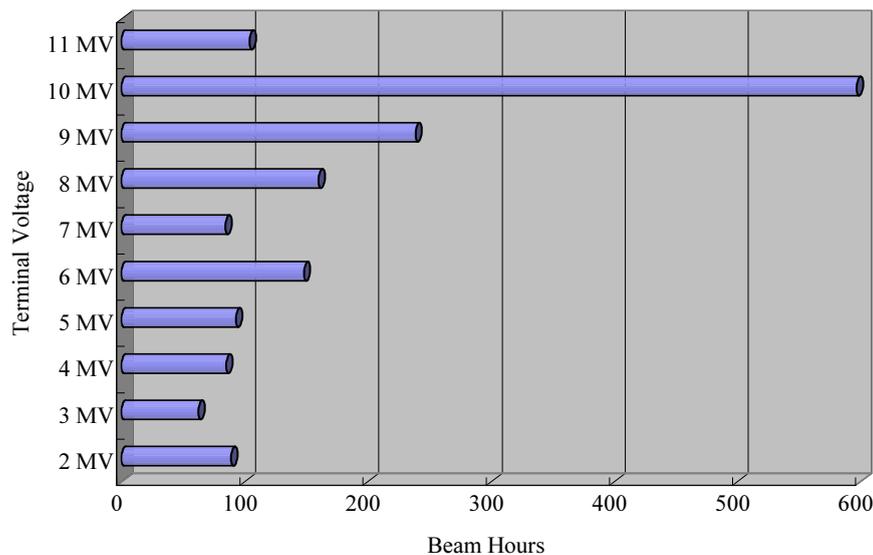
Fig.2. Beam time summed up every 1 MV of terminal voltages.
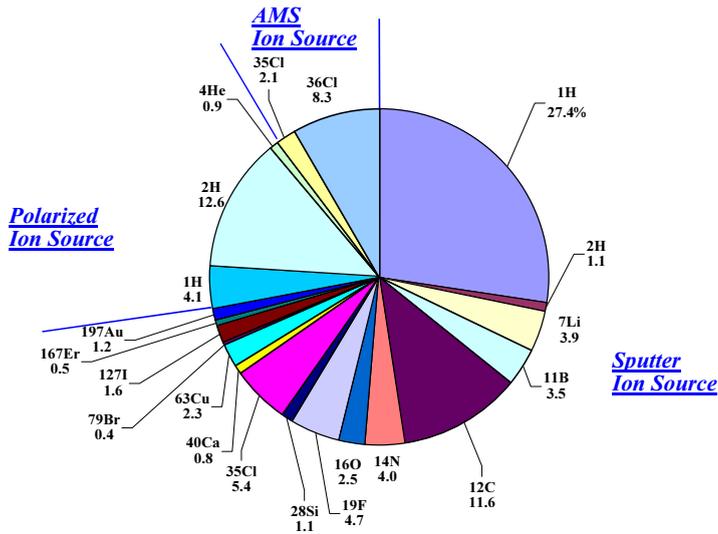
Fig.3. Accelerated ions and fractions of their beam time for three ion sources.
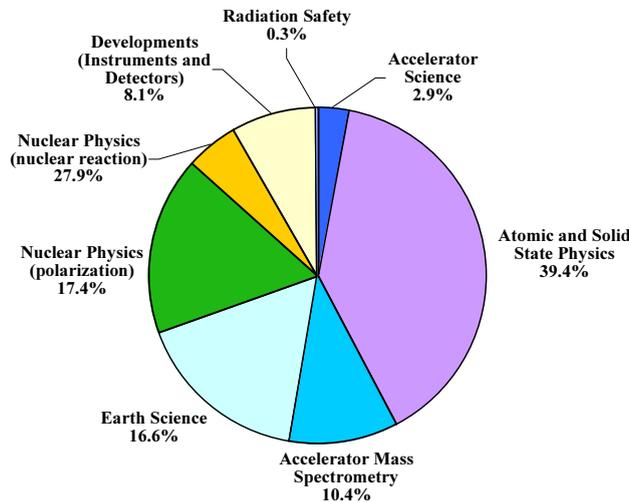
Fig.4. Percentage of experimental beam times for each research field.

The scheduled maintenance was finished on April 5 in 2002. After voltage conditioning, we provided beams for experiments from April 22. The operation of the 12UD Pelletron tandem accelerator was very stable for the period from April in 2002 to March in 2003. However, the driving mechanism of the foil unit-A broke down in December, and we could not change any foil in unit-A. A hanging stripper foil was burned out by the irradiation of heavy ion beam. After this trouble, only the foil unit-B was used in the operation of the 12UD Pelletron tandem accelerator.

The scheduled maintenance in the spring of 2003 was started from March 3 and finished on April 9. The major works of this maintenance were as follows. All corona points were replaced along the column and the accelerating tube. Stripper foils in the foil unit-A and B were also replaced by new foils. We repaired the oiling system, the shorting rod contacts and the insulating sheets of the chain pulley. We also repaired

the broken driving mechanism of the foil unit-A. We modified the structure of the terminal to make larger apertures. It was requested by AMS research group from a reason that somewhat wider acceptance of the tandem accelerator was needed in AMS experiments to obtain better reproduction of measurements and higher accuracy of the data. Fig.5 shows the old and new terminal stages.

In the year of 2002, we lost SF_6 gas by about 800 kg in the operation of the gas handling system. This is a serious problem for us. We are investigating the cause of this problem. We added 1000 kg SF_6 gas to the main accelerator tank during the scheduled maintenance

| Old terminal stage | New terminal stage (after April, 2003) |
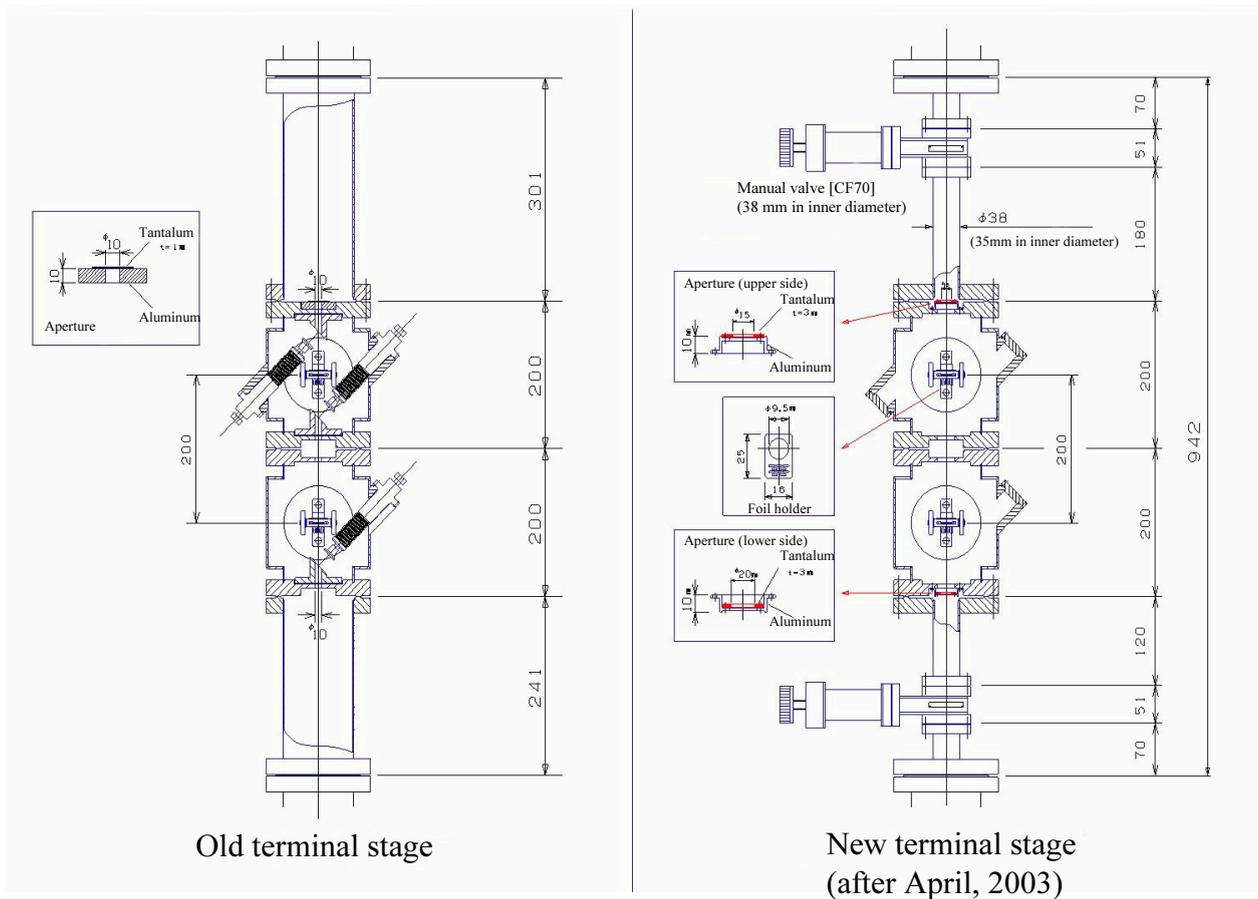
Fig.5. Old and new terminal stages.

[2] The 1MV Tandetron accelerator

The total operating time of the 1 MV Tandetron accelerator was 182 hours for the period of 2002. He ion beam is highly required for RBS analysis, but the duoplasmatron ion source for He[-] production does not supply sufficient intensity of beam currents for experiments at present. While the scheduled maintenance in the spring of 2003, we found that the accelerating tank tilted with respect to the beam line. We corrected the tilt by moving the accelerating tank. Fig.6 shows the transmission of proton beam as a function of the terminal voltage. The transmission is estimated by the ratio of the beam current from the sputter ion source to the accelerated beam current on the C (15°) beam course with a collimator of 3 mm in diameter. The transmission of proton beam was decreased sharply before the maintenance as compared with that in March of 1999. After the maintenance, the transmission was improved, but still much lower

than earlier transmission. Further works are necessary. Table 1 summarizes the typical beam transmissions for various ions at the terminal voltage of 500 kV, but these results were measured in March of 1999.
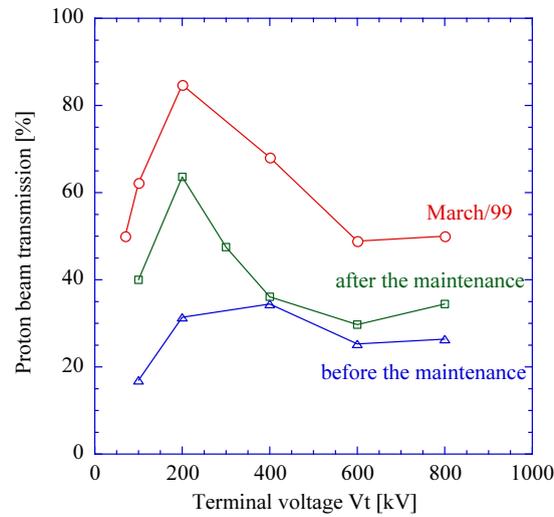
Fig.6. Transmission of proton beam as a function of the terminal voltage.

Table 1. Typical beam transmissions for various ions on the C (15°) beam course (Vt=500 kV).

	Beam current FC 2 [μA]	Beam current on target [μA]			Beam size on target	Transmission[%]
		+	++	+++		
^{1}H	4.0	2.4			~ ϕ 2.5 mm	60.0
^{12}C	4.3	1.1	2.0	0.43	~ ϕ 2.5 mm	52.2
^{35}Cl	13.6	3.6	5.3	3.0	~ ϕ 3 mm	53.3
^{79}Br	2.1 (^{79,81}Br)	0.36	0.3	0.09	~ ϕ 3 mm	25.7
^{107}Ag	0.27 ($^{107, 109}$Ag)	0.022	0.046	0.03	~ ϕ 3 mm	20.4

At the scheduled maintenance in the spring of 2003, we renewed beam courses [1] for the 1 MV Tandetron accelerator. The electron spectroscopy line was shut down, while the micro-beam line for PIXE experiment will be constructed at the A (30°) beam course. The B (11°) beam course is setting up towards a dedicated C_n cluster experiment.

We have started on a new project for the C_n cluster experiment by means of the 1 MV Tandetron accelerator. Preliminary experiments of accelerating C_n cluster ions were performed on the B (11°) and C (15°) beam courses. The C_n cluster ions are generated by a cesium sputtering negative ion source with a graphite cathode. The negative C_n cluster ions are extracted from the ion source by the energy of 20 keV and bent by a switching magnet to 30°. Fig. 7 shows the transmission of carbon beams (C_n: n=1) as a function of the terminal voltage on the C (15°) beam course with a collimator of 3 mm in diameter. These results were measured before and after the maintenance. Fig.8 (a) shows the typical mass spectrum of C_n cluster ions extracted from the ion source. Beam currents were measured by FC2 placed behind the switching magnet. The mass of C_{11} (132 amu) is closed to that of ^{133}Cs (133 amu), therefore the mass of CsC_n cluster ions is also closed to that of the C_{11+n} cluster ions [2]. It is difficult to separate C_{11+n} cluster

ions from CsC_n cluster ions. It is necessary to accelerate C_n cluster ions as the same energy ratio (keV/amu) for the interaction experiment between the cluster ions and the target. Fig. 8 (b) shows the beam currents of C_n cluster ions (n=1, 4, 8) accelerated as 20 keV/amu on the B (11°) beam course with a collimator of 1 mm in diameter. Table 2 summarizes the experimental conditions of C_n cluster ions accelerated for the B (11°) and C (15°) beam courses.
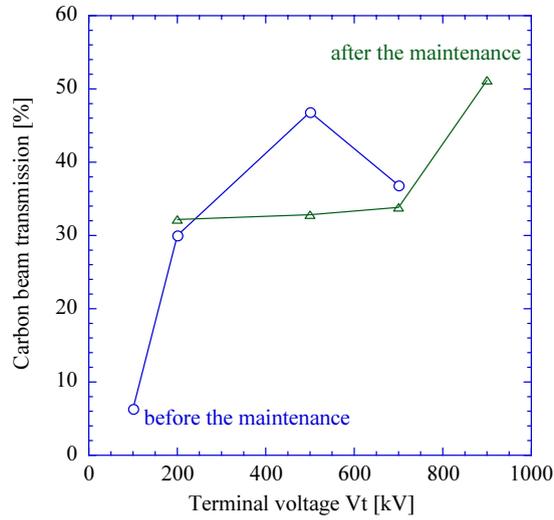
Fig.7. Transmission of carbon beams (C_n: n=1) as a function of the terminal voltage on the C (15°) beam course with a collimator of 3 mm in diameter.

	(a)			(b)
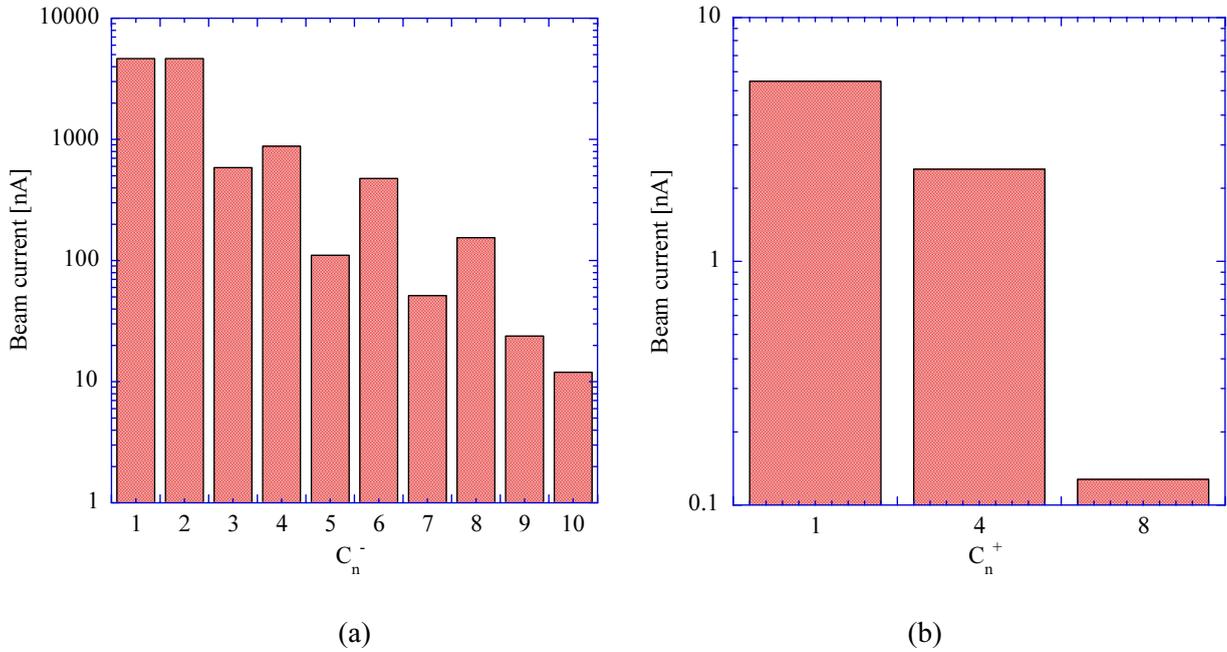
Fig.8. (a) Typical mass spectrum of C_n cluster ions extracted from the ion source. (b) Beam currents of C_n cluster ions (n=1, 4, 8) accelerated as 20 keV/amu on the B (11°) beam course with a collimator of 1 mm in diameter.

Table 2. Experimental conditions of C_n cluster ions for the B (11°) and C (15°) beam courses.

Beam course	Cluster size: C_n	E (keV/amu)	ρ [m]	ME/q^2
B (11°)	$1 \leq n \leq 8$	20	1.84	245
C (15°)	$1 \leq n \leq 6$	20 - 24	1.40	127

References

[1] K. Sasa et al., UTTAC68 (1999) 1.

[2] Y. Saitoh, K. Mizuhashi, S. Tajima, Nuclear Instruments and Methods in Physics Research A 452 (2000) 61-66.

1.2   Performance tests of the Tsukuba high-energy nuclear microprobe

K. Sasa, K. Furuno, Y. Yamato, H. Ohshima, S. Ishii, T. Komatsubara and M. Kurosawa

[1] Introduction

In earth science, hydrogen concentration in melt inclusions confined in quartz or diamond provides important information about the mechanism of formation and evolution of magma. Nowadays, nuclear technique is known to be one of better tools for the detection of hydrogen in various materials. Several authors reported measurements of hydrogen concentration in quartz or diamond with ERDA or NRA [1, 2]. These measurements, however, were performed for thin samples at low beam energies around a few MeV using small accelerators. Since the size of melt inclusions is in the range from 30 to 100 μm, samples including melt inclusions must be thicker than 100 μm not to destroy the inclusions during slicing and polishing samples. We need, therefore, a high-energy beam to measure the hydrogen in such a thick sample over the whole range of the inclusions.

We have developed a system for hydrogen analysis [3] using a 20 MeV proton beam and ^{19}F ions with energies up to 25 MeV. The system is designed and constructed as an apparatus dedicated to the hydrogen analysis of geophysical samples. Our goal is to achieve a beam spot less than 30 μm in diameter at a beam current more than 0.1 nA. It consists of a beam line for microbeam production, a vacuum chamber equipped with a 3-directional sample-driving mechanism, an optical microscope for observation of samples and a proton or a gamma-ray detector. This report mainly describes operational tests and results on the beam focusing of 20 MeV protons under several conditions for openings of the beam defining slits.

[2] Description of the apparatus

The beam defining and the first divergence slits are both modified from their original forms [4] of fixed apertures to a type being variable rectangular slit openings. The material of the beam defining slit is tungsten, while it is copper for the first divergence slit. To reduce slit-edge scattering, the edges of these variable slits were polished to mirror surfaces with roughness less than 2 μm. The displacement of these slits was read with dial gauges having a minimum indication of 1 μm. Another modification from the original design is the placement of the second divergence slit just in front of the Russian quadruplet. The slit is a fixed aperture of 9 mm in diameter and 2 mm thick stainless steel.

Sample positions can be moved in steps of 1 μm with the aid of precision ball screws and stepping motors. This step is determined with the 1 mm lead of the ball screw and the rotation angle of 0.36°/pulse in the stepping motor. The reproducibility of the position determination is measured with a calibrated scale to be ± 2 μm for a movement of 30 mm. The magnification of the optical microscope is variable between 55 and 690.
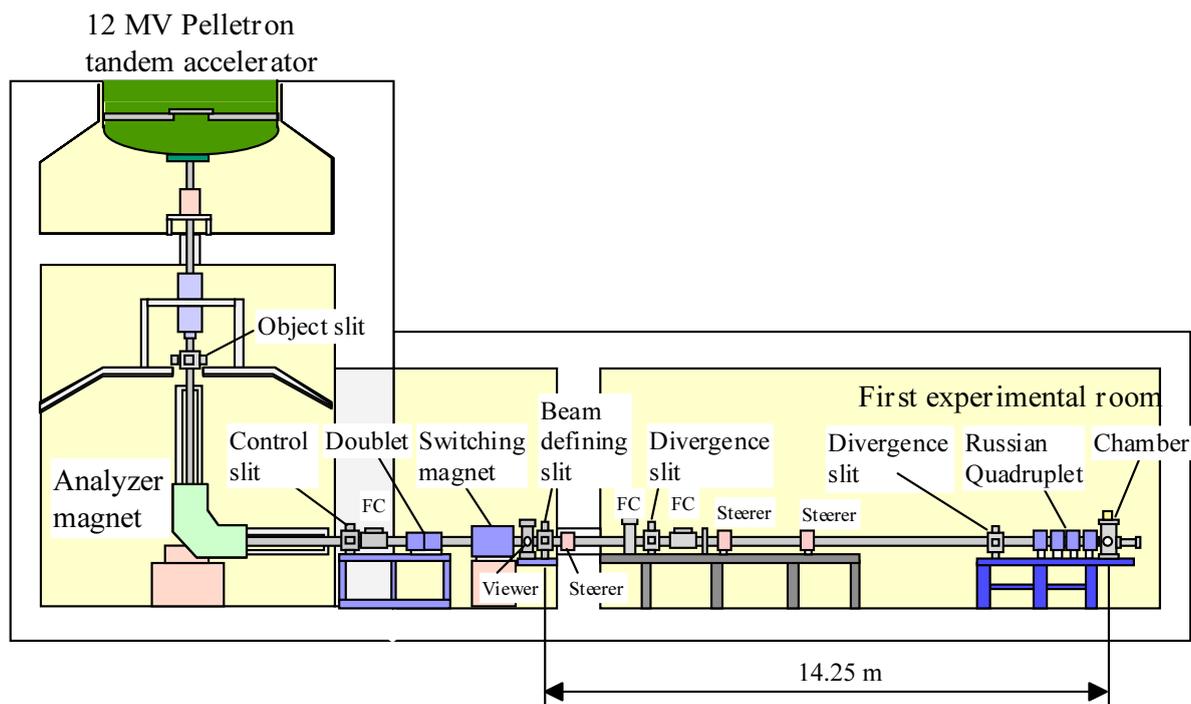
Fig.1. A schematic drawing of the beam line for microbeam production.

[3] Experimental results on the beam focusing and discussion

The size of a beam spot on samples is important for investigations of the hydrogen in melt inclusions. At first, we observed scintillation light emitted from a ZnS plate attached to the sample holder by bombarding the ZnS plate with a low intensity beam. The scintillation light was observed with the optical microscope mounted on the vacuum chamber. The angle of observation was 180° with respect to the incident beam using a 45° mirror with a beam through hole. We used a magnification of about 650 for the optical microscope. The scintillation light comprised of a very bright part and a large halo which was at least three times as large as the very bright part. We measured horizontal and vertical lengths of the very bright part by superposing its captured microscope image on the image of the calibrated scale on the sample holder. Just after the observation of this scintillation light, we moved the sample holder and bombarded a 25 μm thick tantalum wire to measure elastic scattering events with a SSD at an angle of 135°. Fig.2 displays typical scattering yields as a function of the displacement of the tantalum wire in horizontal and vertical directions. In this case, we operated two quadrupole magnets in the Russian quadruplet in the doublet mode. The openings of the beam defining slit were 120 μm in horizontal and 200 μm in vertical directions. The full width of this beam spot can be estimated to 25 μm ± 5 μm in the horizontal and 5 μm ± 3 μm in the vertical direction. This beam spot size is in reasonable agreement with that determined from the very bright part of the scintillation light. Additional confirmation was obtained by observing the fact that all the scintillation light as well as the large halo disappeared completely when the very bright part passed through a pinhole of 30 μm in diameter opened through the ZnS plate. In Table 1, experimental results on beam spot sizes and final beam currents obtained for 20 MeV protons are summarized. Beam spot sizes were estimated from the very bright part of scintillation light. The experimental uncertainty is ± 3 μm.
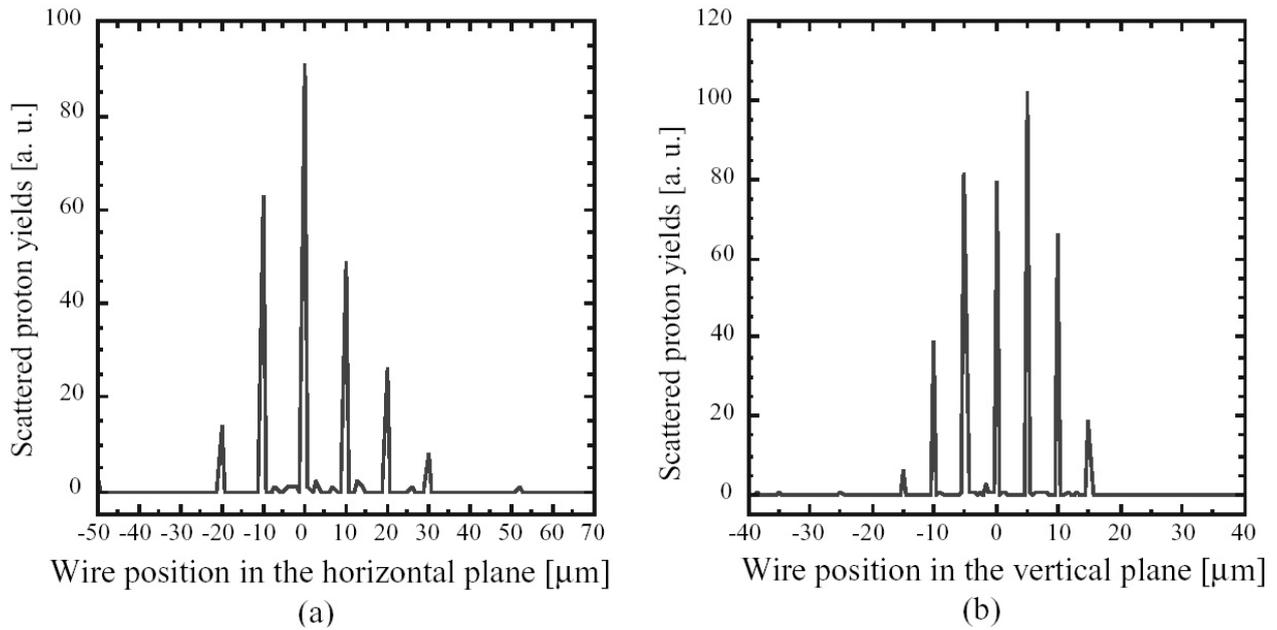
Fig.2. Yields of protons scattered on a 25 μm tantalum wire in the horizontal plane (a) in steps of 10 μm and the vertical plane (b) in steps of 5 μm.

The beam spot size can be calculated as the product of opening widths of the beam defining slits and the demagnification factors in both horizontal and vertical directions. The demagnification factors were calculated in terms of the computer program TRACE 3-D [5] with assumptions of 0.1 % beam energy resolution and uniform brightness. The openings of the beam defining slit and the beam divergence were assumed to be 200×200 μm^2 and 0.43 mrad, respectively. The calculated demagnification factors and corresponding beam spot sizes are listed in Table 1. Parasitic aberrations are not taken into account in these calculations.

Table 1 Calculated and experimental spot sizes obtained for a 20 MeV proton beam. The calculation is assumed to a beam current of 1.2 nA.

	Quadrupole Doublet			Russian Quadruplet
Calculated results				
Object slit [μm^2]	200×200			200×200
Expected beam spot size [μm^2] with no parasitic aberrations	27.7×4.8			14.9×14.9
Demagnification factor	$D_x=7.2, D_y= 41.7$			$D_x= D_y=13.4$
Maximum mass energy product ME/q^2 [MeV amu]	45			100
Experimental results				
Object slit [μm^2]	60×200	120×200	200×200	200×200
Spot size [μm^2]	14×6	22×8	30×10	25×20
Target current [nA]	≤0.15	≤0.5	≤2	≤2

Since the experimental beam spot size obtained with the Russian quadruplet is smaller than 30 μm in diameter, the design purpose of the present microprobe system is achieved. The experimental beam spot size, however, is clearly affected by aberrations. In fact we observed an appreciable rotation of the beam spot on the ZnS plate near an optimal focus. Qualitatively, this rotation could be ascribed to some rotational misalignments in each quadrupole singlet in the Russian quadruplet.

Melt inclusions in natural geophysical samples have various shapes. Therefore a rectangular beam spot would be preferable in some cases. From this point of view, we tested operation in the doublet mode using the last two quadrupole singlets in the Russian type configuration. The experimental results are listed in Table 1 together with calculated demagnification factors and beam spot sizes. The minimum spot size obtained in this doublet mode of operation was 14×6 μm^2 at a beam current of 0.1 nA. This beam current is still high enough for the hydrogen analysis by the proton-proton scattering. These data suggests that the present microprobe system has flexibility in a practical sense because we can easily prepare wide variety of beam spots depending on shapes of melt inclusions. The switching from the Russian quadruplet to the doublet mode can be made by only a few mouse clicking of the symbols relevant to the magnets on the display terminal at the control console.

[4] Summary

We have developed a microprobe system dedicated to the hydrogen analysis of geophysical samples. The smallest beam spot size obtained so far is 14×6 μm^2 for a 20 MeV proton beam. The performance of the present microprobe system is fully sufficient for such measurements of hydrogen in melt inclusions that are important in earth science. Somewhat smaller beam sizes could be obtained by increasing brightness of the beam with an improved operation of the ion source. However, the beam spot size is mainly limited by aberrations in the Russian quadruplet which was modified from old conventional quadrupole doublets for a beam transport line. To decrease the aberration in the present Russian quadruplet is rather difficult.

References

[1] S. H. Sie, G. F. Suter, A. Chekhmir, T. H. Green, Nucl. Instr. and Meth. B 104 (1995) 261.

[2] R.D.Verda, J. R. Tesmer, C. J. Maggiore, M. Nastasi, R. W. Bower, Nucl. Instr. and Meth. B 183 (2001) 391.

[3] K. Sasa, H. Ohshima, Y. Yamato, T. Komatsubara, T. katabuchi, K. Shima, K. Furuno, M. Kurosawa, N. Yanagisawa, Nucl. Instr. and Meth. B 190 (2002) 287.

[4] K. Sasa et al., Annual report 2001, UTTAC-70(2002) 10.

[5] K. R. Crandall, D. P. Rusthoi, TRACE 3-D Documentaion, third ed., Los Alamos National Laboratory Report, LA-UR-97-886, 1997.

1.3   Development of a laser ion source for metallic ions

K. Sasa

A laser ion source (LIS) is a versatile tool to produce high-flux multi-charged ions [1, 2]. One of the problems in LIS is that ions extracted from LIS have a broad energy distribution. The development of a new LIS has been started with the design concept that LIS couples with an electron-cyclotron-resonance (ECR) ion source. The efficient production of highly charged ions in the ECR ion source ensures elimination of molecular ions or micro-particles produced by laser ablation. It consists of LIS as a first stage, followed by the ECR ion source as a second stage which acts as a charge state multiplier and a stable beam extractor. A compact Nd:YAG pulsed laser with the pulse width of 8 ns and the maximum energy of 50 mJ at 1064 nm wavelength was employed to evaporate sample materials as a primary source for the ECR plasma. This report describes preliminary tests of LIS.

A laser beam was focused on a 3 mm thick copper target placed in a vacuum chamber. A pressure in the chamber was 6.7×10^{-4} Pa. A focusing lens was placed at 150 mm at a 45° with respect to the target surface. The laser spot was 0.5×10^{-2} cm^2 at the target position. The maximum power density on the target was achieved to 1.3×10^9 W/cm^2 for the laser energy of 50 mJ. Ions evaporated from the copper target by laser ablation were measured by a Faraday cup (FC) with a suppressor biased to -400V. The FC was located at 500 mm, and a collimator with 8 mm in diameter was placed at 420 mm from the target position. The accelerating voltage up to 5 kV could be applied to the target. Fig.1 shows an experimental set-up.
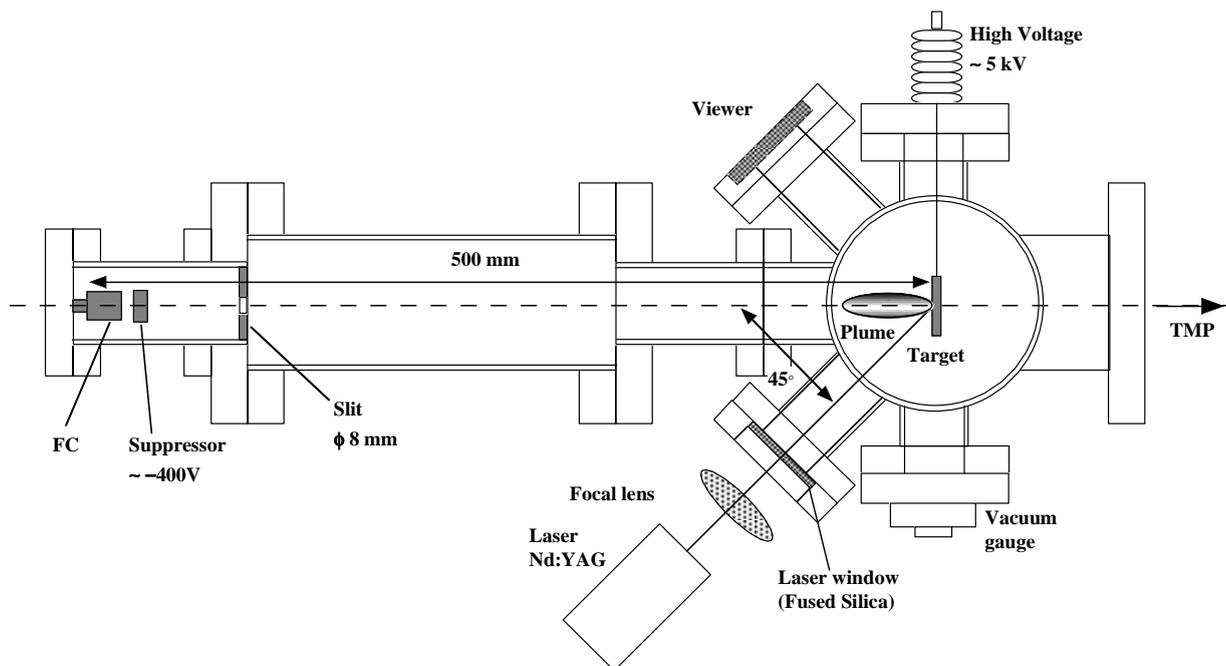
Fig.1.Experimental set-up.

Fig.2 (a) shows typical copper ion spectra obtained by laser energies of 40 mJ and 50 mJ. Each spectrum shows the ion intensity as a function of the flight time. The mean flight time $<t>$ was estimated from the time interval between the start signal and the centroid of the ion distribution. The mean ion velocity $<v>$ was approximately evaluated to be $<v>=d/<t>$. The mean flight times were about 14.8 μs and 13.0 μs for laser energies of 40 mJ and 50 mJ without the accelerating voltage. The experimental values of $<v>$ were calculated to be 3.4×10^4 m/s and 3.8×10^4 m/s, from which the corresponding mean kinetic energies were estimated to 376 eV and 470 eV, respectively. The maximum beam current was 0.13 mA at the laser energy of 50 mJ. No beam was observed when the laser power density was lower than 0.8×10^9 W/cm^2. Fig.2 (b) shows copper ion spectra obtained with the accelerating voltage ranging from 0 to 2 kV at the laser energy of 50 mJ. The maximum beam current increased to 0.51 mA when the accelerating voltage was 2 kV. These results demonstrate that high-flux metallic ions can be produced by the compact pulsed laser.

The relative amount of neutral particles and ions in the plume emission will be measured in the next step. The drift line connected to the ECR ion source is designed, at present.
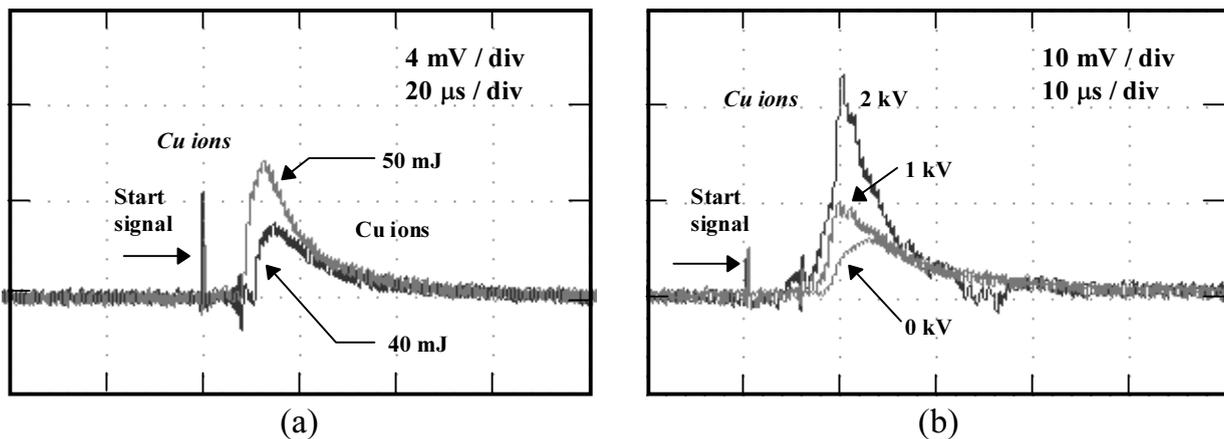
Fig.2. TOF spectra of copper ions produced by laser energies of 40 mJ and 50 mJ without accelerating voltage are shown in (a). TOF spectra observed with accelerating voltages of 0, 1 and 2 kV at the laser energy of 50 mJ are shown in (b).

References

[1] L. Torrisi, L. Ando, S. Gammino, J. Krasa, L. Laska,
Nuclear Instruments and Methods in Physics Research B 184 (2001) 327-336.

[2] V. Nassisi, A. Pedone, A. Raino,
Nuclear Instruments and Methods in Physics Research B 188 (2002) 267-271.

1.4   Development of the gated MSTPC

H. Ishiyama[1], T. Kawamura[2], T. Hashimoto[2,3], T. Ishikawa[2], T. Furukawa[4], M. H. Tanaka[1], N. Yoshikawa[1], H. Miyatake[1], S. C. Jeong[1], T. Nomura[1], T. Komatsubara and Y. Tagishi

A project to acquire directly nuclear cross sections of (α, n) and (p, n) reactions using low energy light neutron-rich radioactive nuclear beams (RNBs) is in progress for nuclear astrophysical interests [1]. Measurements of ^{8}Li(α, n)^{11}B, ^{16}N(α, n)^{20}F [2], ^{16}N(p, n)^{16}O reaction cross sections have been already performed successfully.

For their measurements a detector system consists of a " Multi-Sampling and Tracking Proportional Chamber" (MSTPC) [3] and a neutron detector array. The MSTPC can measure a three-dimensional track of a charged particle and the energy loss along its trajectory. A RNB is injected into the MSTPC directly, which is filled with He + CO_2 (10%) or CH_4 gas. This filling gas also plays a role of a gas target.

The large pulse height defect (about 15%) of energy loss signals from the MSTPC was observed under high injection rate ($>10^3$ pps) of low energy heavy ions. It is supposed to come from the space charge gain limitation at its anode wires due to numerous ions generated by the proportional multiplication process. As a solution, a gating grid [4] was installed between an electron drift region and a proportional region inside the MSTPC. It can control the transparency to drift electrons by changing the electric potentials for every other gating gird wire. As the result of using the gating grid, the gas multiplication process at an anode wire is less induced than 20 events/s and the pulse height defect is suppressed successfully within 2% up to the 5.6 kpps injection rates of ^{14}N (E = 35 MeV) particles. But the expected RNB intensity will become 10^4 pps – 10^6 pps at KEK-JAERI joint RNB facility [5], which is under construction. So it is desirable that the MSTPC can work under higher injection rate (10^4 – 10^5 pps) of low energy heavy ions. A performance test of the MSTPC under such condition has been done at UTTAC.
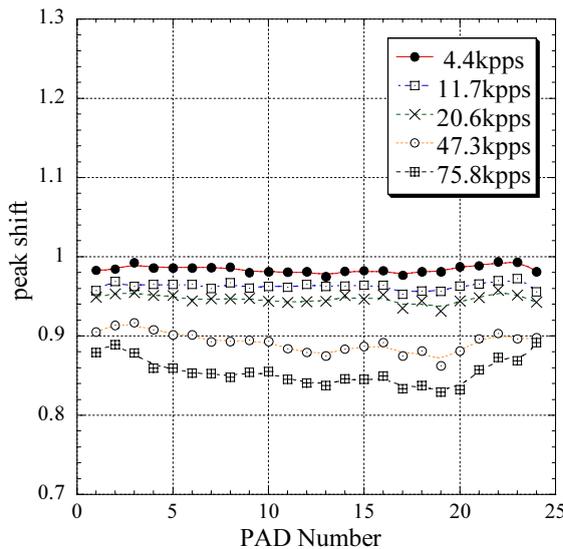
Fig. 1.Peak shifts using the gating grid under the ^{14}N-beam injection. The electric potential differences for each gating gird wires is –40V.

[1] High Energy Accelerator Research Organization, Oho1-1, Tsukuba-shi, 305-0801 Japan.
[2] Tokyo University of Science, Yamazaki 2641, Noda-shi, Chiba-ken, 278-8510 Japan.
[3] Research Fellow of the Japan Society for the Promotion of Science.
[4] Osaka University, 1-1 Machikaneyama, Toyonaka-city, Osaka, 560-0043, Japan.

The ^{14}N-beam (E = 35 MeV) was provided by Pelletron 12UD. The ^{14}N particles elastically scattered from a thin Au-target were transported to the MSTPC with a QDQ spectrometer. The gating grid was triggered by the reduced signals of a SSD in end of the MSTPC. The trigger rate was reduced by a down scalar.

Fig.1 shows peak shifts of the output signals versus counting rates using the gating grid. The vertical axis shows the pulse height normalized to that when the injection rate is a few pps. The horizontal axis shows the cathode pad number, which corresponds to the distance (the one pad length is 11mm) from the beam injection point inside the MSTPC . When the injection rate is 47.3 kpps, the pulse height defect becomes about 10%. As the result of a off-line analysis and a bench test, it is supposed to come from a few % leak of drift electrons to a proportional region even under the closed gate condition. This leak can be suppressed by increasing electric potential differences for every other gating grid wire. In order to check it, an experiment was performed using ^{7}Li-beam (E = 14 MeV) at JAERI tandem facility.
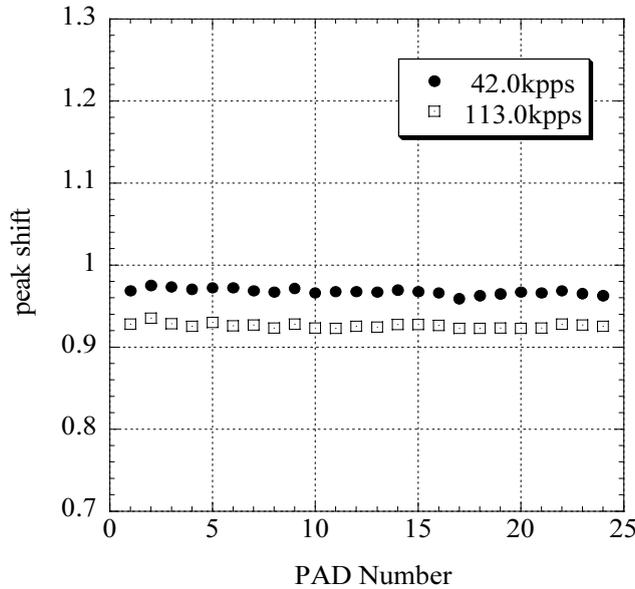
Fig. 2. Peak shifts using the gating grid under the ^{7}Li-beam injection. The electric potential differences for each gating gird wires is –68V.

Fig.2 shows the results. When the injection rate is 42 kpps, the pulse height defect is suppressed within 2% successfully. But when the injection rate is 113 kpps, the pulse height defect becomes about 7%. A further investigation and an improvement are therefore required.

References

[1] H. Ishiyama, et. al., Nucl. Phys. A718c (2003)481.
[2] T. Ishikawa, et. al., Nucl. Phys. A718c(2003)483.
[3] Y. Mizoi, et. al., Nucl. Instrum. Meth. Phys. Res. A 431(1999)112.
[4] P. Nemethy, et. al., Nucl. Instrum. Meth. A 212(1983)73.
[5] H. Miyatake, et. al., Nucl. Instrum. Meth. in press.

2.1 Analyzing powers for the $^6\text{Li}(\vec{d}, p)\,^7\text{Li}$ reaction at an incident energy of 90keV

N.Yoshimaru, M.Yamaguchi and Y.Tagishi

In order to obtain the information of the reaction mechanism of $^6\text{Li(d,p)}^7\text{Li}$ reaction at low energy region, we measured all four analyzing powers at incident deuteron energy of 90 keV. The preliminary results were reported in the previous annual report at UTTAC. All four analyzing powers, iT_{11}, T_{20}, T_{21} and T_{22}, were measured for laboratory angles from 0- to 165-degree with 15-degree step. The target ^6Li was prepared by vacuum evaporation of $^6\text{Li}_2\text{CO}_3$ onto a 15-μm-thick aluminum foil with thickness about $10\mu\text{g/cm}^2$. The emitted particles were detected by four silicon photodiodes (HAMAMATSU S3204).

We compared these data with calculations using resonance model in the reference [1]. In the present calculations, we assumed this reaction proceeds via the single resonance state of 2^+ of the compound nucleus of ^8Be. Results of calculations are shown in Fig. 1 as solid lines with data. The tensor analyzing powers are fairly well reproduced by such calculations. The vector analyzing powers are predicted zero values in this mode, in case of the reaction proceed via a single resonance state. However the measured vector analyzing powers gave negative values of around –0.1, so we cannot suggest that this reaction might proceed via a single resonance state of 2^+ of ^8Be. A further analysis is now in progress.

Reference

[1] F. Seiler, Nucl. Phys. A286, 1 (1977)
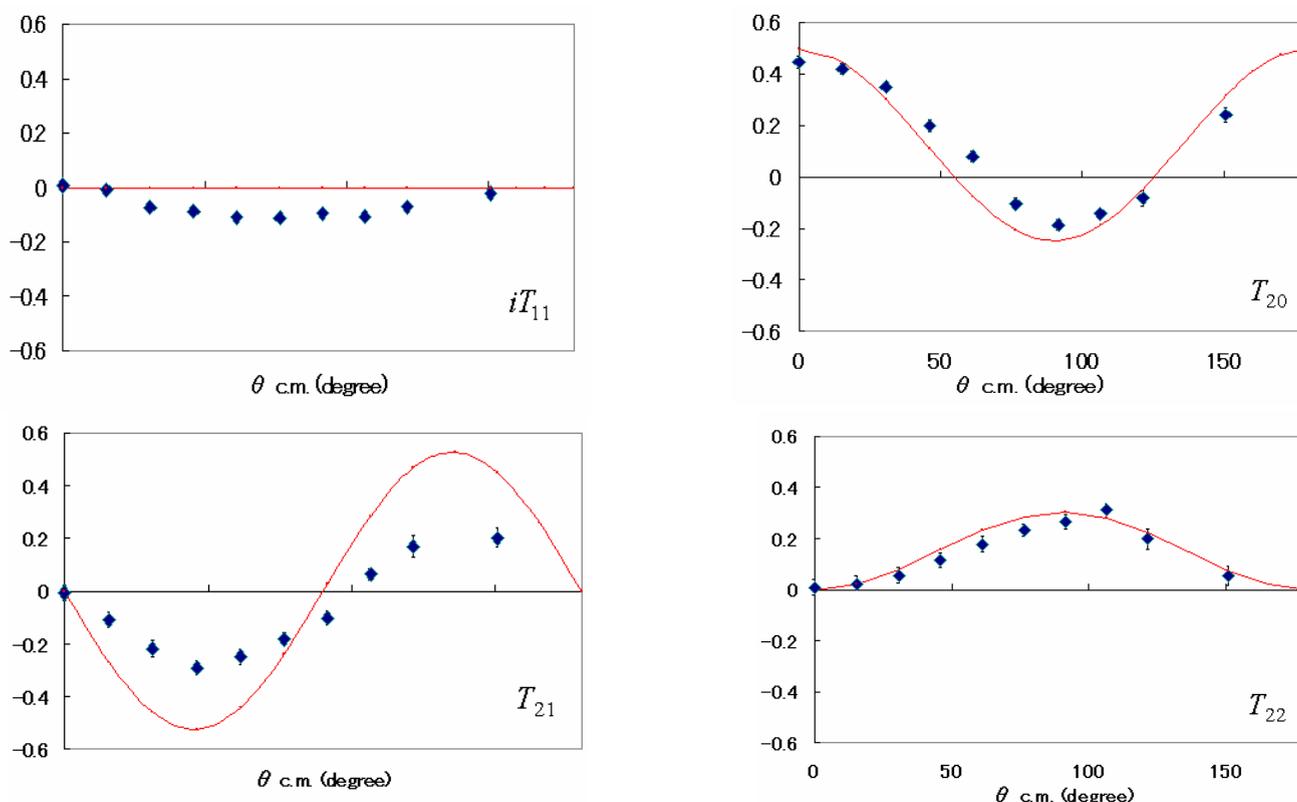
Fig.1　Analyzing powers iT_{11}, T_{20}, T_{21} and T_{22}. Dots are experimental data, and the solid curves are result of the resonance model.

2.2 Measurement of proton polarization in ^{208}Pb(d,p)^{209}Pb reaction at incident energy of 20 MeV

M.Yamaguchi, N.Kawachi, N.Yoshimaru, Y.Aoki, and Y.Tagishi

In the previous annual report [1], we presented data of the polarization of emitted protons from the ^{208}Pb(d,p)^{209}Pb reaction to the $\frac{9}{2}^{+}$ ground-state at an incident energy of 20 MeV. In the present work, complementary data were taken at six angles from 60 to 105°.

Emitted protons from ^{208}Pb(d.p) reactions were momentum-analyzed by QDQ magnetic analyzer system [2]. A high efficiency polarimeter [3] was used to measure the polarization of the protons.

Measured polarization data are shown in Fig. 1 together with the vector analyzing powers for the same reaction [4]. These data were compared with a finite-range DWBA and continuum discretized coupled channel (CDCC(d,p)) calculations. As shown in Fig.1, the vector analyzing powers are reproduced well by these calculations. However, the polarization data are not reproduced.

By a simple consideration, it can be explained that the angular distribution of iT_{11} should be similar to that of polarization if spin-flip probability were neglected. The difference between the vector analysing power and the polarization suggests that the spin dependent interaction to bring about spin flip should be take into account in the present (d,p) reaction.
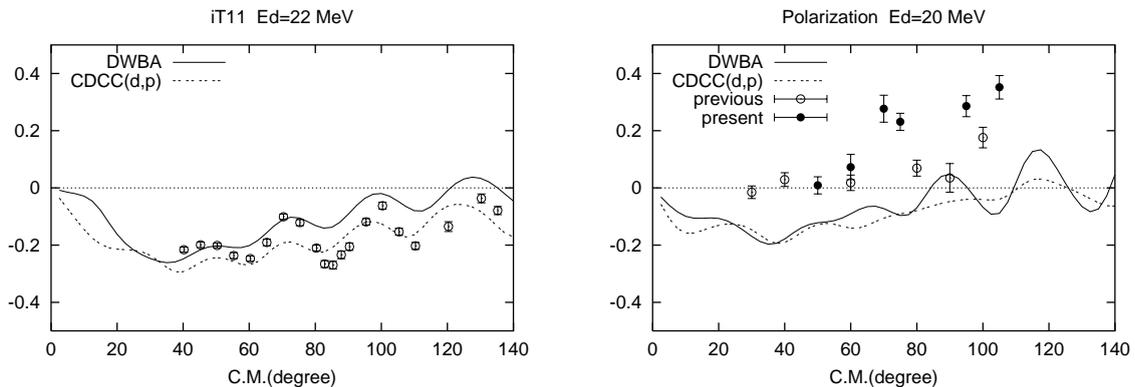
Fig. 1. The measured iT_{11} and polarization for the ^{208}Pb(d,p) reaction is shown. The present polarization data are shown by solid circles. The dashed lines are calculations in terms of CDCC(d,p) and the solid lines are calculations in terms of finite-range DWBA .

References

[1] M.Yamaguchi et al., UTTAC Annual Report 70, 31(2002)

[2] Y. Aoki, S. Hiroki, M. Tomizawa, Y. Tagishi and K. Yagi, UTTAC Annual Report 52, 5(1987)

[3] M. Yamaguchi, K.Sawada, T.Katabuchi, N.Kawachi, N.Yoshimaru, K.Shiga and Y.Tagishi, Nucl. Instr. and Meth., to be published

[4] K.Hirota, Y.Aoki, N.Okumura, Y.Tagishi, Nucl.Phys. A628, 547(1998)

2.3 Spin correlation measurement for ^{2}H(d,p)^{3}H reaction at incident energy of 20 MeV

M.Yamaguchi, N.Okumura, N.Yoshimaru, S.Ishii, Y.Tajima, Y.Tagishi, I.Daito[1], T.Inagaki[1], T.Kobayashi[1], N.Horikawa[1], M.Iio[2], N.Kuwazu[2] and N.Kawachi[3]

The spin correlation measurements are of interest for the nuclear physics of a few nucleon systems and also fusion energy applications. At low energy region, in particular it is suggested that the d-d fusion reaction should be suppressed for deuterons with parallel spins[1].

We arranged to make experiment for spin-correlation measurements in the ^{2}H(d,p)^{3}H reaction in collaboration with Nagoya University, where a polarized-deuteron target had been developed. The polarized-deuteron target system[2][3] was carried into UTTAC from Nagoya Univ. on April, 2002.

We designed a scattering chamber and detection system, which was shown in Fig. 1. A target made of deuterized polyethylene $((CD_2)_n)$ was placed at the center of the chamber. The target has a diameter of 4 mm and the thickness of about 20 μm. Emitted charged particles were detected with two counter-telescopes consisting of silicon solid-state detectors. Each telescope was comprised of a transmission type detector with thickness of 400 μm and thick detector with thickness of 3000 μm. Deuteron beam was produced by a Lamb-shift type polarized ion source at UTTAC[4] and accelerated up to 20 MeV. Double collimaters having 2 mm and 3 mm diameters were placed at 40 cm and 156 cm upstream from the target. A typical beam current was about 20 nA on the Faraday cup in the scattering chamber.

The target was placed at the center of magnetic field at 2.5 T generated by Helmholtz coils in order to polarize deuterons in the target. The directions of incident deuterons and ejected charged particles were deflected in this magnetic field. The left graph in Fig. 2 shows the strength of the magnetic field in the reaction plane. Ray-trace simulation was performed for incident deuterons and ejected protons and deuterons. According to the simulation, the total deflection of the deuteron beam during the travel through the magnetic field was about 7°. The right graph in Fig. 2 shows the ray-trace of the deuteron beam in the magnetic field. The ejected charged particles were also deflected from original emitted angles. The predicted energies of the emitted deuterons and protons observed with detectors placed outside of the magnetic field at each laboratory angle are shown in Fig. 3. The measured energy spectra are also shown in Fig. 3 with red lines. The peak positions of these red lines were well reproduced by the present simulation. The thicknesses of the target and refrigerant (liquid helium having the thickness of about 1 mm) caused the energy spreads of the peaks in these spectra. It was found that protons from the ^{2}H(d,p)^{3}H reaction were well separated from those of other reactions in emission-angle regions from 32 to 38° and from 49 to 63°.

References

[1] R .M. Kulsrud et al. Phys. Rev. Lett. 49(1982)1248

---

[1]Nagoya Univ.
[2]Miyazaki Univ.
[3]Natioanl Cardiovascular Center

[2] I.Daito, "Polarized deuteron target system for low energy D(d,p)T measurement", POLU-SION99,(1999).

[3] I.Daito, H.Doushita, S.Hasegawa, N.Horikawa, S.Horikawa, T.Iwata, K.Kondo, Y.Miyachi, K.Mori, N.Takabayashi, T.Tojyo, A.Wakai, "SPIN2000, 14th. International Spin Physics Symposium", AIP Conference Proceedings, **570**, 896(2001)

[4] Y.Tagishi and J.Sawada, Nucl. Instr. and Meth., **164**,411(1979).
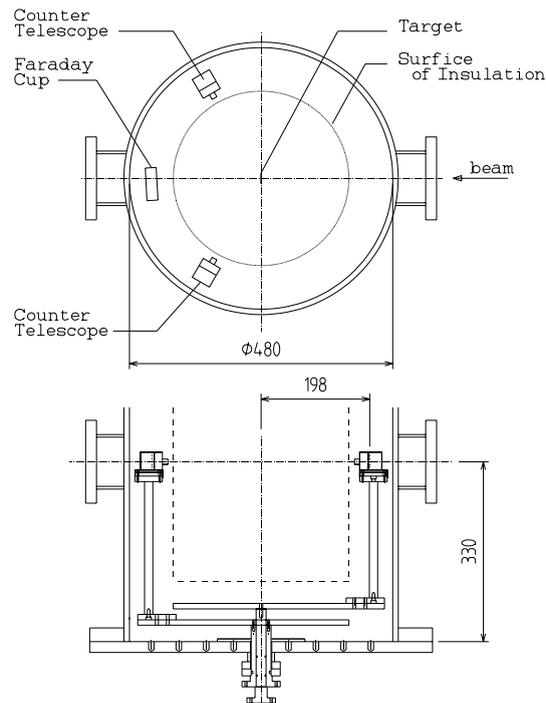
Fig. 1. Scattering chamber and the layout of the detectors. Dimension are given in units of mm.
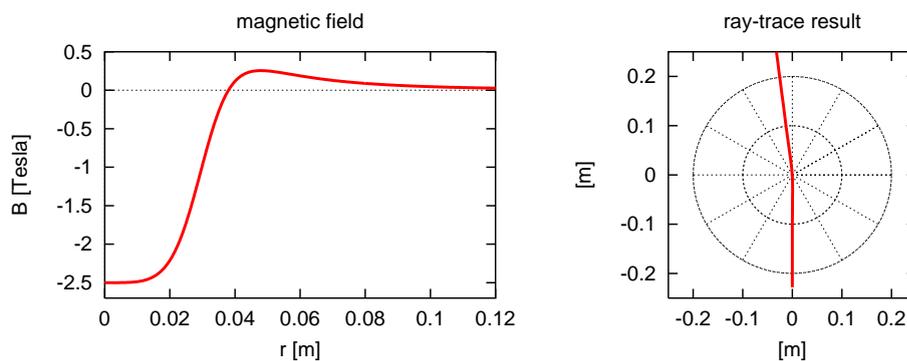
Fig. 2. The strength of the magnetic field at the horizontal scattering plane is shown in left side, which calculated from dimensions of the Helmholtz coil. The amplitude is normalized to -2.5 Tesla at the origin. The right side shows the result of the ray-trace calculation of the incident deuteron-beam at the horizontal scattering plane at 20 MeV.
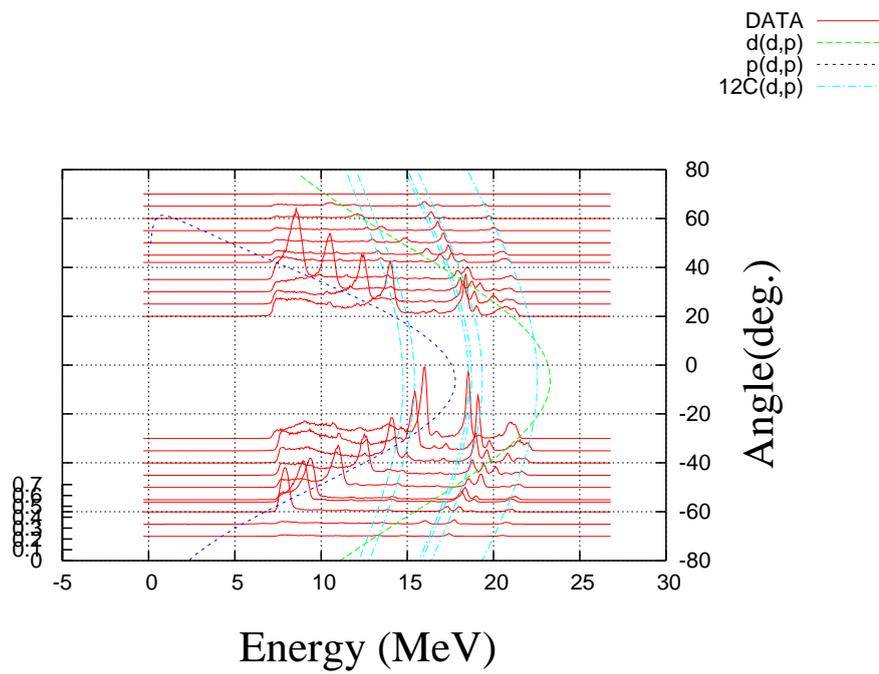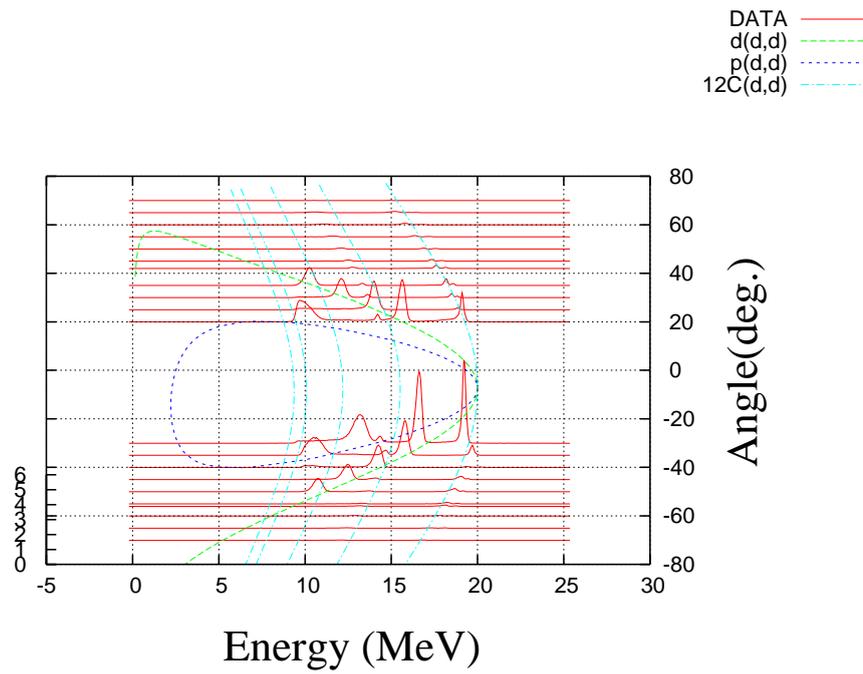
Fig. 3. The top figure shows the scattered deuteron energies detected outside of the magnetic field at each laboratory angle. The bottom one shows those of the emitted protons. The red curves show the measured energy spectra.

2.4 Energy dependence of proton elastic scattering from ^{28}Si around ^{28}Si(p, n) reaction threshold energy

N.Okumura and Y.Aoki

Proton total reaction cross sections have a resonance like behavior around ^{28}Si(p, n)^{28}P threshold energy [1]. This threshold effect should be observed in elastic scattering, so that the energy dependence of cross sections was studied. The incident energy range was from E_p^{CM} = 14.553 to 16.099 MeV and the energy loss in the target was 36 keV for 15.2 MeV proton. Fig. 1 shows the ratio of elastic scattering
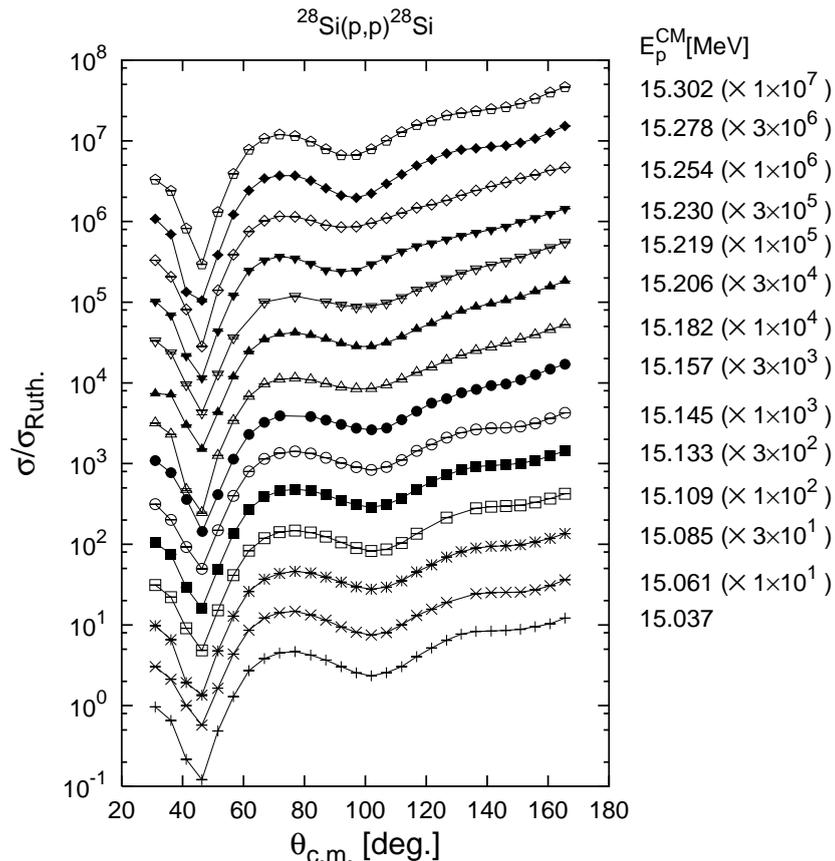
Fig. 1. Proton elastic scattering cross sections. The each line is shown for guide your eyes.

cross section to Rutherford cross section. From 15.157 to 15.254 MeV, angular distribution of the ratio becomes flat in the backward angles.

We searched the optical potential parameters that reproduced these cross sections and calculated phase shifts $\delta_{\ell j}$ for each energy. Energy derivative of the phase shift,

$$\tau_{\ell j} \equiv 2\hbar \frac{\partial \delta_{\ell j}}{\partial E},\tag{1}$$

is the time delay for each (ℓ, j) partial wave (partial wave reaction time).

A few examples of the phase shift are shown in Fig. 2. We smoothed the phase shift and evaluated the partial wave reaction times (Table 1).
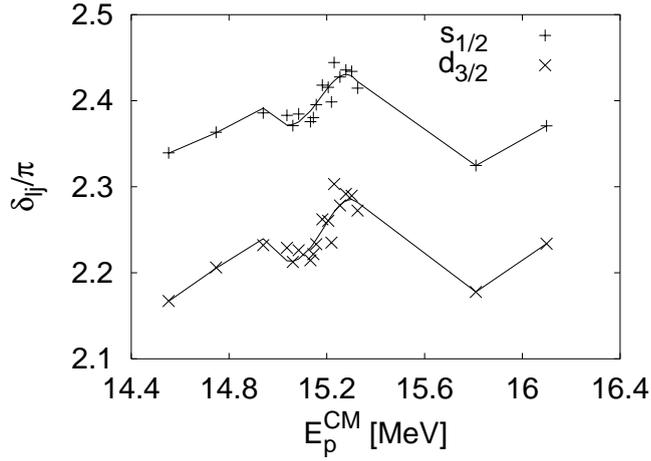
Fig. 2. Partial wave phase shift $\delta_{\ell j}$.

Table 1. Partial wave reaction time

| ℓ | $\tau_{\ell j}(\times 10^{-21} s)$ | |
	$j = \ell - \frac{1}{2}$	$j = \ell + \frac{1}{2}$
0	–	1.5
1	2.1	1.9
2	1.3	1.4
3	3.2	1.1
4	0.3	0.5
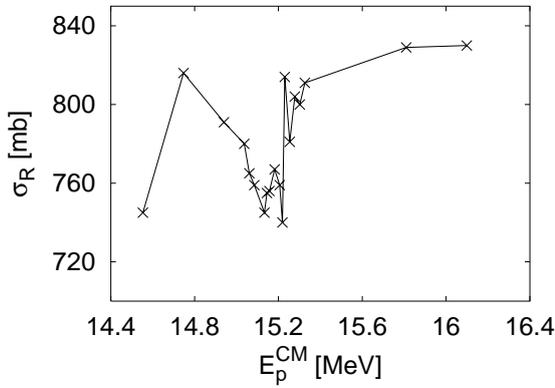
(a) Calculated σ_R
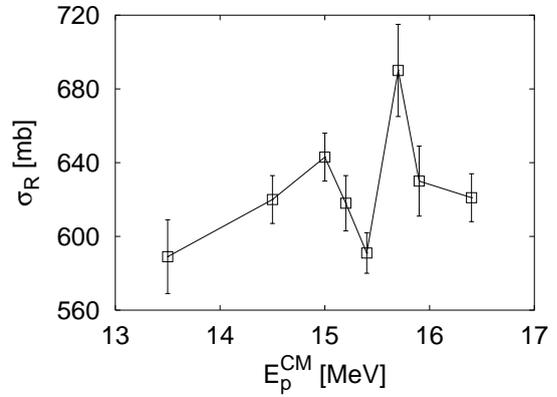
(b) Experimental σ_R

Fig. 3. the comparison of calculated and experimental total reaction cross sections

Total reaction cross sections calculated by the searched optical potentials are plotted in Fig. 3. Like our experimental total reaction cross sections [1], there is a dip in this calculation at the threshold energy.

References

[1] N. Okumura, Y. Aoki, T. Joh, Y. Honkyu, K. Hirota and K. S. Itoh, *Nucl. Inst. Meth.* A487(2002)565.

2.5 Energy dependence of deuteron total reaction cross sections below Coulomb barrier

Y. Aoki, N. Okumura, H.Ishiguro

Lawrence and coworkers [1] reported that the energy dependence of sub-Coulomb (d,p) reaction cross section is not so dramatic as is expected from the Gamow theory. Oppenheimer and Phillips [2] explained this energy dependence by assuming the Coulomb break-up followed by a neutron transfer reaction. A brief history and discussion against this Oppenheimer-Phillips effect is given by Bencze and Chandler [3].

By solving CDCC [4] equation, we evaluated the energy dependence of total reaction cross, σ_R, for several target nuclei, ^{12}C, ^{27}Al, ^{40}Ca, ^{90}Zr, ^{118}Sn, ^{142}Nd and ^{208}Pb. In one type of calculations Coulomb interaction is assumed to work between the center of gravity of the colliding pair. In other set of calculations, the proton in the incident deuteron interact with the uniformly charged sphere, the target nucleus.

CH89 [5] set of nucleon optical potential is assumed, irrespective of the incident energy and target atomic number.

Spin triplet states in p-n pair taken into account are $^3S_1 - {}^3D_1$, $^3D_{2,3}$, $^3P_{0,1}$ and $^3P_2 - {}^3F_2$ states. Wave functions of these states are calculated by using Reid soft core potential parameters [6]. Only energetically open channels are explicitly considered.

Figure 1 shows the energy dependence of the ratio of the total reaction cross sections with and without Coulomb breakup contributions, $\sigma_R(withCBU)/\sigma_R(withoutCBU)$.
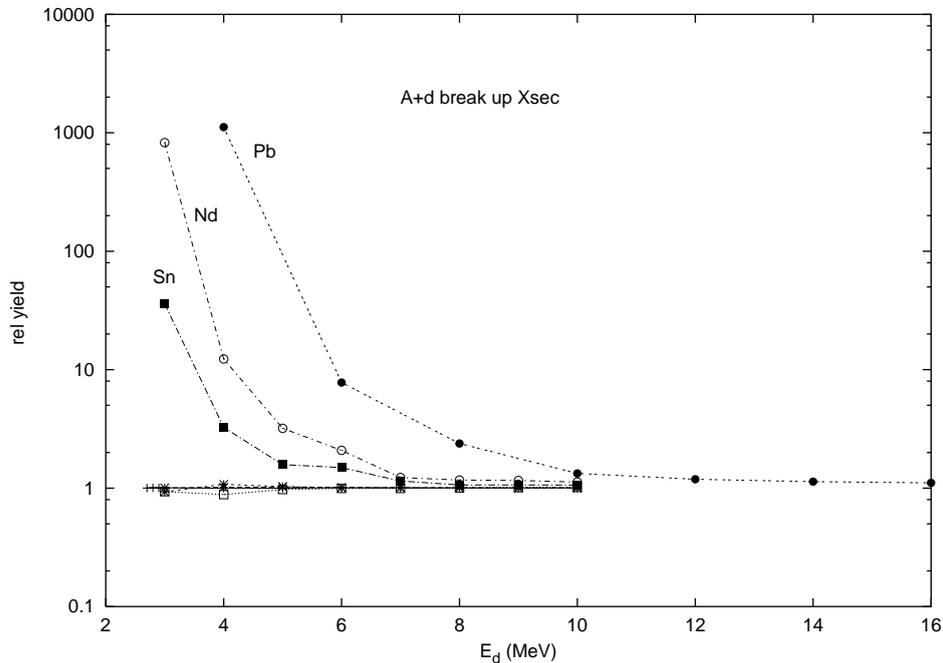
Remarkable enhancement can be seen for the target of large atomic number ($Z > 40$). The ratio is almost 1 for lower Z targets and well above 1 for heavier targets. It is estimated that the curves depart from 1 for $E_d < (Coulomb\ barrier\ height)/2$. From these calculations, Oppenheimer-Phillips effect via open channels seems to be unimportant for light nuclei.

References

1 O.E. Lawrence, E.McMillan and R.L. Thornton, Phys. Rev. **48**, 493(1935)

2 J.R. Oppenheimer and M. Phillips, Phys. Rev. **48**,500(1935)

3 Gy. Bencze and Colston Chandler, Phys. Rev. **C53**,880(1996)

4 M. Kamimura, M. Yahiro, Y. Iseri,Y. Sakuragi, H. Kameyama and M. Kawai, Prog. Theor. Phys. Jpn. Supp.,**89**(1986).

5 R.L. Varner, W.J. Thompson, T.L. McAbee, E.J. Ludwig and T.B. Clegg, Phys. Rep.**201**(1991) 59.

6 R.V. Reid, Jr., Ann. Phys. **50** 411(1968).

2.6 CDCC analysis of triple differential cross section of ^{208}Pb(d,pn) reaction at E$_d$=56 MeV

Y. Aoki, N. Okumura, T. Jho and Y. Iseri[a]

As an extension of an CDCC analysis, triple differential cross sections of deuteron elastic break up process is studied.

The concept of Continuum Discretized Coupled Channels (CDCC) approach of deuteron elastic scattering and breakup process is spelled out by Kawai and co-workers in ref. [1]. A brief description is given here just to remind the concepts of the ingredients. The CDCC Hamiltonian may be written as follows,

$$H = T_p + V_p + T_n + V_n + V_{pn},$$

where T_p and T_n are kinetic energy operator of a proton and a neutron, which are bound to form a deuteron in the incident channel. They interact with each other by the potential V_{p-n}. Continuum states are discretized by wave number binning. We assumed that the spin flip process may be negligible and the spin singlet states are neglected. Scattering states really taken into the analyses are, $^3S_1 - {}^3D_1$, $^3D_{2,3}$, $^3P_{0,1}$ and $^3P_2 - {}^3F_2$ states. Wave number k_{p-n} of the relative p-n motion are binned by 10 bins of $k_{p-n} = 0 - 0.1$, $\cdots$ $0.9 - 1.0 fm^{-1}$. Reid soft core potential [2] is assumed whenever it is available. Gaussian potential, which reproduce the phase shift, is assumed for the $^3D_3$ states.

Proton and a neutron interaction with a target nucleus are given by potentials of V_p and V_n. No explicit excitation of target nucleus and rearrangement reactions are taken into account. Nucleon optical potential, CH89 [3], of half the deuteron kinetic energy $E_p = E_n = E_d/2$ are assumed in the present analyses. Proton in the deuteron interact with the target nucleus via Coulomb potential, which are assumed to be due to uniformly charged sphere. Because deuteron is a bound state of proton and a neutron, antisymmetrization correction is necessary even if we assume that the phenomenological optical potential takes care of the exchange effect of incident nucleon and nucleons in the target. This antisymmetrizaton correction is phenomenologically taken into account by reducing(increasing) the real(imaginary) central part of the optical potential.

Proton and neutron coordinates $\mathbf{r}_p$, $\mathbf{r}_n$ are expressed by the center of mass and relative coordinates by the following relation,

$$\mathbf{R} = (\mathbf{r}_n + \mathbf{r}_p)/2, \quad \mathbf{r} = (\mathbf{r}_n - \mathbf{r}_p)$$

Coupled channels equation for the R coordinates are written by partial wave expansion, solved numerically and S-matrices are obtained. In handling the nucleon spin-orbit potential, terms with $(\mathbf{s}_p - \mathbf{s}_n)$ are neglected.

A detailed data of elastic scattering by Matsuoka [4] and triple differential cross sections by Okamura [5] are taken into account and the case of 56 MeV deuteron + ^{208}Pb are considered.

Elastic differential cross section and other polarization observables are calculated from the elastic S-matrices. Differential cross section of experimental data and the present analysis are compared in fig. 1.

^{208}Pb(d,d) E_d= 56 MeV
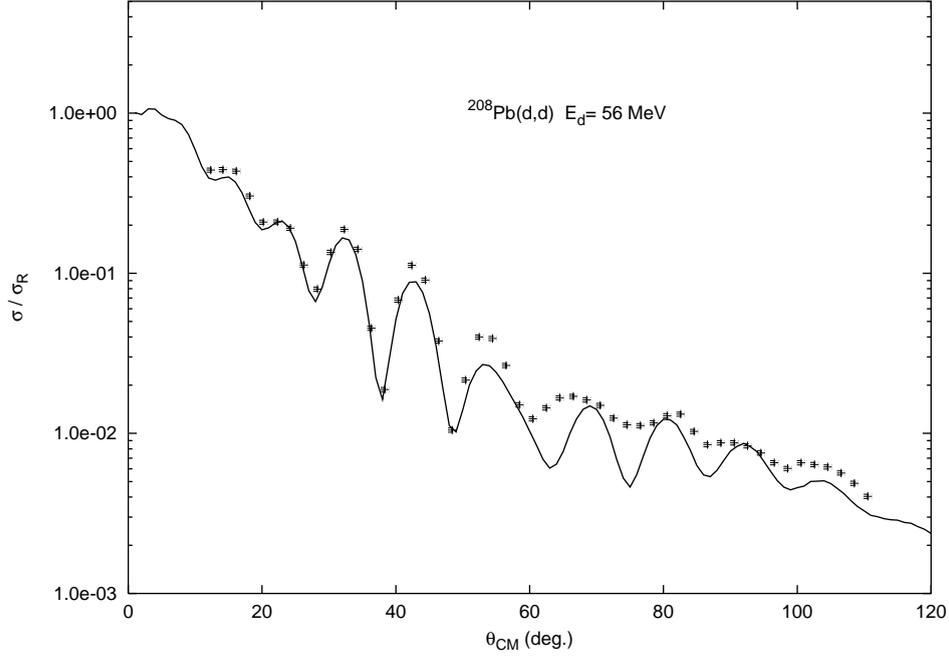
A reasonable reproduction can be seen. This is also true for the polarization observables. Phase relation, peaks and valleys of the angular distribution pattern, can be reproduced well by introducing the antisymmetrization correction.

Triple differential cross section $\dfrac{d^3\sigma}{d\Omega_n\, d\Omega_p\, dE_p}$ are calculated by the following relation,

$$\frac{d^3\sigma_{\nu_p\nu_n}}{d\Omega_n d\Omega_p dE_p} = \frac{2\pi}{\hbar v_{p+n-T}}|T_{fi}|^2\rho_1(E_p) = \frac{2\pi}{\hbar}\frac{\mu_{p+n-T}}{P_{p+n-T}}|T_{fi}|^2\rho_p(E_p). \tag{1}$$

Spin orientations of ν_p and ν_n are included in this expression. Proton state density $\rho_p(E_p)$ are given in the literature [6].

Expression of T-matrix (T_{fi}) is somewhat complicated because of the recoupling of p-n state wave functions and many angular momenta involved in the analysis and is not written here.

Triple differential cross sections measured by Okamura is a proton energy spectrum measured at $\theta_p = \theta_n = 0°$. At very forward angles, many partial waves interfere constructively and make a very sharp peak. Average over the proton and neutron detectors should be made to explain the experimental energy spectrum.
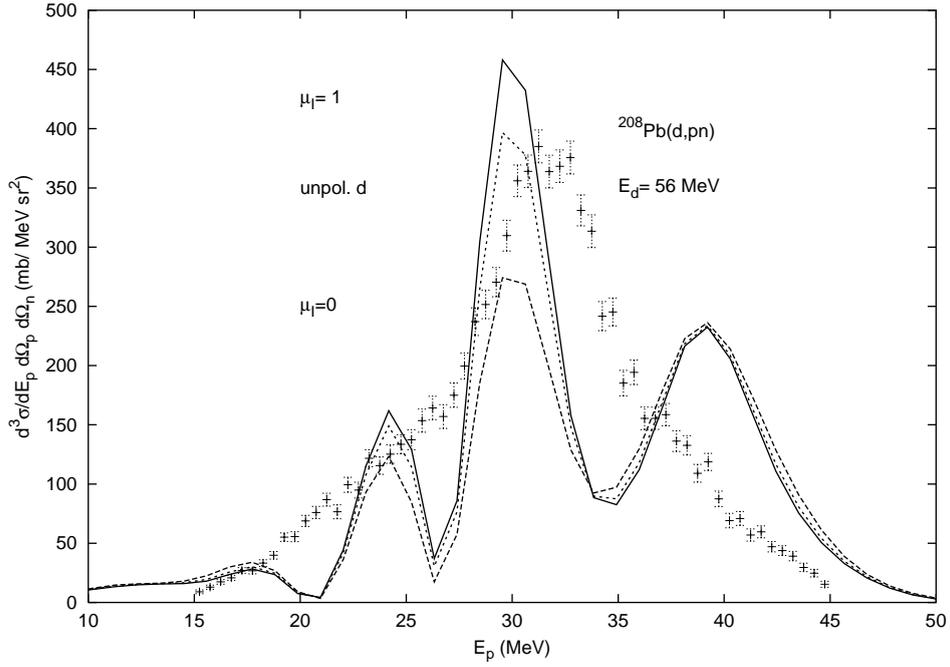
Fig. 2 compares the experimental data with the averaged triple differential cross sections for polarized and unpolarized deuterons. Polarization axis is along the beam direction.

One can see a large peak at $E_p = 30$ MeV, while experimental peak is located at about $E_p = 31\text{-}32$ MeV. Large valleys can be seen on both sides of the peak, which are not seen in the experimental data. The origin of these valleys can be ascribed to the destructive interference of nuclear and Coulomb contributions for this reaction. This statement can be confirmed by limiting the maximum angular momentum and drawing an energy spectrum.

Importance of continuum coupling can also be confirmed as follows.
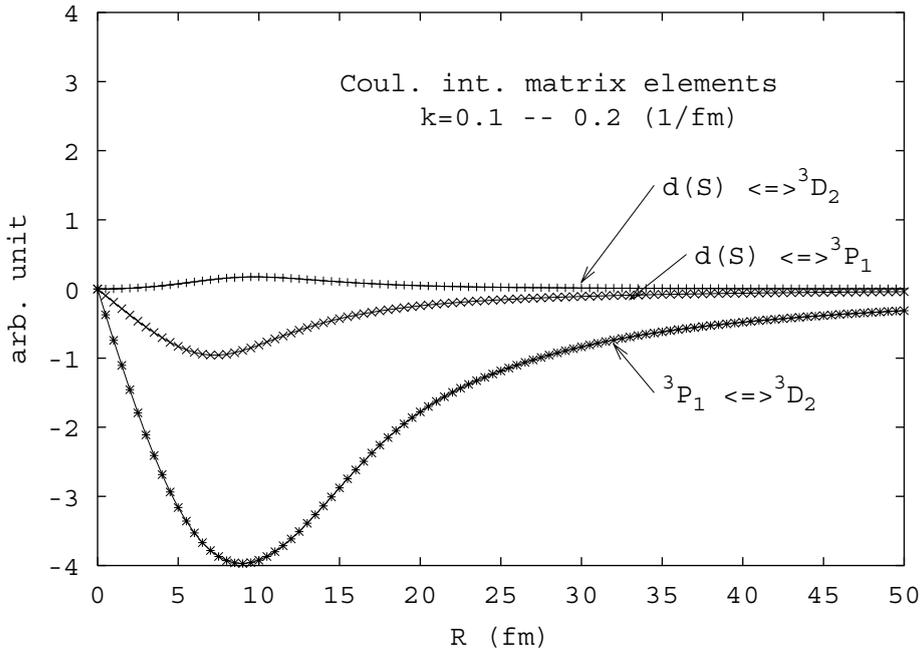
Fig. 3 compares three matrix elements, which connect three states in p-n system,the S-state of the

deuteron, $^3P_1$ and $^3D_2$. Wave number of these scattering states are $k_{p-n} = 0.1 - 0.2 fm^{-1}$. Continuum-continuum coupling, in this case, is much larger than the direct break up matrix elements. We can study the elastic break-up cross section by plotting the following quantity,

$$\frac{10\pi}{3K_{p+n}^2}(2J+1)|S^J(break-upchannel)|^2$$

By using this quantity, we can compare quantitatively at what J and to what breakup channel, the incident flux is actually directed. Ratio of positive to negative parity break up can be studied by changing the amplitudes of these off diagonal matrix elements.

References

1 M. Kamimura, M. Yahiro, Y. Iseri, Y. Sakuragi, H. Kameyama and M. Kawai, Prog. Theor. Phys. **89** 1986

2 R.V. Reid, Jr., Ann. Phys.**50**(1968) 411

3 R.L. Varner, W.J. Thompson, T.L. McAbee, E.J. Ludwig and T.B. Clegg, Phys. Rep. **201**(1991) 59

4 N.Matsuoka, H.Sakai, T. Saito, K. Hosono, M. Kondo, H. Ito, K. Hatanaka, T. Ichihara, A. Okihana, K. Imai, K. Nishimura, Nucl. Phys. **A455** (1986) 413

5 H.Okamura, A.Ishida, N. Sakamoto, O.Otsu, T. Uesaka, T. Wakasa, H. Sakai, T. Niizeki, H. Toyokawa, Y. Tajima, H. Ohnuma, M. Yosoi, K. Hatanaka and T. Ichihara, Phys. Rev. **C58** (1998) 2180

6 G.G. Ohlsen, Nucl. Instr. Meth. **37**(1965) 240.

2.7   Numerical evaluation of negative energy Coulomb wave functions

Y. Aoki, N. Okumura, H.Ishiguro

Negative energy scattering state Coulomb wave functions may be used to evaluate closed channel contribution in two-step analyses and to solve weakly coupled equations. It is defined by solutions of a following differential equation,

$$w''(\rho) = \left(1 + \frac{2\eta}{\rho} + \frac{\ell(\ell+1)}{\rho^2}\right) w(\rho).$$

It has two independent solutions. They are characterized by the following factors, $\exp\{\pm(\rho + \eta \log \rho)\}$. The one which has $-(+)$ exponent is denoted, in this note, by u_ℓ (v_ℓ). Numerical evaluation at large ρ is presented.

(1) Evaluation of $u_\ell(\rho)$

u_ℓ can be expressed as,

$$u_\ell(\rho) = \exp(-\rho - \eta \log \rho) g(a,b,\rho),$$

where

$$g(a,b,\rho) = \sum_{n=0}^{\infty} \frac{\Gamma(a+1)\Gamma(b+n)}{n!\,\Gamma(a+1-n)\,\Gamma(b)\,(2\rho)^n},$$

and abbreviations are used for $a = \ell - \eta$ and $b = \ell + \eta + 1$. $\Gamma(z)$ is a usual gamma function.

$g(a,b,\rho)$ satisfies the following basic relations,

$$g(a-1,b,\rho) = g(a,b,\rho) - \frac{b}{2\rho} g(a-1,b+1,\rho)$$

and

$$g(a,b+1,\rho) = g(a,b,\rho) + \frac{a}{2\rho} g(a-1,b+1,\rho).$$

Some useful relations are derived from these recurrence relations. Last term of the right hand side is closely related to the derivative, u'_ℓ. After some manipulations, ascending relation can be derived as,

$$u_{\ell+1} = \frac{1}{\ell+\eta+1}\left[\left\{\eta + \frac{\ell(\ell+1)}{\rho}\right\} u_\ell - (\ell+1)u'_\ell\right]$$

and

$$u'_{\ell+1} = -\left\{\frac{\eta}{\ell+1} + \frac{\ell+1}{\rho}\right\} u_{\ell+1} - \frac{\ell-\eta+1}{\ell+1} u_\ell.$$

Initial values of u_0 and u'_0 are calculated from power series expansion of $1/\rho$ for large ρ. Ten digit convergence is achieved for $\rho_c = 2.857 \times \eta + 12.706$. Telescoping by using the following recurrence relation for the n-th derivatives ($w^{(n)}$) is mad when ρ is smaller than ρ_c and $\ell = 0$.

$$w^{(n+2)} = \left(1 + \frac{2\eta}{\rho}\right) w^{(n)} + n(w^{(n-1)} - w^{(n+1)}).$$

(2) Evaluation of v_ℓ

v_ℓ may be written as,

$$v_\ell(\rho) = \exp(\rho + \eta \log \rho) f(\alpha,\beta,\rho),$$

where,

$$f(\alpha,\beta,\rho) = \sum_{n=0}^{\infty} \frac{(-1)^n \Gamma(\alpha+1)\Gamma(\beta+n)}{n!\,\Gamma(\alpha+1-n)\Gamma(\beta)(2\rho)^n},$$

$\alpha = \ell + \eta$ and $\beta = \ell - \eta + 1$. $f(\alpha,\beta,\rho)$ satisfies the following relations,

$$f(\alpha-1,\beta,\rho) = f(\alpha,\beta,\rho) + \frac{\beta}{2\rho}f(\alpha-1,\beta+1,\rho)$$

and

$$f(\alpha,\beta+1,\rho) = f(\alpha,\beta,\rho) - \frac{\alpha}{2\rho}f(\alpha-1,\beta+1,\rho)$$

Descending formulae for ℓ follow as,

$$v_\ell = \frac{1}{\ell+\eta+1}\left[\left\{\eta+\frac{(\ell+1)^2}{\rho}\right\}v_{\ell+1} - (\ell+1)v'_{\ell+1}\right]$$

and

$$v'_{\ell+1} = \frac{1}{\ell+1}\left[\left\{\eta+\frac{(\ell+1)^2}{\rho}\right\}v_\ell + (\ell-\eta+1)v_{\ell+1}\right]$$

Key values of v_ℓ and v'_ℓ can be evaluated as follows. We notice a recurrence relation for contiguous β and fixed α,

$$\left(1+\frac{\alpha+\beta+1}{2\rho}\right)f(\alpha,\beta+1,\rho) = f(\alpha,\beta,\rho) + \frac{\beta+1}{2\rho}f(\alpha,\beta+2,\rho).$$

This relation is converted to the following continued fraction,

$$f_\beta \equiv \frac{f(\alpha,\beta,\rho)}{f(\alpha,\beta+1,\rho)} = b_0 + \frac{a_1}{b_1+}\frac{a_2}{b_2+\cdots},$$

$$b_0 = 1 + \frac{\alpha+\beta+1}{2\rho} = 1 + \frac{\ell+1}{\rho},$$

$$a_n = -(\beta+n) = -(\ell-\eta+n+1),$$

and

$$b_n = 2\rho+\alpha+\beta+n+1 = 2(\rho+\ell+1)+n.$$

This continued fraction converges very fast for large ℓ.

By using the recurrence relations for $f(\alpha,\beta,\rho)$ and Wronskian relation $v'_\ell u_\ell - v_\ell u'_\ell = 1$, $v_\ell(\rho)$ and $v'_\ell(\rho)$ are written as,

$$v_\ell = \left[u_\ell\left\{1+\frac{1}{\rho}\left(\ell+1-\frac{\ell+1-\eta}{f_\beta}\right)\right\} - u'_\ell\right]^{-1}$$

and

$$v'_\ell = \left\{1+\frac{\ell+1}{\rho}-\frac{\ell+1-\eta}{\rho\,f_\beta}\right\}v_\ell.$$

All the logic is confirmed by checking the Wronskian relations for any ℓ.

Detailed derivation, in Japanese, and FORTRAN program (cwf.tex) can be downloaded from http://www.tac.tsukuba.ac.jp/~yaoki.

3.1 Equilibrium charge states of Cu, Br and I ions passing through Be foils

K.Shima, N.Okumura, H.Koubai, S.Ishii and K.Sasa

Charge distributions of energetic ions after the passage through thin foils differ by the atomic number Z_2 of foils. For ions of 28.5 and 59 MeV ^{19}F, 29-109 MeV ^{28}Si, 23.5-108.5 MeV ^{35}Cl and 117 MeV ^{63}Cu, equilibrium mean charges, q_b, were found to oscillate with Z_2 when q_b values are compared at a common projectile energy[1-3]. For all these ions and energies, the general characteristics is that the q_b values increase with decreasing Z_2 by showing an oscillatory behavior although the oscillatory behavior is not so remarkable in ^{19}F ions. Within the framework of investigated foils, ions after the passage through Be foil exhibited the highest q_b, and those after the passage through C foil exhibited the second highest q_b value.

In view of accelerator technology such as settling a charge stripper in the course of acceleration tube, it is very important to investigate the problem that the above mentioned fact of the Be foil exhibiting the most highly charged ions is true or not for any ion species. Actually, except for the case of 117 MeV ^{63}Cu, there has been no report on heavier ions than Cu after the passage through Be foils in tandem accelerator energy region [4]. In this report, projectile ion species and energy have been extended to 50-150 MeV ^{63}Cu, ^{79}Br, and ^{127}I ions, and equilibrium charge distributions have been measured after the passage through Be foil. In some cases of ions and energies, the charge distributions were also measured by using foils with some different Z_2.

The procedure to measure the charge distribution is described elsewhere [2]. After the passage through a self-supporting foil, the ions with charge state q were analyzed by using a magnetic spectrograph ESP-90, and are collected with a Faraday cup. On the other hand, the scattered ions or recoiled target atoms were detected with a surface barrier detector. Charge fraction F(q) for each q was obtained from the integrated beam current and the scattered or recoiled particle counts during the measurement.

Obtained results of equilibrium mean charges , q_b , are plotted in Figs.1-3 for Cu, Br, I ions after the passage through Be and C foils as a function of projectile exit energy from a foil, E. In the figures, present data as well as already reported data elsewhere [1,2,3,5,6] are shown.

Figs.1 to 3 demonstrate that even in the heavy ions of Cu, Br and I, the mean charges after the passage through Be foil, q_b(Be), are higher than those after the C foil, q_b(C), at about E>50 MeV for Cu and Br ions and E>100 MeV for I ions. Figures also show that the difference between q_b(Be) and q_b(C) increases with increasing E. Above mentioned two trends are similar to those observed in the lighter ions like F, Si or Cl [1-3]. On the other hand, It should be noticed that the trend of higher q_b values for lower Z_2 is also preserved at much higher E region than the present energy region of around 0.5-2 MeV/u. Gauvin et al. reported that the q_b values of 4.35 to 40 MeV/u Kr ions after the passage through Be, Al, Cu Ag, Au foils are higher for lower Z_2 [7]. Present information is useful in the construction of ion accelerator, particularly for the selection of the material charge strippers placed not only at the terminal of a tandem accelerator but also at some stages of the higher energy stages along the accelerated beam line.

References:

[1] K.Shima, Nucl. Instr. And Meth. B10/11 (1985) 45.

[2] K.Shima, T.Ishihara, T.Miyoshi, T.Momoi, and T.Mikumo, Phys. Rev. A29 (1984)1763.

[3] K.Shima, T.Ishihara, T.Momoi, T.Miyoshi, K.Numata and T.Mikumo, Phys. Lett. 98A (1983) 106.

[4] K.shima, S.Nagai and T.Ishihara, Nucl. Instr. and Meth. A244 (1986) 330.

[5] S.Datz, C.D.Moak, H.O.Lutz, L.C.Northcliffe and L.B.Bridwell, Atomic Data 2 (1971) 273.

[6] K.Shima, T.Mikumo and H.Tawara, At. Data and Nucl. Data Tables 34 (1986) 357.

[7] H.Gauvin, R.Bimbot, J.Herault and B.Kubica, Nucl.Instrum. and Meth. B47 (1990) 339.
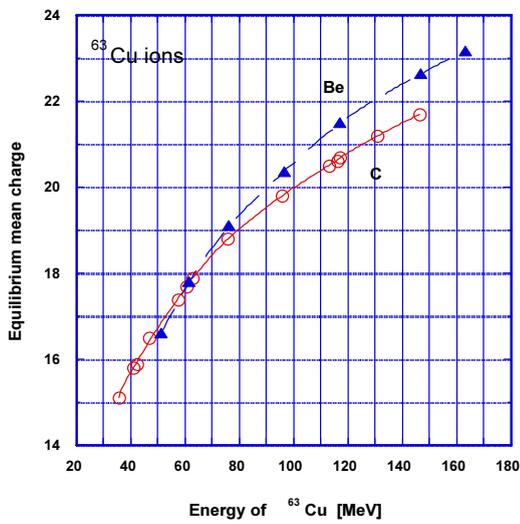
Fig.1. Equilibrium mean charge of Cu ions
passing through a Be or C foil.
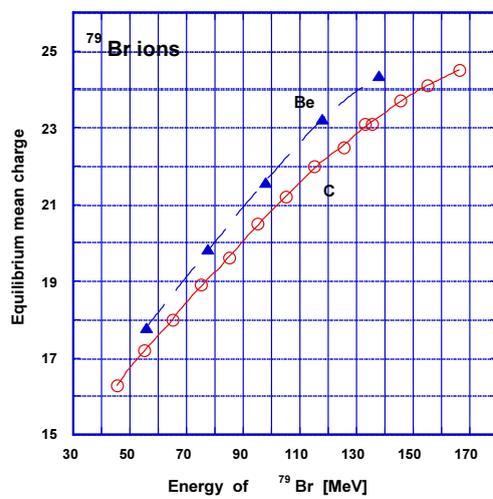
Fig.2. Equilibrium mean charge of Br ions
passing through a Be or C foil.
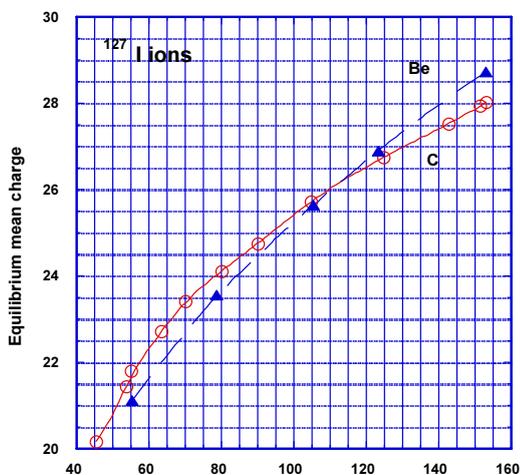
Fig.3. Equilibrium mean charge of I ions passing
through a Be or C foil.

3.2 Electron emission by fast cluster impact on solids

W. Iwazaki, T. Suguri, H. Kudo, Y. Saitoh[1], S. Yamamoto[1], K. Narumi[1], H. Naramoto[1]

When a solid target is bombarded by a fast atom-cluster beam, the atomic collisions near the surface are sometimes affected by the correlated impacts on a nano-sized area on the surface. They are different from those induced by impact of a single ion or a small molecule. Actually, fast cluster ions in the MeV/atom velocity range give rise to nonlinear radiation effects on solid targets with respect to the number of constituent atoms in the cluster n. This topic has been reviewed recently by Jacquet and Beyec [1], and by Parilis [2].

The nonlinearity has so far been reported for energy loss (stopping power) [3, 4], sputtering [5], lattice damage [6, 7, 8], secondary ion emission [9], and total electron emission yield (corresponding to the emission current) [10]. It is notable that the total electron emission yield per atom depends sublinearly on n. This is contrast to the radiation effects accompanying atomic displacements, i.e., sputtering or lattice damage, for which the n–dependence is stronger than linear.

The aim of the present study is to investigate the cluster effect in the ion-induced electron emission. Key information for the cluster-solid interactions will be included in the electron yield possibly at energies lower than $\sim$50 eV, which should reflect soft interactions of the cluster as a whole, rather than of the constituent atoms, with the target atoms. A better understanding of the cluster-induced electron emission would provide not only knowledge about the atomic and electronic processes of the cluster impact phenomena, but also an insight into the related effects resulting from energetic cluster-solid interactions. Such basic approach will also be of practical importance for future material processing by cluster impact.
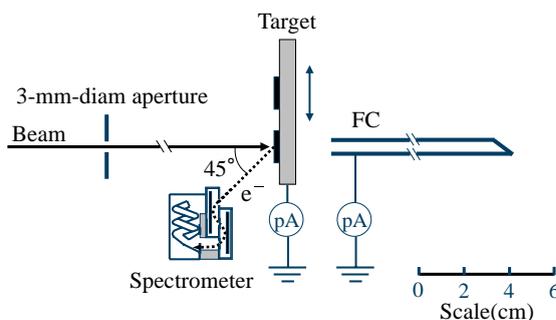
Fig. 1: Experimental setup.

The 0.5 MeV/atom C_n^+ ($n = 1, 4, 8$) beams obtained from the 3 MV tandem accelerator at JAERI-Takasaki were incident on the samples of evaporated Nb on alumina, pyrolytic graphite with cleaved (0001) surface, and chemically cleaned Si(100). The secondary electrons were measured at $135°$ with respect to the beam direction, using a $45°$ parallel-plate electrostatic spectrometer of the double-deflection type, as shown in Fig. 1. To reduce the influence of environmental magnetic field on the motion of low-energy electrons, the spectrometer was designed to be a smaller size than reported previously. The electron

---

[1]JAERI

measurements were carried out at room temperature under a pressure of $\sim 6 \times 10^{-6}$ Pa. The existence of contaminant atoms on the surfaces is anticipated under the present vacuum conditions. This should slightly change the transmission of outgoing electrons across the surface, but should not affect the n dependence of the electron energy spectra, which is of primary interest in the present studies.

The energy spectra of electrons presented here are raw data, i.e., the yield in the vertical axis is the number of electron signals counted. Accordingly, the spectra include no correction for the energy acceptance of the spectrometer, which is proportional to the electron energy, nor for the energy dependence of the efficiency of the electron multiplier. This is of minor importance in the analysis of the data because the measured electron yields for different experimental conditions are compared always at the same electron energy.
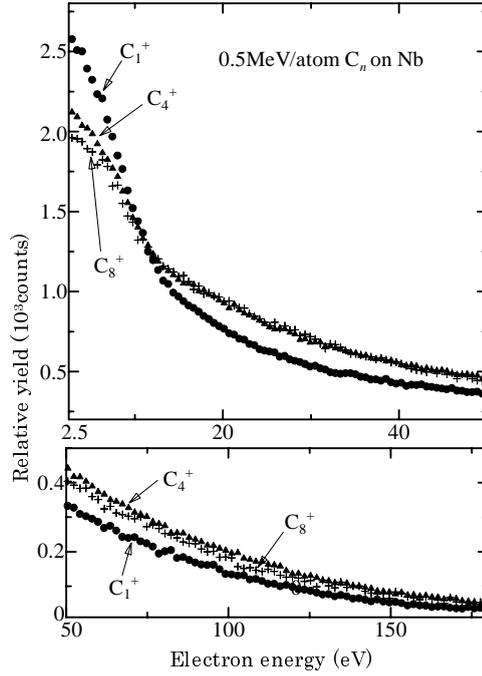
Fig. 2: Energy spectra of electrons emitted from Nb bombarded by 0.5 MeV/atom C_n^+ ($n = 1, 4, 8$).

Figure 2 shows an example of the energy spectra of electrons emitted from Nb bombarded by 0.5 MeV/atom C_1^+, C_4^+, and C_8^+. The electron yield was divided by n so that the spectra should be overlapped if the non-linear effect for the cluster ions is absent. Thererfore, the results obviously demonstrate the details of the nonlinear cluster effect, i.e., the difference in the spectrum shape, which has never been observed from the measurements of the total electron yield, so far reported. We see from Fig. 2 that the electron yield for C_4^+ and C_8^+ at energies lower than ~ 10 eV is suppressed by a factor of ~ 0.8, compared with that for C_1^+. At higher energies, on the contrary, the electron yield for the cluster ions is clearly enhanced.

The sublinear effect at energies lower than 10 eV is consistent with the reduction of the total electron yield, reported by the Orsay group, while the superlinear effect at higher electron energies has been found in the present work. This is probably due to the multi-stage scattering of the target electrons by the cluster ions, which should cause a higher-energy shift of the electrons that are ionized mainly by soft collisions. It should be noted that the superlinear effect have been obtained for 1.67 MeV/atom Au_1^+ and Au_3^+. Detailed

analysis of the results are now being carried out.

References

[1] D. Jacquet, Y. Le Beyec, Nucl. Instrum. Methods B 193 (2002) 227.

[2] E. Parilis, Nucl. Instrum. Methods B 193 (2002) 240.

[3] W. Brandt, A. Ratkowski, and R. H. Ritchie, Phys. Rev. Lett. 33 (1974) 1325.

[4] K. Baudin, A. Brunelle, M. Chabot, S. Della-Negra, J. Depauw, D. Gardes, P. Hakansson, Y. Le Beyec, A. Billebaud, M. Fallavier, J. Remillieux, J. C. Poizat, J. P. Thomas, Nucl. Instrum. and Methods B 94 (1994) 341.

[5] H. H. Andersen, A. Brunelle, S. Della-Negra, J. Depauw, D. Jaquet, Y. Le Beyec, J. Chaumont, H. Bernas, Phys. Rev. Lett. 33 (1998) 5433.

[6] M. Döbeli, R. M. Ender, U. S. Fischer, M. Suter, H. A. Synal, D. Vetterli, Nucl. Instrum. and Methods B 94 (1994) 388.

[7] H. Shen, C. Brink, P. Hvelplund, S. Shiryaev, PeiXiong Shi, J. A. Davies, Nucl. Instrum. and Methods B129 (1997) 203.

[8] J. R. Liu, X. M. Wang, L. Shao, H. Chen, W. K. Chu, Nucl. Instrum. and Methods B197 (2002) 101.

[9] A. Brunelle, S. Della-Negra, J. Depauw, D. Jaquet, Y. Le Beyec, and M. Pautrat, K. Baudin, H. H. Andersen, Phys. Rev. A 63 (2001) 022902.

[10] M. Fallavier, R. Kirsch, J. C. Poizat, J. Remillieux, J. P. Thomas, Nucl. Instrum. and Methods B 164-165 (2000) 920.

3.3 Low-energy electron emission from solids bombarded by fast dressed ions

T. Suguri, W. Iwazaki, C. Sakurai, S. Numazawa, I. Arano, H. Kudo

Low-energy electrons emitted from a solid surface bombarded by fast heavy ions reflect the screening effect of the charge-exchanged, dressed (not fully-stripped) ions passing through the surface layer. The present work provides comprehensive approaches to the pre-equilibrium charge states of the incident ions from the experimental data of the low-energy electron yield, the effective nuclear charges for the loss electron yield, and the binary-encounter electron yield reported previously.

The electron emission from fast dressed ions in collision with atoms has been one of the attractive phenomena in atomic collision studies [1]. The observation of the emitted electrons, in particular, the loss electrons, provides knowledge about the ionization processes in a reversed situation of the collision-induced ionization of a target atom in the laboratory frame. Indeed, the loss electron yield is maximal at a loss-peak energy E_{L}, which is equal to the kinetic energy of an electron moving at the same speed as the ion. The fundamental aspects of the loss electron yield have been studied experimentally and theoretically since its discovery in the 1970s. In these basic studies, the workers focused on the loss electron spectra resulting from an ion–atom single collision process which is realized in gas-target experiments.

For a solid target, loss electrons produced below the surface generally suffer elastic and inelastic scattering before they are emitted from the surface. Accordingly, the energy and angular distributions of the loss electron yield at a backward angle from a solid target are inherently degraded from those in the produced stage. This is probably one of the reasons that there are only a few related studies so far reported. For example, Koyama and coworkers studied the dependence of the loss peak energies for impact of 1.1 MeV/u He$^+$ on the atomic number of the metal targets [2]. Other related studies include those of convoy peaks by foil transmission experiments [3].

Since the loss electron yield results directly from the charge changing process of the incident ions, we may obtain knowledge about the evolution of the charge states of fast dressed ions from the analysis of the loss electron yield. Also, further knowledge will be provided from the low-energy electron yield which should reflect the effective charge state of the ion at the surface. Both approaches will be complementary for a detailed analysis of the charge changing process in a solid target. With these as a prospect, this paper reports experimental studies of pre-equilibrium charge states of fast ions in solids by electron spectroscopy combined with the ion channeling technique [4].

The 2.5 and 3.5 MeV/u C^{4+}, C^{6+}, O^{5+}, and O^{8+} beams obtained from the tandem accelerator at the University of Tsukuba were incident on chemically cleaned Si(110) and Ge(110) surfaces under a pressure of $\sim 1 \times 10^{-6}$ Pa. Only the $\langle 110 \rangle$ axial direction normal to the Si or Ge surface was chosen for the channeling measurements since the dependence of the electron spectra on the channeling direction is not of essential importance in the present study. The energy spectra of the ion-induced electrons were measured in the high (0.3–3.5 keV) and low (less than 30 eV) energy ranges. In the high-energy range, the spectra have been measured at $180°$ with respect to the ion beam direction, adopting the experimental setup similar to that described elsewhere [4].

In the low-energy range, the spectra have been measured at a backward angle of $135°$ using a $45°$
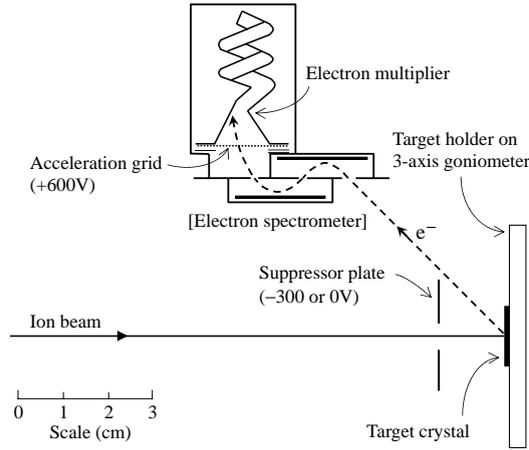
Fig. 1: Experimental setup for measurements of ion-induced electrons in the energy range below $\sim 30\,\mathrm{eV}$.

parallel-plate spectrometer of the double deflection type, as shown in Fig. 1. The post-acceleration field ($+600\,\mathrm{V}$) in the spectrometer was necessary to generate the signals of the low-energy electrons. The relative energy resolution of the spectrometer is $\sim 3\%$. During the measurements, the ion beam current was not monitored since the operation of the suppressor plate ($-300\,\mathrm{V}$) to repel back the emitted electrons is necessary for beam current measurements. Therefore, the measured electron yields without operating the suppressor were normalized using the beam current values, 0.7–0.8 nA, monitored with operating the suppressor. Typically, the fluctuation of the beam current was within $\pm 3\%$. The beam dose required for accumulating a spectrum was $\sim 3 \times 10^{14}$ ions/cm^2. The spectra were effectively reproduced even after 3 repeated cycles of the measurements.

It should be noted that the KLL Auger peaks due to C and O atoms on the crystal surfaces were slightly recognized, indicating existence of contaminants of effectively less than a monolayer, according to a comparison with the Auger peaks from reference targets. These light contaminant atoms should slightly change the transmission of outgoing electrons across the surface, but should not affect the input-charge dependence of the projectile or target ionization, which is of primary interest in the present studies.

The energy spectra of electrons presented here are raw data, i.e., the yield in the vertical axis is the number of electron signals counted. Accordingly, the spectra include no correction for the energy acceptance of the spectrometer, which is proportional to the electron energy, nor for the energy dependence of the efficiency of the electron multiplier. This is because the measured electron yields for different experimental conditions are compared always at the same electron energy.

Figures 2 and 3 show energy spectra of electrons induced by 2.5 and 3.5 MeV/u C^{4+} and C^{6+} under $\langle 110 \rangle$ and random (nonchanneling) incidence conditions of Si and Ge, measured at $180°$ with respect to the ion beam direction. The electron yields shown are normalized to the same number of incident ions. The enhanced electron yields at $\sim 1.5\,\mathrm{keV}$ for Si and at $\sim 1.0\,\mathrm{keV}$ for Ge are due to Si-KLL and Ge-LMM Auger electrons, respectively. We first estimate the background yield, consisting of the continuum and the Auger yields, on which the loss electron yield is superimposed. In Figs. 2 and 3, the electron yields for C^{4+} and C^{6+} for each pair of $\langle 110 \rangle$ and random cases are effectively equal at energies higher than
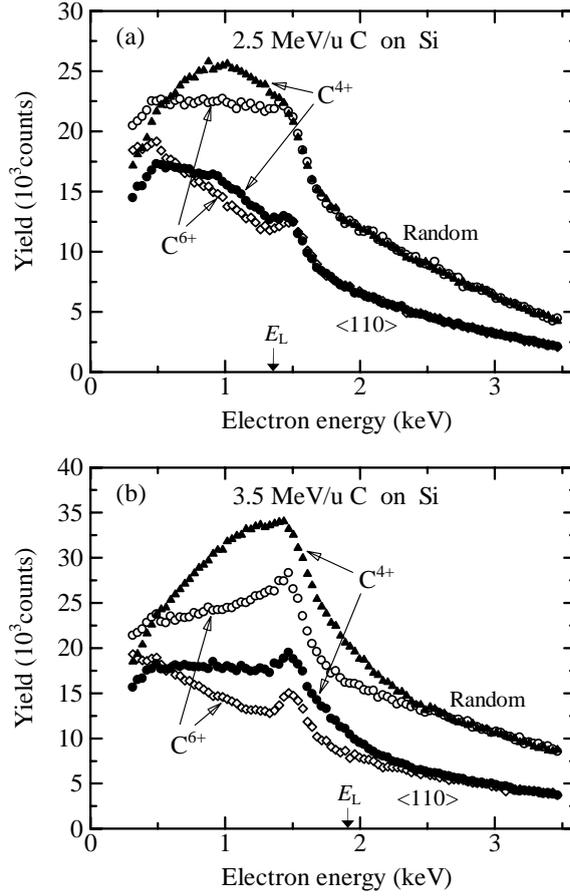
Fig. 2: Energy spectra of electrons emitted from Si bombarded by (a) 2.5 and (b) 3.5 MeV/u C^{4+} and C^{6+} under $\langle 110 \rangle$ and random incidence conditions. E_L indicates the loss-peak energy. The relative energy resolution of the spectrometer is $\sim 4\%$.

~ 2.0 and ~ 2.5 keV for the 2.5 and 3.5 MeV/u ions, respectively.[1] At other energies, the enhanced yields for C^{4+} over those for C^{6+} originate from the loss electrons from C^{4+}, including the cascade electrons generated by the primary lost electrons. However, care must be taken to use the spectra for C^{6+} as the background spectra for C^{4+}. Actually, at energies lower than ~ 0.5 keV the electron yield for C^{4+} is less than for C^{6+}. This results from the fact that at the low energies the background yield for C^{4+} is less than for C^{6+} because of the screened nuclear charge of C^{5+} in the pre-equilibrium stage, as will be discussed later. Therefore, the spectra for C^{6+} can be used for the background subtraction mainly at a high energy region of the spectra. Such reduction of the background yield due to the screened nuclear charge becomes serious for heavier ions. As a typical case, Fig. 4 shows the spectra for the pair of 2.5 MeV/u O^{5+} and O^{8+}, which are normalized to the same number of incident ions. These spectra should have similarities to those for the equal-velocity C ions, as anticipated from the binary-encounter model of ion-induced ionization [7, 1], which predicts that the spectrum shape is determined by the ion velocity. Thus, from a comparison of the corresponding pairs of the spectra shown in Fig. 4(a) and Fig. 2(a), also of Fig. 4(b) and Fig. 3(a), it is understood that the background yields for O^{5+} is appreciably reduced over the energy

---

[1]Precisely, the $\langle 110 \rangle$ yield for C^{4+} is greater than for C^{6+} by a factor of 1.02–1.07 at ~ 3 keV,[5, 6] although such a small difference is negligible in the present analysis.
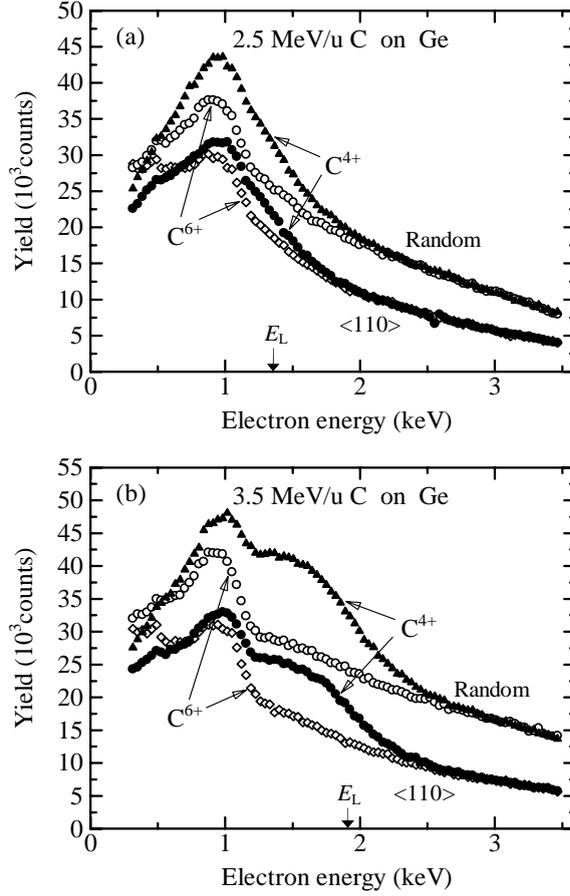
Fig. 3: Energy spectra of electrons emitted from Ge bombarded by (a) 2.5 and (b) 3.5 MeV/u C^{4+} and C^{6+} under $\langle 110 \rangle$ and random incidence conditions.

range up to ~ 2 keV, relative to those for O^{8+}, which is probably due to the pre-equilibrium O^{6+} state, as will be discussed later. In these cases, the background yields seriously deviate from the yield for O^{8+}. In the opposite case, i.e., for light ions such as He, for example, the spectrum for He^{2+} might be a reasonable alternative to the background yield of He^{+} [2].

Figure 5 shows the excess electron yields for 2.5 and 3.5 MeV/u C^{4+}, which were obtained by subtraction of the yield for C^{6+}. The peak energies of the excess yields are a factor of 0.7–0.9 less than the values of $E_L = 1.36$ and 1.91 keV for the 2.5 and 3.5 MeV/u ions, respectively, which is consistent with the experiments by Koyama and coworkers [2]. Figure 6 shows the ratios of $\langle 110 \rangle$ to random excess yield obtained from the data shown in Fig. 5. The ratio is constant near E_L and decreases with decreasing electron energy. The decreased ratio for the low-energy part of the excess yield results from the subtraction of the overestimated background yield, assumed to be that for C^{6+}, as noted earlier. The loss electron yield in the channeling case can therefore be characterized by the well defined value of the ratio near E_L. The ratios of $\langle 110 \rangle$ to random loss electron yield R_e, determined in this manner, are $R_e = 0.50 \pm 0.06$, 0.58 ± 0.05, 0.50 ± 0.07, and 0.60 ± 0.05 for 2.5 MeV/u C^{4+} on Si, 3.5 MeV/u C^{4+} on Si, 2.5 MeV/u C^{4+} on Ge, and 3.5 MeV/u C^{4+} on Ge, respectively.

The values of R_e obtained above can be used to determine the charge state of the C ions in the crystal.
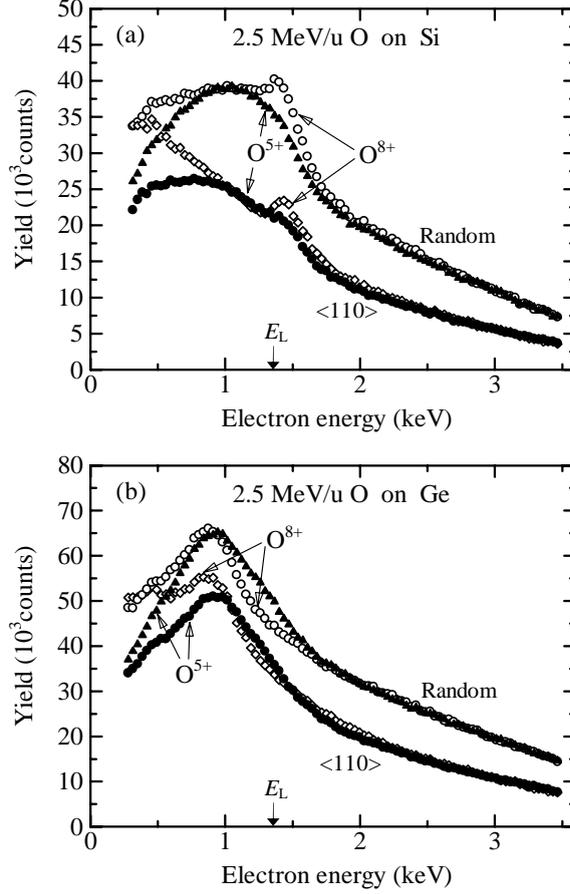
Fig. 4: Energy spectra of electrons emitted from Si and Ge bombarded by 2.5 MeV/u (a) O^{5+} and (b) O^{8+} under $\langle 110 \rangle$ and random incidence conditions.

Obviously, the present results of $R_e \simeq 0.5$ correspond to one- and two-electron loss of C^{4+} for the $\langle 110 \rangle$ and random incidence, respectively. Such simple correspondence is mainly due to the same order of ionization energies, I, of C^{4+} ($I = 392$ eV) and C^{5+} ($I = 490$ eV) [8]. The base width of the electron-loss peak for a gas target is approximately given by $4\sqrt{E_L I}$, according to Stolterfoht and coworkers [9]. Therefore, an electron ionized from a deeper atomic level of the projectile should contribute less to the enhancement of the loss electron yield near E_L, corresponding to a wider loss peak expected from the above formula. More detailed discussion of this effect must include escape processes of the electrons lost from the ion in the solid target.

In the following analysis, the effective nuclear charge of the C ion in the channeling case Z_C has been determined under the assumption that in the random case the C ions are fully stripped, as inferred above. This assumption is consistent with the charge-state data of fast ions passing through thin foils [10]. It is also notable that the assumption has been successfully used to determine the charge states of C ions in the crystals from the analysis of the binary-encounter electron yield [5, 6, 4]. In a simple treatment, $Z_C = 4$ if there is no electron loss from C^{4+} in the crystal, i.e., $R_e = 0$. Also, $Z_C = 6$ if C^{4+} is fully stripped near the crystal surface, i.e., $R_e = 1$, like in the the random case. Z_C can therefore be written as

$$Z_C = 4 + 2R_e . \tag{1}$$
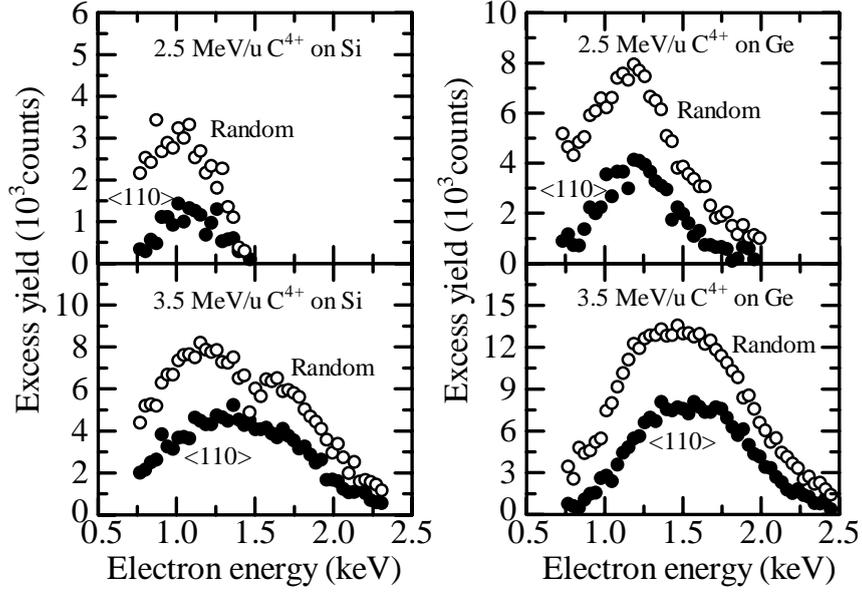
Fig. 5: Excess yield for C^{4+} obtained from subtraction of the yield for C^{6+}.

The values of Z_C determined using Eq. (1) are summarized in Table 1. An uncertainty in the values ± 0.1 stems from that of R_e. The values of Z_C are effectively equal to 5, which indicates that C^{5+} is the main charge state for $\langle 110 \rangle$ incidence of C^{4+} on Si and Ge.

Further knowledge on the charge states can be obtained from the low-energy spectra of the emitted electrons, according to Koyama and coworkers [11, 12, 3]. Figure 7 shows energy spectra of electrons emitted from Si bombarded by 2.5 MeV/u $C^{4+,6+}$ and 3.5 MeV/u $O^{5+,8+}$, together with the ratio of the yield α for the dressed to the fully stripped case. The spectra are normalized to a fixed number of the incident ion. In contrast to the loss electron yield, the low-energy electron yield showed no discernible change associated with ion channeling, within a statistical error of $\sim 2\%$ in the measured yield. This implies that the low-energy electrons are produced mainly by distant collisions with the target electrons. In a rough estimate, an average ion–electron distance for ionization of a target electron by a fast ion of velocity v is given by the adiabatic radius $\rho = v/(I + \varepsilon)$, where I and ε are the binding energy and the emission energy of the electron [9, 1]. For example, $\rho \simeq 1.4$ Å for ionization of Si L-shell electrons ($I \simeq 100$ eV for $L_{2,3}$ shell) under the condition of $\varepsilon \leq 30$ eV, corresponding to the present case shown in Fig. 7. This value is comparable to the interatomic distance in Si, which accounts for the absence of the channeling-related behavior of the low-energy electron yield, considering that (i) Si K-shell electrons make only minor contribution to the observed electron yield [4], and (ii) the ionization of widely distributed valence electrons should not suffer channeling effect. It is noticeable in Fig. 7 that α is constant, i.e., $\alpha = 0.70 \pm 0.02$ (at 15–27 eV) and $\alpha = 0.58 \pm 0.01$ (at 5–27 eV) for incidence of 2.5 MeV/u C^{4+} and 3.5 MeV/u O^{5+}, respectively. α is actually the low electron-energy limit of the ratios of the background yield both for the $\langle 110 \rangle$ and random cases. Similar results for Ge are shown in Fig. 8.

The ionization by distant collisions are caused by the screened Coulomb field of the partially stripped ion, and can be described in terms of the effective nuclear charge, i.e., an alternative point charge Z_{eff}. It is therefore expected that α is proportional to Z_{eff}^2 [3, 1]. We may assume that Z_{eff} is equal to the atomic
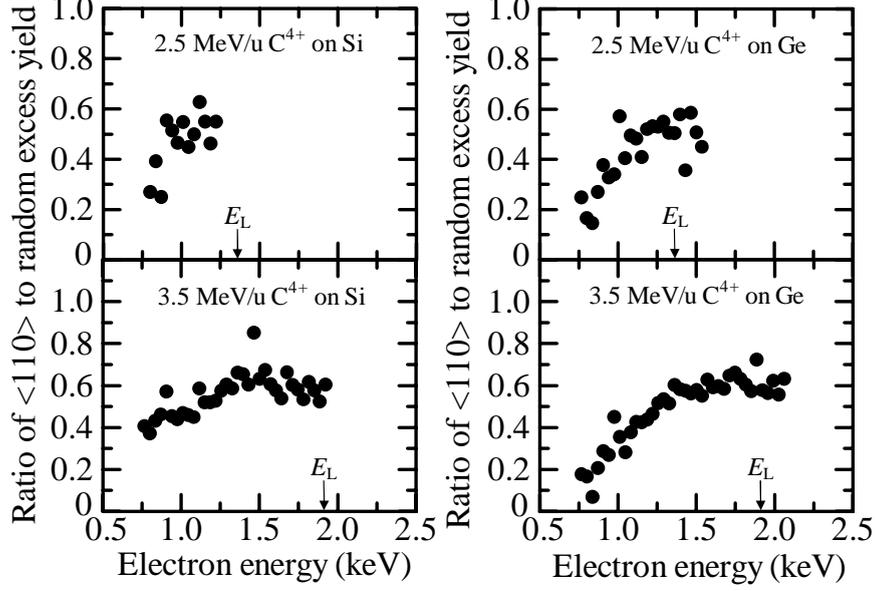
Fig. 6: Ratios of $\langle 110 \rangle$ to random excess yield, obtained from the results shown in Fig. 5. The loss-peak energies E_L are indicated.

Table 1: Comparison of Z_C, Z_{eff}, and Z_{eff}^* for $\langle 110 \rangle$ channeling in Si and Ge. The values of Z_C and Z_{eff} have been obtained in the present work, while those of Z_{eff}^* were obtained previously using the binary-encounter electron yield [5, 6, 4]. An estimated uncertainty in the values of Z_C, Z_{eff}, and Z_{eff}^* is roughly ± 0.1. Note that Z_{eff} is independent of the incident direction, i.e., channeling or random incidence, on the crystal target.

Projectile	Crystal	Z_C	Z_{eff}	Z_{eff}^*
2.5 MeV/u C^{4+}	Si	5.0	5.0	4.8
2.5 MeV/u C^{4+}	Ge	5.0	5.1	5.7
3.5 MeV/u C^{4+}	Si	5.2	5.3	5.1
3.5 MeV/u C^{4+}	Ge	5.2	5.4	–
3.5 MeV/u O^{5+}	Si	–	6.1	6.0

number of the ion Z_1 for incidence of the fully stripped 2.5 MeV/u C^{6+} and 3.5 MeV/u O^{8+}, since these are the most probable charge states for random incidence, as noted earlier. It follows that Z_{eff} for the partially stripped ion is given by

$$Z_{eff} = Z_1 \sqrt{\alpha} . \tag{2}$$

The values obtained from Eq. (2) are, for example, $Z_{eff} = 5.0 \pm 0.1$ and 6.1 ± 0.1 for incidence of 2.5 MeV/u C^{4+} and 3.5 MeV/u O^{5+} on Si, respectively, and are summarized in Table 1.

The evolution of the charge states of the ions can be deduced from a comparison among the three effective nuclear charges shown in Table 1, i.e., Z_C, Z_{eff}, and Z_{eff}^* which was determined previously from the binary-encounter electron yield produced under channeling incidence conditions [5, 6, 4]. Such an approach allows a comprehensive understanding of the experimental results because of the different character of the three effective nuclear charges. While Z_C directly corresponds to the average charge state,
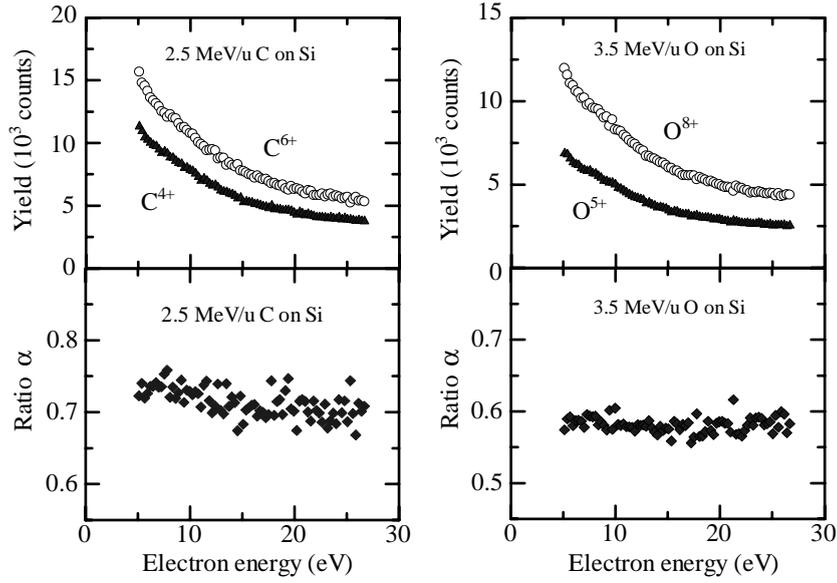
Fig. 7: Energy spectra of electrons emitted from Si bombarded by 2.5 MeV/u C and 3.5 MeV/u O ions, measured at 135° with respect to the beam direction. The yields are normalized to the same number of incident ions. Also shown are the ratios α of the yield for the dressed to the fully stripped case. Note that these spectra showed no discernible change associated with ion channeling.

Z_{eff} and Z_{eff}^* are associated with the screening of nuclear charges, and accordingly, they depend on the ion–electron or ion–atom distance of interaction for the observed phenomenon of interest. Also, Z_C and Z_{eff}^* are associated with stable charge states realized by the balance between the electron capture and loss processes, in contrast to Z_{eff} which probably reflects the pre-equilibrium stage of the incident ions.

The data shown in Table 1 indicate that in most cases the values of Z_C, Z_{eff}, and Z_{eff}^* are effecftively equal to 5. It is inferred from this fact that an incident C^{4+} mainly loses one electron in a thin surface layer and most of the target electrons are ionized by C^{5+}. C^{5+} loses one more electron in the random case, while it remains unchanged in the channeling case. A similar change in the charge state is anticipated for O^{5+}. The distance from the surface L, where the one-electron loss of the incident ion is completed, can be estimated by considering that Z_{eff}^* is characterized by the channeling orbits. The ion–atom glancing collisions starting from the surface, by which the channeling orbits are established, mainly occur from the surface to the depth L_1 where the close-encounter probability of ions with the aligned atoms decreases to 50%. L_1 can be evaluated from the computer simulations of channeling [13, 14], which allow to calculate the close-encounter probability as a function of distance along the axial direction. In the present case, the simulations conclude $L_1 \sim 40$ and 30 Å for Si and Ge, respectively.[2] Therefore, we may estimate $L \le 10$ Å in the actual case, from the condition of $L \ll L_1$. According to the previous analysis, $Z_{eff}^* \simeq 5$, i.e., the channeling orbits are established mainly by C^{5+}. It is therefore concluded that the frozen charge state of the channeled C^{5+} (and probably O^{6+}) is established not by the ion–atom glancing collisions, but predominantly by the quick freezing of the pre-equilibrium charge state at the surface.

Finally, an essential aspect of the low-energy electron yield from a solid target is pointed out. The

---

[2]These values can be obtained also from a universal curve of the simulation results, as given by Stensgaard and coworkers [15, 13].
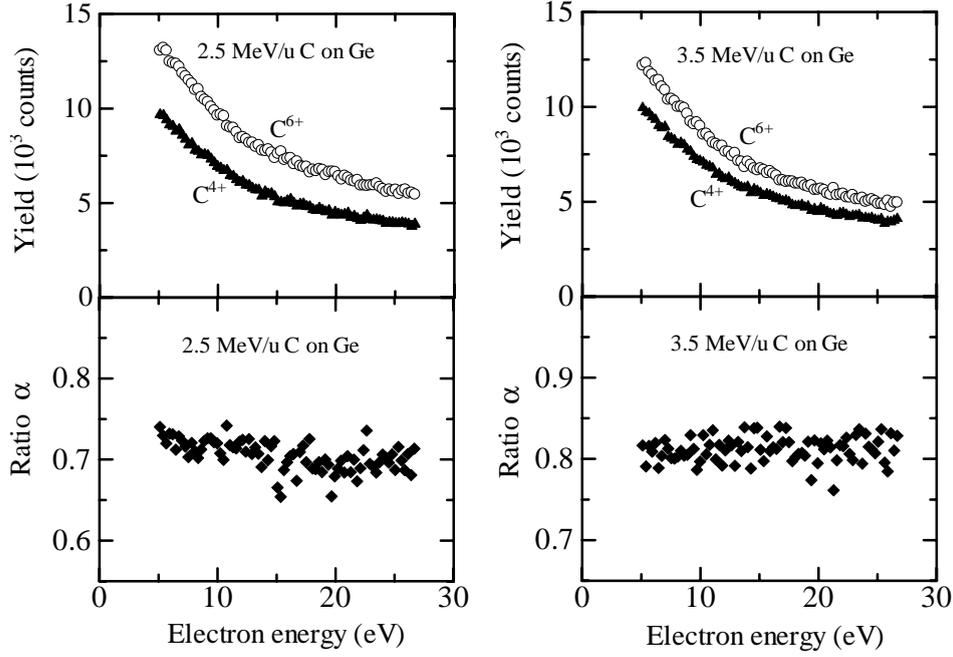
Fig. 8: Energy spectra and the ratios α of electrons emitted from Ge bombarded by 2.5 and 3.5 MeV/u C ions, measured at 135° with respect to the beam direction, shown similarly to Fig. 7.

present values of Z_{eff} do not agree with the input charges, in contrast to the experiments using gas targets. In fact, Stolterfoht and coworkers observed the 50–200 eV electrons produced by 30 MeV O^{q+} ($q = 4$–8) impact on O_2, and confirmed that the effective charge is equal to q [9, 1]. For solid targets, the disappearance of the electron yield that reflects the input charge state is due to the considerable contribution of the electron yield produced by the ionized ions. Surely, there must be low-energy electrons produced in the surface layer by the effective nuclear charge equal to the input charge (C^{4+} or O^{5+} in the present case). In the sublayer, however, the low-energy electrons are also produced by the ions losing one electron (C^{5+} or O^{6+}) and are emitted from the surface, in some cases, after suffering inelastic collisions. Therefore, the low-energy spectrum should include the electron yield corresponding to more than two charge states of the ions. It should be noted that for 10–20 eV electrons the mean free path for inelastic scattering is longer than 10 Å [16], which is larger than the value of L estimated earlier. This implies considerable mixing of the electron yield produced by the ions of the different charge states. Moreover, the sublayer should be thicker than the surface layer where the electron yield is produced by the ions of the input charge state, since the charge state varies towards the equilibrium less quickly with increasing the penetration distance. We can therefore expect larger contribution to the low-energy spectra of the electrons from C^{5+} or O^{6+} than from C^{4+} or O^{5+}, which accounts for the experimental results.

The present work has demonstrated the evolution of the charge state of partially stripped C and O ions near the surface. The frozen charge state of the channeled ions is established not by the ion–atom glancing collisions, but predominantly by the quick freezing of the pre-equilibrium charge state at the surface. It is notable that information obtained from the loss electron yield is essentially different from that obtained in terms of the effective nuclear charge, which is usually an alternative to the screened Coulomb field around

the ion, and cannot be directly related to the charge state.

Evidently, the charge-state analysis using loss electrons is applicable when the electron loss process plays a significant role in the evolution of the charge state in solids. For example, the present technique might allow a different type of observations of the resonant coherent excitation, rather than by usual transmission experiments [17], or by grazing scattering at a crystal surface [18].

References

[1] N. Stolterfoht, R. D. DuBois, R. D. Rivarola, *Electron Emission in Heavy Ion–Atom Collisions* (Springer, Berlin, Heidelberg, 1997), Sect. 6.4.

[2] A. Koyama, O. Benka, Y. Sasa, H. Ishikawa, M. Uda, Phys. Rev. B 36 (1987) 4535.

[3] D. Hasselkamp, H. Rothard, K.-O. Groeneveld, J. Kemmler, P. Varga, H. Winter, *Particle Induced Electron Emission II* (Springer, Berlin, Heidelberg, 1991).

[4] H. Kudo, *Ion-Induced Electron Emission from Crystalline Solids* (Springer Tracts in Modern Physics Vol. 175, Springer, Berlin, Heidelberg, 2002).

[5] H. Kudo, T. Fukusho, T. Ishihara, H. Takeshita, Y. Aoki, S. Yamamoto, H. Naramoto, Phys. Rev. A **50** (1994) 4049.

[6] H. Kudo, A. Tanabe, T. Ishihara, S. Seki, Y. Aoki, S. Yamamoto, P. Goppelt-Langer, H. Takeshita, H. Naramoto, Nucl. Instrum. Methods B **115** (1996) 125.

[7] M. E. Rudd, Y.–K. Kim, D. H. Madison, T. J. Gay, Rev. Mod. Phys. 64 (1992) 441.

[8] NIST Atomic Spectra Database, National Institute of Standards and Technology, http://www.physics.nist.gov/cgi-bin/AtData/main_asd.

[9] N. Stolterfoht, D. Schneider, D. Burch, H. Wieman, J. S. Risley, Phys. Rev. A **49** (1994) 5112.

[10] K. Shima, T. Mikumo, H. Tawara, At. Data Nucl. Data Tables **34** (1986) 357.

[11] A. Koyama, O. Benka, Y. Sasa, M. Uda, Nucl. Instr. and Meth. B 13 (1986) 637.

[12] A. Koyama, H. Ishikawa, Y. Sasa, O. Benka, M. Uda, Nucl. Instr. and Meth. B 33 (1988) 338.

[13] L. C. Feldman, J. W. Mayer, S. T. Picraux, *Materials Analysis by Ion Channeling* (Academic, New York, 1982) Chap. 1.

[14] J. S. Williams, R. G. Elliman: *Ion Beams for Material Analysis*, ed. by J. R. Bird, J. S. Williams (Academic Press, Sydney, 1989) Chap. 6.

[15] I. Stensgaard, L. C. Feldman, P. J. Silverman, Surf. Sci. 77 (1978) 513.

[16] M. P. Seah, W. A. Dench, Surf. Interface Anal. 1 (1979) 2.

[17] H. F. Krause, S. Datz, Adv. At. Mol. Opt. Phys. 37 (1996) 139.

[18] C. Auth, H. Winter, Phys. Rev. A 62 (2000) 012903.

3.4   Elastic recoil detection analysis of polyimide-based layers fabricated on Si

S. Numazawa, H. Kudo, and S. Ishii

For fablication of thin polymer layers on substrates, it is of essential importance to investigate the hydrogen and, in some cases, deuterium content as added marker atoms. Elastic recoil detection analysis (ERDA) using a MeV ion beam might be one of the most suitable analysis techniques for the composional studies of H and D [1, 2], if it can be applied under low beam damage on the polymer structure. The feasibility of ERDA for polymer layers can reasonably be inferred from the recent compositional analyses of polymer layers of micrometer thickness by Rutherford backscattering of MeV light ions [3, 4]. The present work demonstrates ERDA determination of the relative numbers of H and D atoms contained in the polyimide-based layers which are under development as low-k–dielectric as well as moisture-resisted coating materials for use in microelectronics.

The samples were prepared by spin coating of polyimide (PI) and polyamic acid (PAA) on Si(100) substrates. In the coating layers, H atoms are partly replaced by D atoms as a marker for the fablication processes. The thicknesses of the polymer layers are ∼60 nm, estimated from the spin-coating conditions.
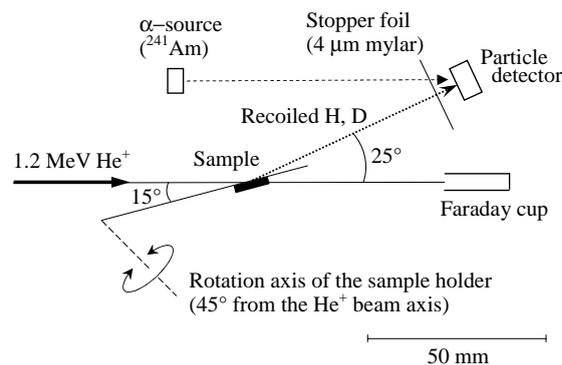
Fig. 1: Experimental setup for ERDA.

The experimental setup in the vacuum chamber is schematically illustrated in Fig. 1. The beam of 1.2 MeV He$^+$ from the Tandetron accelerator is incident on the sample at 15° relative to the sample surface, and the recoiled H or D atoms are detected at a recoil angle of 25°. The presssure in the chamber was 1.5×10^{-5} Pa during the experiments. The samples were fixed on the surface of the conical sample holder, whose conic axis, i.e., the rotation axis, is at 45° from the beam axis (Fig. 1). By rotating the sample holder, ERDA for different samples can be carried out under the same geometrical conditions.

A mylar film of 4 μm thickness was used as a filter for the solid-state particle detector, so that it stops the scatterd He ions, while it is transparent for the recoiled H and D because of the smaller stopping powers than for the He ions by a factor of ∼0.2. The ^{241}Am α source, which emits 5.48 MeV He^{2+}, was used for calibration of the particle detector. The energy resolution of the detector is ∼15 keV for 5.48 MeV He^{2+}. The beam spot on the target is a rectangular area of 1 mm×2 mm. The beam current during the

measurements was ∼1.3 nA, which was often monitored by the Faraday cup, shown in Fig. 1, by rotating the sample holder to a position off from the beam path.
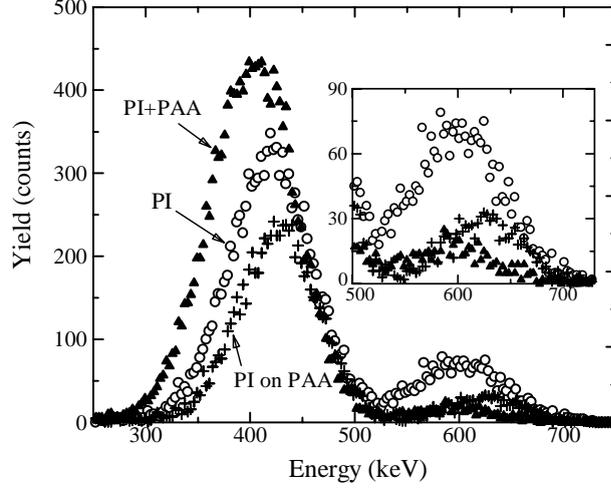
Fig. 2: Energy spectra of the recoiled H and D from the "PI", "PI+PAA", and "PI on PA" samples. The inset shows the magnified yield at 500–730 keV.

The energy spectra of the recoiled H and D are shown in Fig. 2. The three spectra correspond to (i) a 60 nm-thick PI layers ("PI"), (ii) a blended 60 nm-thick layer of PI and PAA ("PI+PAA"), and (iii) a double layer of 48 nm thick PI on 12 nm thick PAA ("PI on PAA"). The stoichiometries of the layers are C:N:O:H:D=52:6:13:16:13 for PI, C:N:O:H=47:4:13:36 for PAA, and C:N:O:H:D=47:5:13:33:2 for PI+PAA. It should be noted that the dependence of the spectrum on the beam dose has been measured (for an interval of $\sim 10^{13}$ He$^+$/cm^2) to investigate the influence of the radiation effects. However, the spectra showed no discernible change within the present beam dose up to 2.4×10^{14} He$^+$/cm^2, which is required to measure each of the spectra shown in Fig. 2.

The two peaks at 300–500 and 520–680 keV in the observed spectra, corresponding to H and D, respectively, are clearly resolved under the present experimental conditions. For the three H peaks, the full width at half maximum is effectively equal (~ 100 keV width), corresponding to the layers of ~ 60 nm thickness on Si. Furthermore, the D peak for the "PI on PAA" sample is located on the higher energy side than for the other samples, reflecting the distribution of D in the upper PI layer only. In contrast, D is distributed throughout the blended layer (PI+PAA), indicating that PI and PAA are well mixed. Obviously, the effective depth resolution of the order of 20 nm has been obtained in the present analysis.

The area under the peak is proportional to the number of H or D contained in the layer(s), and also to the Rutherford recoil differential cross section dσ/dΩ with respect to the solid angle Ω. Accordingly, the ratio of the number of D to H atoms contained in the layer $R_{D/H}$ is given by,

$$R_{D/H} = \frac{S_D(d\sigma/d\Omega)_H}{S_H(d\sigma/d\Omega)_D} , \tag{1}$$

where S_H and S_D are the areas under the peaks for H and D in Fig. 2, respectively. Since dσ/dΩ depends on the the mass $M_{H,D}$ of the recoiled atom as $(1+M_{H,D}/M_{He})^2$, where $M_{He} = 4$ is the mass of the projectile,

Table 1: ERDA results of the ratios of D to H contents, $R_{D/H}$, for the fabricated layers of PI, PI+PAA, and PI on PA. The values of $R_{D/H}$ anticipated from the stoichiometries of PI and PAA are also shown in the pharentheses.

Sample	$R_{D/H}$	
PI	0.64 ± 0.02	(0.81)
PI+PAA	0.101 ± 0.003	(0.061)
PI on PAA	0.33 ± 0.015	$(---)$

it follows that

$$R_{D/H} = (25/9)(S_D/S_H) \,. \tag{2}$$

It is also pointed out that from the mass dependence of $d\sigma/d\Omega$, noted above, ERDA in the present case is less sensitive to D than H by a factor of $9/25$.

The analysis results using eq. (2) are summarized in Table 1, together with the content ratios of H and D anticipated from the stoichiometries, noted earlier, for comparison. The uncertainty in the values of $R_{D/H}$ mainly stems from the separation of the slightly overlapped tails of the H and D peaks at 520–530 keV, seen in Fig. 2. Usually, ERDA requires careful check for the background H yield which results mainly from the residual hydrocarbons and water in the vacuum. In the present case, background H yields corresponding to typically 2–3% of the measured H in the polymer layers have been detected for chemically cleaned Si. Such a background, however, causes only minor influence (within the uncertainty shown in Table 1) on the present results. The present characterization has concluded that the values of $R_{D/H}$ estimated from the stoichiometry are appreciably deviated from the values determined by ERDA. ERDA thus allows structural studies of multi-layered polymers using D as a marker. Evidently, the direct detection of H and D by ERDA is of essential advantage for controlled polymer-layer processing.

References

[1] *Ion Beams for Material Analysis*, ed. by J. R. Bird, J. S. Williams (Academic Press, Sydney, 1989), pp. 144-148.

[2] *Handbook of Modern Ion Beam Materials Analysis*, ed. by J. R. Tesmer, M. Nastasi (Materials Research Society, Pittsburgh, 1995).

[3] T. E. Shearmur, D. W. Drew, A. S. Clough, M. G. D. van der Grinten, A. T. Slark, Polymer **37** 2695 (1996).

[4] N. Sundararajan, C. F. Keimel, N. Bhargava, C. K. Ober, J. Opiz, R. D. Allen, G. Barclay, G. Xu, J. Photopolym. Sci. Technol., [**12**) 457 (1999).

3.5 ^{57}Fe Moessbauer study of α' iron-nitride

T. Koyano, E. Kita, T. Ohba[1], H. Ohtsuka[2] and H. Wada[2]

Magnetization of iron nitrides in bct structure, α' [1] and α" [2] phases, has attracted much attention after Kim and Takahashi reported "giant magnetization" of the α" phase [3].   Thin film technique such as MBE and sputtering successfully produced single crystal or single phase samples of iron nitrides [4-7], but substantial confusion still exists in value of magnetization for the α" phase.   In order to shed a light into this argument over 30 years, magnetization measurement for bulk samples is best suited, but no single phase sample of α' or α" is obtained yet.   Therefore, it is necessary to estimate mass fraction of phases in samples as precise as determination of gross magnetization.

The nitrogen atoms in Fe-N alloys occupy the octahedral interstitial sites in the same manner as carbon atoms do in the Fe-C steel [1].   The austenite (γ) phase with fcc structure spontaneously undergoes the fcc -> bct Martensitic transformation when it is quenched below the Ms temperature, and the α' phase is formed.   Because nitrogen atoms in γ phase are randomly dispersed on the octahedral sites in the fcc matrix with some interaction among solute atoms and the transformation proceeds without diffusion process, nitrogen atoms are also irregularly distributed on corresponding sites in the α' phase.   Heat treatment at 120 C orders interstitial nitrogen atoms and the α" phase is formed [2].   It can be said the α' phase is precursor to the α" phase.   The Martensitic transformation accompanies a large atomic volume increase causing substantial internal stress in the matrix, which suppresses further development of the structure change.   This mechanism immediately tells us why the γ phase always remains in the sample as far as high nitrogen γ phase is concerned, and single phase sample of α' can not be obtained when one just cooled the γ phase below its Ms temperature.   Because a change in magnetization upon α" phase formation can not be analyzed properly without having a correct value of magnetization for the α' phase, determination of γ phase amount is of vital importance to elucidate whether the giant magnetization exists or not.

We have applied static external magnetic field up to 35 T on the γ phase at low temperatures to increase the volume fraction of the α' phase [8-10].   Magnetic field lowers the Gibbs' free energy of ferromagnetic α' phase whereas no substantial change takes place for paramagnetic γ phase.   Obviously, this drastic change in free energy drives the transformation.   With combining X-ray diffraction and magnetic measurement data, we have proved 35 T of field at 4.2 K reduces residual austenite to less than a quarter of the amount at zero magnetic field.

From point of view of ^{57}Fe Moessbauer spectroscopy, the γ and α' phases are unambiguously distinguishable.   Spectrum for γ phase is a combination of a singlet and quadrupole doublets whereas the α' phase spectrum consists of sets of magnetic sextet.   As well known in the theory for resonant absorption of γ-ray,   energy integral of an absorption line is proportional to the number of resonant

---

1 Department of Material Science, Shimane Univ., Matsue, Shimane, 690-8504 Japan.

2 National Institute for Materials Science, Sakura, Tsukuba, Ibaraki 305-0003 Japan.

nuclei in ideally thin absorbers.   Therefore, the mass fraction of the γ phase can be measured with transmission Moessbauer spectrum.   In this report, we analyzed Moessbauer spectra of α' + γ phase samples in order to determine the amount of residual austenite as a function of applied magnetic field at 4.2 K.

Commercially available iron foils (0.01 mm in thickness, 10 mm x 10 mm in size, and 99.8 % in purity) were annealed at 1270 K in dry hydrogen gas to decaburize and grain growth for 1 hour, and successively nitrified with a mixture of NH_3 and H_2 gas at 923 K for 1 hour.   Foil thickness and annealing time were optimized to assure composition homogeneity in samples.   Nitrified samples were subsequently quenched into distilled water without having contact with the air, and single phase sample of γ was obtained.   The γ phase samples were cooled to 4.2 K in zero magnetic field, and external magnetic field was applied in the foil plane as to minimize demagnetizing factor.   A Bitter type magnet was used to generate magnetic field of 0 < B < 23 T.   For experiments above 23 T, a hybrid magnet consisting of 14 T superconducting and 21 T Bitter type magnet was employed. ^{57}Fe Moessbauer spectra were recorded at room temperature using a constant acceleration type spectrometer in conventional transmission geometry and ^{57}Co source in Rh matrix.   Velocity scale was calibrated with pure α-Fe at room temperature.

Figure 1 shows Moessbauer spectra for α' + γ phase samples as a function of applied magnetic field at 4.2 K.   A prominent paramagnetic absorption is observed for the γ phase around zero velocity in B = 0 T sample besides convolution of many magnetic sextets originating in the α' phase.   As can be seen in the figure, the γ phase absorption becomes weaker with increasing applied magnetic filed in good accordance with our X-ray diffraction data published earlier [8-10].   The spectra were analyzed with a least squares fitting software with an assumption of Lorentzian line shape and thin absorber approximation.   As mentioned above, both γ and α' phases possess disordered structure and variety of local environment for Fe atoms exists.   Oda et al. pointed out that the γ phase spectrum needs to be analyzed with a singlet plus two doublets [11].   Due to weak intensity of the second doublet, we analyze our data with a combination of a singlet and a symmetric doublet.   Absorption profile of the α' phase is very complicated and characterized with broad line width as expected from disordered structure.   We employed seven sets of sextets with the first order (magnetic + quadrupole) interaction, whose initial values of hyperfine field for fitting range from 28.6 T to 38.3 T.   Absorption area ratio of individual lines in each sextet was assumed to be 3:x:1:1:x:3 for possible shape anisotropy effect, and all sextets were constrained to have the same value of x.   With this model, all spectra were properly analyzed as shown in Fig. 1.   Here, we focus our interest to absorption area ratio of the γ phase.   Figure 2 shows its dependence on applied magnetic field at 4.2 K.   The data for magnetization is taken from ref. 10 and plotted together.   The absorption area ratio of the γ phase monotonically decreases with increasing magnetic field in consistent with magnetization data.   The absorption area ratio of the γ phase at 35 T is 6.6 %, and corresponds to gross magnetization of 215 emu/g, assuming magnetization of 230 emu/g for the α' phase.   This is in good agreement with magnetic measurements.   It should be noted that the area ratio stays finite even at 35 T, and we need much stronger magnetic field to obtain single phase of γ.   Unfortunately, the strongest steady field in the world is 45 T and seems not enough for this particular purpose.

We concluded that α' phase possesses magnetization of 230 emu/g not only in thin films but also in

bulk sample. This means a new bulk material having larger magnetization than pure iron can be synthesized from iron and nitrogen, provided if one find out a method to reduce the residual austenite further.

References

[1] K. H. Jack, Proc. R. Soc. London, Ser. A 208, (1951) 200-215.

[2] K. H. Jack, Proc. R. Soc. London, Ser. A 208, (1951) 216-224.

[3] T.K.Kim and M.Takahashi: Appl. Phys. Lett., 20, (1972) 492-494.

[4] Y. Sugita, H. Takahashi, M. Komuro, K. Mitsuoka, and A. Sakuma, J. Appl. Phys., 76, (1994) 6637-6641.

[5] Y. Takahashi, H. Shoji, and M. Takahashi, J. Magn. Magn. Mater, 210, (2000) 333-340.

[6] S. Okamoto, O. Kitakami, Y. Shimada, J. Magn. Magn. Mater., 208, (2000) 102-114.

[7] K. Nakajima and S. Okamoto, Appl. Phys. Lett., 56, (1990) 92-94.

[8] T. Koyano, H. Ikeda, R. Yoshizaki, and A. Tasaki, J. Magn. Soc. Jpn., 22, (1998) 1069-1073.

[9] T. Koyano, H. Ikeda, R. Yoshizaki, K. Uehara, A. Tasaki, H. Ohtsuka, T. Takamasu, H. Wada, G. Kido, and T. Ohba, Mater. Trans., JIM., 41, (2000) 923-927.

[10] T. Koyano, T.Nomiyama, H. Ikeda, N.Kanoh, T.Ohba, H. Ohtsuka, and H. Wada, Mater. Res. Soc. Jpn (2003) in press.

[11] K. Oda, K. Umezu, and H. Ino, J. Phys. Condens. Matter., 2, (1990) 10147.
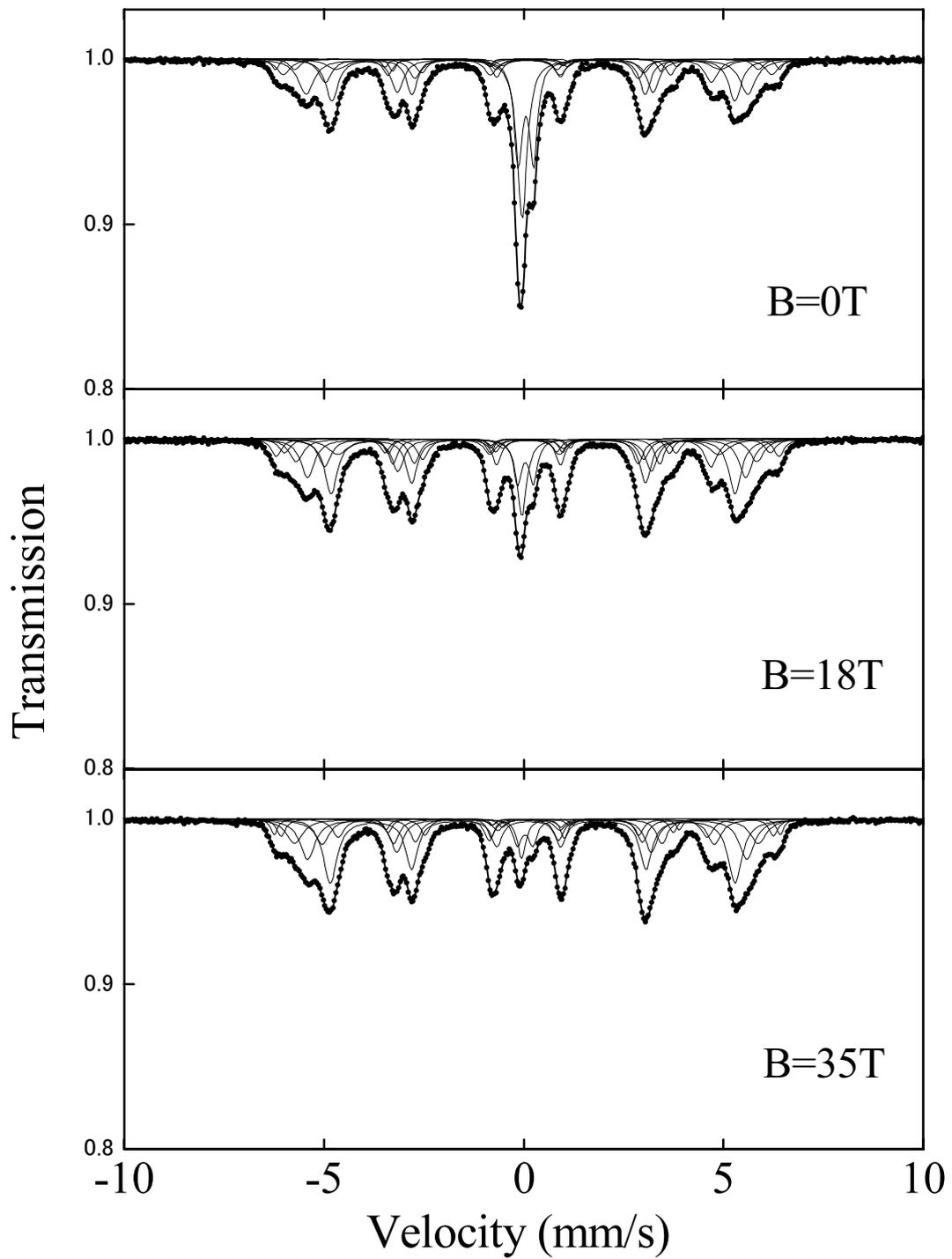
Fig. 1 ^{57}Fe Moessbauer spectra of α' + γ phase samples as a function of applied magnetic field at 4.2K.
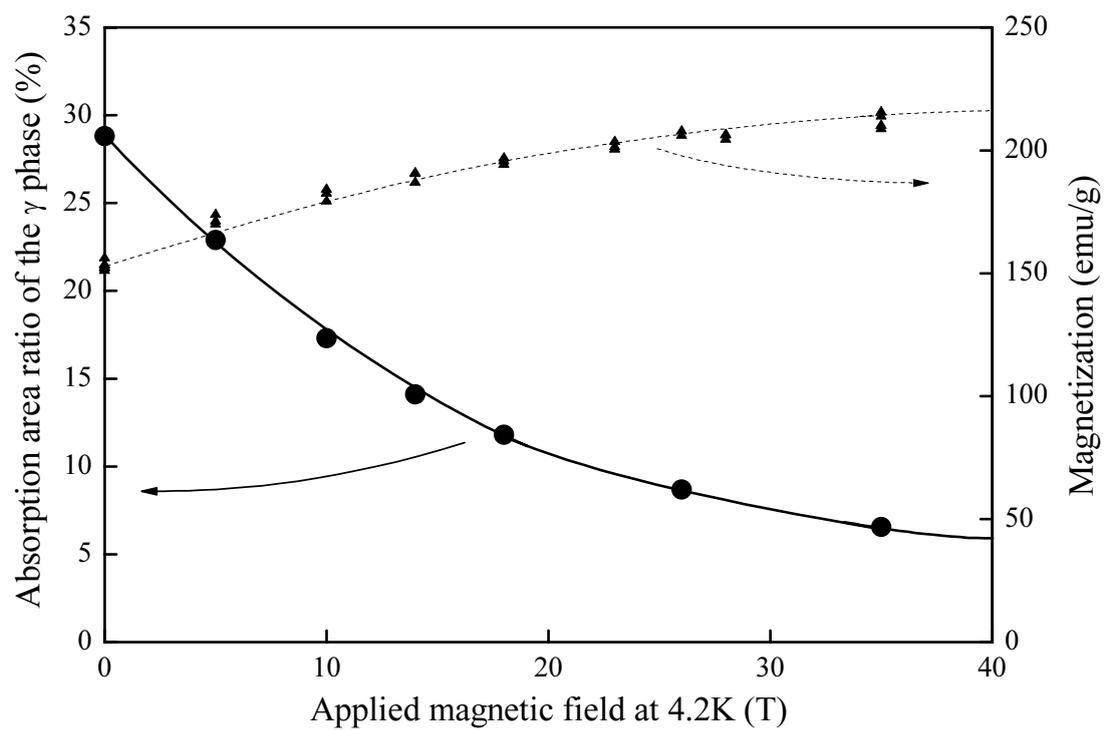
Fig. 2   Absorption area ratio of the γ phase (solid line) and magnetization (dashed line) plotted against applied magnetic field at 4.2K.   Magnetization data are taken from ref. 10.

3.6 Characteristic mechanical properties of high-density nanocrystalline FCC metals

H. Tanimoto, T. Yamada, N. Yagi, H. Mizubayashi,

1. Introduction

Whereas an increased volume fraction of the grain boundaries (GBs) may modify the properties of nanocrystalline (n-) materials, the present knowledge on the GB regions is very limited. Recent mechanical studies on high-density n-metals reveal that the Young's modulus of n-metals is not much lower than that of the conventional polycrystalline (poly-) metals [1-3]. For example, the Young's modulus of the high-density n-Au at 10 K is almost the same to the value of poly-Au after taking into account the crystalline texture [3]. In contrast, it is found that the anelastic strains revealed for the strain, ε, range above 10^{-4} in the prolonged time scale of the order of 10^4 sec, start to strongly increase above 200 K, where the slow anelastic process in the GB regions is excited [4]. On the other hand, the increase in the anelastic strain above 200 K is also found in the dynamic measurements at 10^2 Hz, where the fast anelastic process in the GB regions is excited. The magnitude of the fast anelastic process is much lower than that of the slow anelastic process. We surmise that the fast anelastic process is associated with the simple underlying anelastic processes in the GB regions. In the present work, we pursued the fast anelastic process by means of the vibrating reed method at about 200 Hz. That is, we measured the strain amplitude dependence (SAMD) of the resonant frequency, f, and the internal friction, Q^{-1}, and effects of the low temperature irradiation of 2 MeV electrons or 20 MeV protons on them.

2. Experimental Procedure

High-density n-Au ribbons 0.02 ~ 0.1 mm thick, 1 mm wide and 23 mm long were prepared by the gas-deposition (GD) method [3]. The density was measured by the Archimedes' method using high-purity ethanol, indicating that the relative density to the theoretical value (ρ/ρ_0) is more than 99 %. The mean grain size, d, estimated from the peak broadening of the X-ray diffraction was about 20 ~ 30 nm. No contamination were detected from the electron probe microanalysis and the thermal gas-desorption measurement in vacuum.

The electrostatically excited flexural vibration at about 300 Hz was used for the strain range below 10^{-4}. The electromagnetically excited vibration of the "U"-shape composite reed at about 100 Hz was used for the strain range between 10^{-4} and 5×10^{-3} [5]. The temperature dependence of f and Q^{-1} was measured by the electrostatic method with ε of 10^{-6}, where the low temperature irradiation was made to get an insight into the grain boundaries through a probable modification by irradiation. The 2MeV electron irradiation at temperature, T, below 15 K was carried out by using the 3MeV single-ended electrostatic accelerator of TIARA, JAERI. The 20MeV proton irradiation at $T < 5$ K was carried out by using the tandem accelerator of University of Tsukuba.

3. Results and Discussion

Figure 1 shows an example of the SAMD observed for the n-Au specimens in the as-prepared state at various temperatures. The outline of the SAMD is as follows : For $\varepsilon < 10^{-4}$, f observed at 90 K shows a monotonous decrease by about 1 % with increasing ε, and f at 303 K shows a decrease for ε below 4×10^{-5} and then saturation for ε above 4×10^{-5} (Fig. 1(a)). Q^{-1} shows a monotonous increase with increasing ε for all the temperatures (Fig. 1(b)). The SAMD of f and Q^{-1} observed at 258 K is intermediate between those at 90 and 303 K. In Fig. 1(c) for $\varepsilon > 10^{-4}$, f at 293 K remains almost constant for $\varepsilon < 3 \times 10^{-4}$, and then increases by about 1 % showing saturation with increasing ε to 8×10^{-4}. On the other hand, f at 90 K remains almost constant for the present strain range. The SAMD of f observed at 223 K is intermediate between those found at 90 K and 293 K. For the strain range shown in Fig. 1(d), Q^{-1} shows a monotonous increase as like as Q^{-1} shown in Fig. 1(b).

The SAMD of f seen in Fig. 1 is so different from that of conventional poly-Au specimens. No plastic deformations are detected for the n-Au specimens after the SAMD measurements for ε up to 2×10^{-3} at 300 K, although the microyielding takes place for ε below 10^{-5} for conventional polycrystalline Au specimens [6]. After the low-temperature irradiation, the Q^{-1} spectrum was remained unchanged, in contrast, f showed a large monotonous increase which showed a recovery by warm-up after the irradiation [7]. These changes in f by irradiation and warm-up suggest the accumulation of irradiation-induced defects and the annealing out, respectively. From the combination of the observed results for the SAMD in f and the low temperature irradiation experiments, we surmise that the characteristic SAMD of f found for the n-Au specimens is associated with a certain anelastic process other than dislocation motions, where the GB regions may play some role [8]. It is noted that the SAMD of f reported for amorphous alloys is qualitatively similar to that observed for the n-Au specimens shown in Fig. 1, and is explained by the cooperative motion of many atoms [5]. For the atomic diffusion in the GB regions, the cooperative motion of three or four atoms are suggested after the computer simulations [9,10], indicating that one part of the GB regions may be soft mechanically. Possible explanation for the characteristic SAMD of f found for the n-Au specimens is a cooperative motion of a crystallite which is surrounded by the GB regions being mechanically soft in a relative sense. However, quantitatively, the SAMD of f for the n-Au specimens is much smaller than that found in amorphous alloy, suggesting that the fractional volume of such soft GB regions should be very low.

Figure 2 shows a relative change in the Young's modulus as a function of f, where f was adjusted by changing the reed length and the Young's modulus found at the lowest f is taken as the reference. Whereas the experimental accuracy is not enough, the general tendency of increase in the Young's modulus can be seen at 293 K, and the Young's modulus remains almost constant at 100 K. It is suggested that the anelastic strain at 293 K is as large as the dynamic modulus change detected by increasing f for the present frequency range, and the anelastic strain is much smaller at 100 K than at 293 K. On the other hand, a large decrease in the dynamic modulus is reported for the amorphous alloys [5] and it is attributed to the excitation of the cooperative motion of many atoms in resonance. As already mentioned, the behavior of the cooperative motion in n-Au metals may be quantitatively

different from that in the amorphous alloys.   As well as the similar measurements for high-density n-Cu, the further study is now in progress.

References

[1] P. G. Sanders, J. A. Eastman and J. R. Weertman, Acta Mater., 45(1997)4019.

[2] X. Y. Qin, X. R. Zhang, G. S. Cheng and L. D. Zhang, Nanostruct. Mater., 4(1998)661.

[3] S. Sakai, H. Tanimoto and H. Mizubayashi, Acta Mater. 47(1999)211.

[4] S.Sakai, H.Tanimoto, K.Otsuka, T.Yamada, Y.Koda, E.Kita and H.Mizubayashi, Scripta Mater., 45(2001)1313.

[5] H. Mizubayashi, T. Okamoto, K. Koyama and M. Horiuchi, Acta Mater., 46(1998)1257.

[6] G. Fantozzi, C. Esnoug, W. Benoit and C. Bonjour, Proc. 4th Inter. Conf. on the Strength of Metals and Alloys, (Nancy, France, 1976), p.351.

[7] H. Tanimoto, H. Mizubayashi, H. Fujita and S. Okuda, J. de Phys., 6(1996)C8-199.

[8] H. Tanimoto, S. Sakai and H. Mizubayashi, Mater. Trans., 44(2003)94 : Mat. Sci. Eng. A, in press.

[9] M.R. Sørensen, Y. Mishin and A.F. Voter, Phys. Rev. B, 62(2000)3658.

[10] P. Keblinski, D. Wolf, S. R. Phillpot and H. Gleiter, Phil. Mag. A, 79(1999)2735.
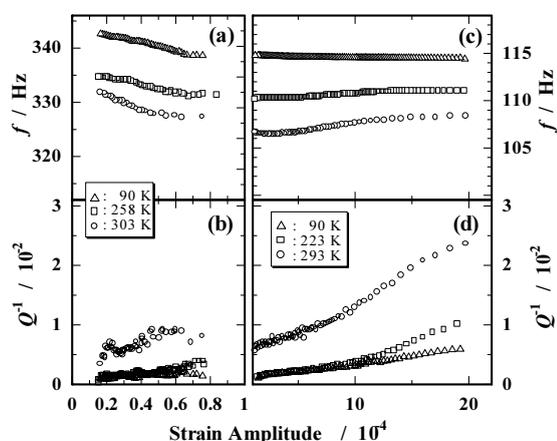
Figure 1.   Strain amplitude dependence of the resonant frequency, f, and the internal friction, Q^{-1}, observed for the n-Au specimens, where (a) and (b) are measured by the electrostatic method, and (c) and (d) by the electromagentic
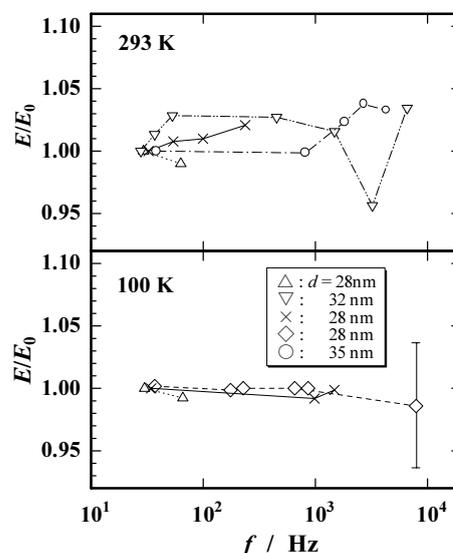
Figure 2.   Dynamic Young's modulus, E, as a function of the measurement frequency observed for n-Au with $\varepsilon = \sim 10^{-6}$ at (a) 100 K and (b) 293 K, where E_0 is E observed at the lowest frequency. d is the mean grain size estimated from the X-ray diffraction.

3.7   Cluster impact secondary electron emission from metal surface

T. Suzuki, S.Shimakura, T.Miyazaki, I.Arai and S.M. Lee

We measured the cluster impact secondary electron emission from Cu surface. The experimental setup has a configuration similar to the so-called a Daly-type particle detector in principle [1]. The Cu metal target is set on the dynode. We have simulated the ion trajectories by using the ion traffic simulator SIMION [2] in order to determine the optimum setup configuration possible to catch up all the electrons emitted from the Cu target. We used the emission statistics method developed by Dietz and Sheffield [3]. With this method, we can evaluate the number distribution of emitted electron. The clusters with an energy of 2 keV are size-selected under a mass resolution of about 500 and accelerated by a dynode bias voltage of 30 kV. They impact the Cu target at an angle of about 45 degrees. The electrons emitted from the surface of Cu target are accelerated by the same bias voltage and led onto the solid state detector(SSD).

When n electrons, each of which has an energy of E_0, are led onto the SSD simultaneously, the resulting signal obtained from the SSD should be proportional to their total energy $E = nE_0$. The spectrum obtained is affected by backscattered electrons [4] at SSD, besides the electrons from Cu target. The energy response function of SSD $F_n(E)$ is expressed by a sum of $n+1$ Gaussian functions, each of which corresponds to the number of backscattered electrons from 0 to n. Then we have tried a multi-Gaussian fitting to the obtained spectrum with use of the profile function $S(E)$ given by

$$S(E) = \sum_{n=1}^{N} Y_n F_n(E), \tag{1}$$

where Y_n is given by the intensity of n'th peak. A set of Y_n ($n = 1, 2, 3, .., N$) forms the number distribution of emitted electrons.

Next, we have tried a Polya distribution fitting of the number distribution Y_n. Polya distribution is

$$P(n, \mu, b) = \frac{\mu^n}{n!} (1 + b\mu)^{-n-1/b} \prod_{i=1}^{n} (1 + (i-1)b), \tag{2}$$

where μ is equal to the average emitted electron yield γ, n the number of emitted electrons and b the variance parameter with $0 \leq b \leq 1$. When $b = 0$, the Polya distribution becomes the Poisson distribution.

Figure 1 shows a correlation between the velocity of cluster and the reduced electron emission yield, i.e., γ per atom. Although the electron emission yield γ consists of two contribution i.e., the potential emission term [5] and the kinetic emission term, kinetic emission is dominative in this energy region [6]. And there is a sum rule about emitted electron yields in kinetic emission [4, 7]. It seems that the sum rule for the emitted electrons is not valid in the present case,i.e.., the case of Cu_n^+ ($n = 1, 2, .., 40$) cluster ions. However it might be valid for the cluster ions Cu_n^+ with $n \geq 9$. Furthermore, there might be another sum rule for the cluster ions Cu_n^+ with $n < 9$. Figure 2 shows a correlation between the reduced olectron emission yield $\gamma/Atom$ and the Polya parameter b [8]. Apparently, there are two tendencies for the parameter b as a function of $\gamma/Atom$ on reaching and leaving the cluster size 9, which give a minimum value of b.

As a further extention, we measured the cluster impact secondary electron emission by the cluster ions Cu_n^+ ($n = 1, 2, 3, 5, 7$) with the various injection energy 15, 20, 25 and 30kV. We changed the dynode

bias voltage to obtain the required injection energies. The optimum setup configuration to catch up all the secondary electrons was determined by a SIMION simulation for such energy change. We show the result of measutrement in Figure 3 and 4. In Figure 3, it seems that the sum rule for the emitted electrons is valid. There is no remarkable energy dependence. In Figure 4, the parameter b shows an increasing trend with an increase of $\gamma/Atom$.
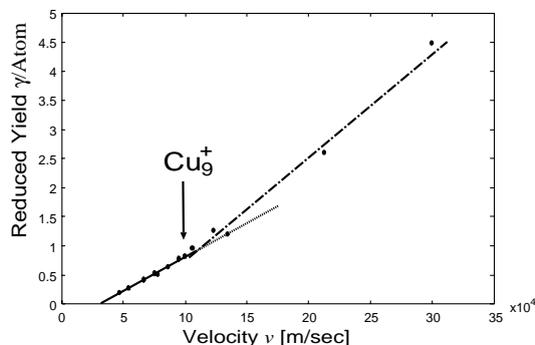
Fig. 1. Correlation between the reduced emitted electrons yield $\gamma/Atom$ and the velocity of cluster ion; the solid line is a result of least square fitting.
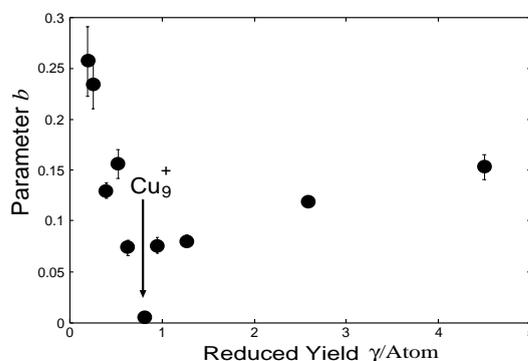
Fig. 2. Correlation between the reduced emitted electrons yield $\gamma/Atom$ and the Polya parameter b.
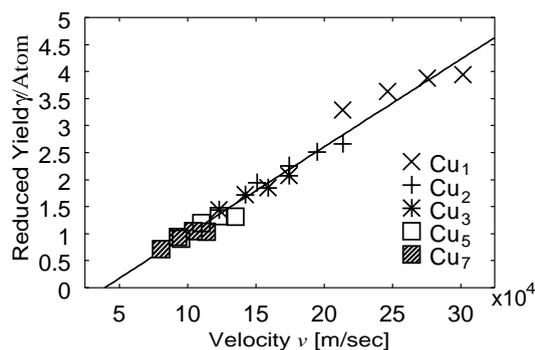
Fig. 3. The same as Fig.1. The solid line is a result of least square fitting. Each symbol means a cluster size.
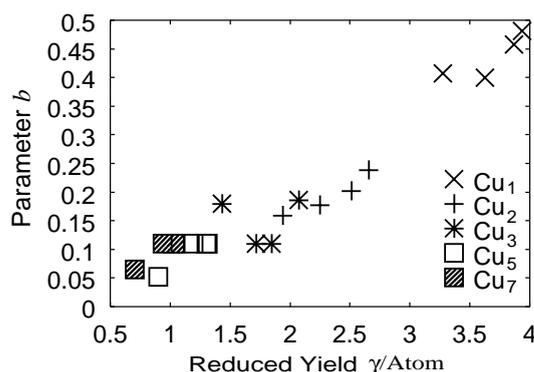
Fig. 4. The same as Fig.2. Each symbol means a cluster size.

References

[1] N.R.Daly, Rev. Sci. Instr., **31**, (1960)264.

[2] SIMION3D, Idaho National Engineering Laboratory Chemical Materials & Processes Department Lockheed Idaho Technologies Company.

[3] L.A.Dietz and L.C.Sheffield, Rev. Sci. Instr., **44**, (1973)183.

[4] G.Lakits, F.Aumayr and H.Winter, Rev. Sci. Instr., **60**, (1989)3151.

[5] L.M.Kishinevskii, Rad. Effects, **19**, (1973)23.

[6] F.Thum, W.O.Hofer, Suf. Sci., **90**, (1979)331.

[7] Hasselkanp et.al., Particles Induced Electron Emission Ⅱ, Springer-Verlag, Berlin(1992).

[8] A.Itoh et al., Nucl. Instr. Meth. in Phys. Res., **B193**, (2002)626.

3.8 TOF mass spectrometer for the experiment with highly-charged ion beam

Y. Takanashi, H. Sasaki and M. Imanaka, H. Arai, I. Arai and S.M. Lee

We have developed a TOF mass spectrometer system to measure the mass to charge ratio of the products generated by collision between a highly charged ion (HCI) and a neutral molecule or cluster. In this report, we introduce this system and preliminary spectra of collision products observed with fullerene C_{60} target irradiated by laser and HCI.

A schematic view of the system is illustrated in Fig.1. The HCI beam is provided from an electron cyclotron resonance ion source[1] and separated according to mass to charge ratio by the 90 degree analyzer magnet. We used a Xe^{20+} beam extracted by a voltage of 15 kV the current of which was 1 mA. The charge selected beam is chopped into a pulsed beam with a time duration of 200 ns long by a pulsing electric field generated by the deflecting electrode. To make a pulsed high voltage swing from 0 V to 2.8 kV on the electrode, we use a high speed push-pull switch (Bhelke Electronic, HTS31-GSM). The pulsed ion beam passes through the diaphragm of 1 mm in diameter and intersects the target chamber. The base pressure of target chamber is 10^{-8} torr. In the experiment, we fill the target chamber with the fullerene vapor at a typical pressure of 7.0×10^{-8} torr by heating fullerene powder up to 673K. The extraction region consists of the ionization region and the acceleration region. After a HCI beam has passed the ionization region, the extraction field can be pulsed with a high speed push-pull switch and the ions of collision products enter the acceleration region. In the acceleration region, there are applied two electric fields with different gradients from each other. The two stage extraction can focus the flight time of the ion which was produced with the same m/q but at a different position in the ionization region. An acceleration voltage of 2700 V is applied in a region of 5 cm in length giving a field gradient of 107 V/cm for the first acceleration region, while the same voltage is applied in a region of 4 cm giving a field gradient of 525 V/cm for the second acceleration. The intermediate electrodes (1 cm apart from each other) in the acceleration region ensure a good homogeneity of electric field necessary for a high mass resolution. The path of the ions is corrected by the electrostatic steerer and focused by the Einzel lens. The ions fly in a field free region of 2 m and finally go into the detector. We used a micro channel plate detector with a cup-type electron conversion dynode. We measured TOF spectra by using a trigger signal of the extraction pulse switch as a start signal and an output signal of the detector as a stop signal, both of which were lead to a 2 GHz multi-stop time to digital converter (P7886E, FAST ComTec).

Fig.2 shows the result obtained in collision with highly charged Xe^{20+} ions. There are the clearly identified peaks of the fullerene ions C_{60}^+, C_{60}^{2+}, ... , C_{60}^{6+} in addition to those of the residual gas ions. The mass resolution estimated from the peak of C_{60}^+ is about 200. Espetially, the ion C_{60}^{q+} with q upto 6 is observed dominantly while its fragment such as C_{58}^{q+} amounts to little there. This result is very much different from the case of C_{60} bombarded with a much more highly charged ion such as Au^{69+}[2]. In the present case, it seems that C_{60} has been ionized gently without receiving so much internal energy on its way crossing Xe^{20+}. The situation is similar to the collisional ionization of sodium clusters with use of highly charged ions[3], the collisional ionization of C_{60} with use of highly charged high-energy Xe ions[4] or the femtosecond laser driven ionization[5][6].

Now, we are planning to measure abundance spectra of cluster ions from the metal surface bombarded with slow highly charged ions, and to discuss in details about the mechanism of cluster formation dominated there in comparison with the one in neutral Xe atom bombardment[7][8].
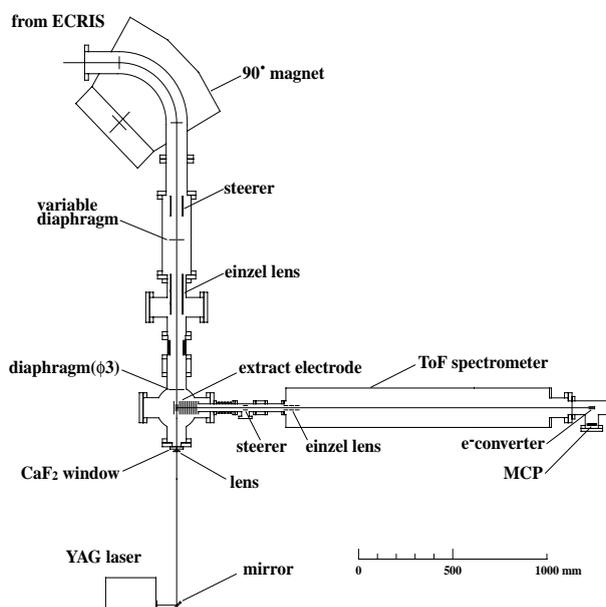
Fig. 1. Top view of beam line and TOF system.
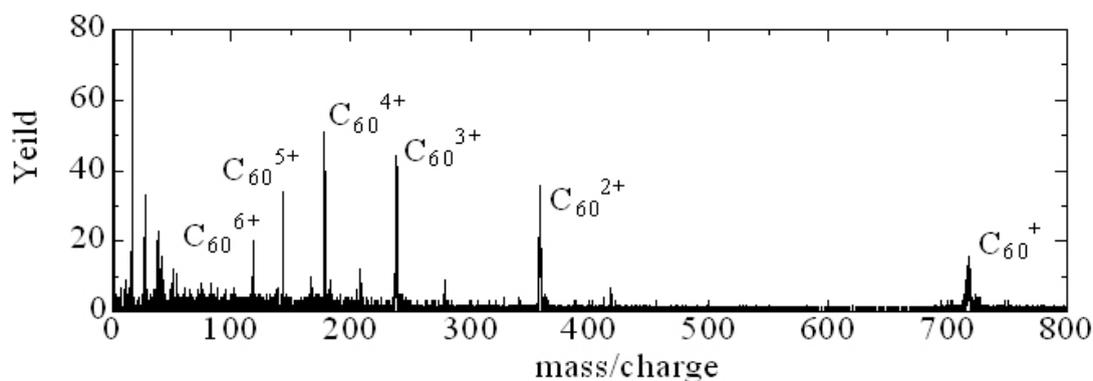
Fig. 2. Mass/Charge distribution of collision products observed with C_{60} target irradiated by Xe^{20+}.

References

[1] T. Kurita, Doctor thesis, University of Tsukuba(2001).

[2] T. Schenkel, et al, Eur. Phys. J., **D1**, 297 (1998).

[3] F. Chandezon et al., Phys. Rev. Lett., bf 87, 153402-1-4(2001).

[4] S. Cheng, et al, Phys. Rev., bf A54, 3182 (1996).

[5] E.E.B. Campbell et al., Eur. Phys. J., bf D16, 345(2001).

[6] P.G. Reinhard and E. Suraud, Int. J. Mol. Sci.,bf 1, 92(200).

[7] T. Sekioka, et al, Nuc. Inst. Meth. Phys. Res. bf B182, 121(2001)

[8] T. Schenkel et al., Prog. Sur. Sci., bf 61, 23(1999).

3.9 Cluster abundance spectra of In, Ga, Bi and Sn cluster produced by sputtering with Xe atoms

S.Hamajima, K.Teranishi, I.Arai, and S.M.Lee

We have produced 3-d transition metal cluster by bombardment of 6keV Xe atoms in a previous experiment, and observed its abundance spectra. The abundance spectra of clusters obtained were well expressed by a power function. We successfully apply the scaling hypothesis with a critical exponent –2.0 to such observed power function. To understand deeply, we carried out calculations based on percolation theory [1][2]. Suppose that the metal surface consists of mutually bond connected atoms and formation of a cluster takes place when all the bonds surrounding it are broken, the resulting cluster abundance spectra was represented well by employing a suitable value of the only parameter P, i.e., the broken bond probability. Furthermore, we have observed strongly correlation between P and melting temperature of metal. To explain the correlation, let us suppose the thermal diffusion model. In this model we assume the sputtering process like this. When the atoms bombard the target metal, thermal diffusion happens along the surface. The associated formation of thermally isolated small area, the equilibrium temperature being kept much higher than the melting temperature at around the bombardment position, and cluster formation within the thermally isolated area as a result of bond breaking.

In the present experiment we have investigated cluster abundance spectra for low melting temperature metals, In, Ga, Sn, and Bi,. The experiments were performed with a FAB ion source in conjunction with high resolution double focusing mass analyzer (JEOL JMS-HX110). Cluster cations sputtered from the surface of target materials under bombardment with 6keV Xe neutral atoms.

The spectra obtained show a quite different nature compared with the previously observed spectra for the 3d transition metals. As a result, we have identified two new types of spectra. One is a combination of an exponential function and a power function in the case of In and Ga and the other a combination of an exponential function and a log-normal function in the case of Sn and Bi. The exponential function-like behavior suggests the occurrence of an explosive release of monomer atoms just after the bombardment followed by a cluster formation via monomer absorption. A power function-like behavior may be interpreted as a cluster formation via bond-breaking on the remnant surface, while the log-normal function-like behavior is rather common to a cluster formation via cluster coalescense under the course of aggregation process in high density gaseous environment, which is unlikely to occur in the present case, i.e., a singly driven short time phenomenon. However, if it is the case an occurrence of an explosive release of monomer atoms with highly density core is strongly suggested.

In order to confirm this interpretation further, we have observed the change of abundance spectrum for In under changing the target temperature and the projectile energy. Figure 1 shows the abundance spectra measured for various target temperature. In the figure, the dependence on the target temperature is not observed at all. This effect is interpreted in the following way. At first, as for the explosive release of monomer atoms, the energies of participant atoms are too high to be affected by tiny thermal energies obtained at the initial target temperature. Secondly, as for the cluster formation via bond-breaking, the

remnant surface after explosion should be kept at low temperature because of the small remnant energy so that the broken bond probability P is kept at around the critical value. Figure 2 shows the abundance spectra measured under changing the projectile energy. As shown in the figure, it is found the fraction of larger clusters tends to decrease with decreasing the projectile energy. Especially, the effect is more enhanced at lower projectile energies.

For further quantitative understanding, we have fitted the spectra by the following function; $I(n) = aexs(-\alpha n) + bn^{-\beta}$. As a result, it was found that the parameter α does not depend on the projectile energy. This means that the projectile energy does not affect the density monomer atoms participating the explosion at the first stage. As for the parameter β, it was found that β tends to decrease of the temperature of remnant surface. The ratio a/b, i.e., a ratio of the exponential function part to the power function part, shows a tendency of becoming larger when the projectile energy becomes larger. Such a tendency may be interpreted as an increase of explosive area due to larger energy deposit.
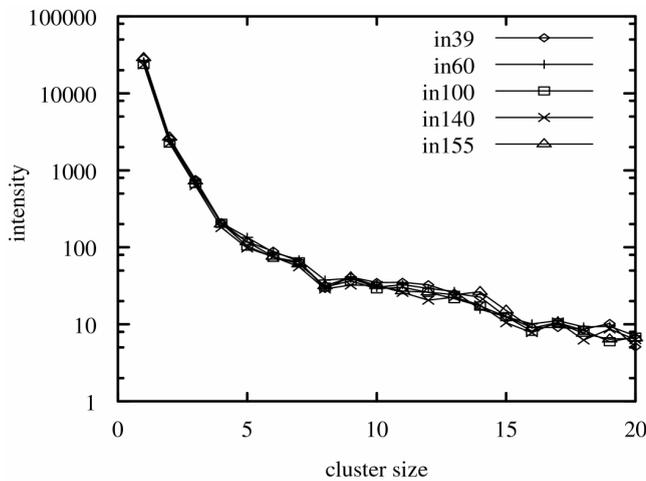

Fig.1 Abundance spectra for In measured under changing the target temperature from the room temperature to the nearly melting temperature. (155℃).
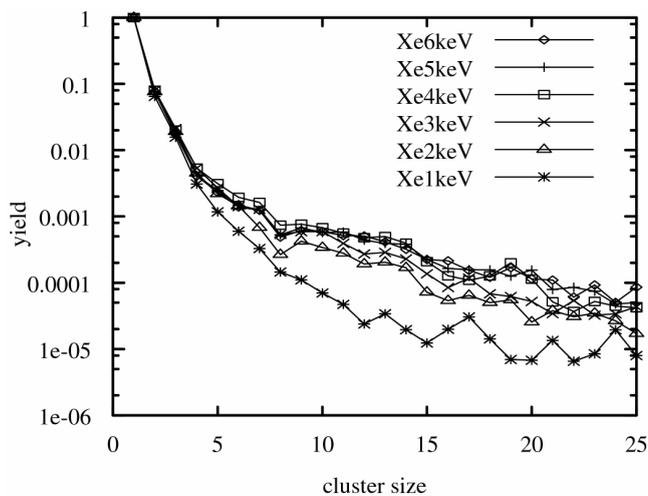

Fig.2 Abundance spectra for In measured under changing the projectile energy from 1keV to 6keV.

References

[1] M.B.Isichenko

Rev.Mod.Phys.,64(1992)961

[2] D.Stauffer, Introduction to Percolation Theory, Taylor and Francis, London,1994.

3.10 Plasma diagnostics of the plasma of liquid-He-free superconducting ECR ion source with use of a laser ablation method

H.Arai, M.Imanaka, M.Tsukada, T.Nakagawa[1], I.Arai and S.M.Lee

Short pulses of the neutral particles generated by laser ablation are injected into the plasma. The injected neutral metal atoms are ionized sequentially by the electron impact. Using the laser ablation method, we can measure the creation and subsequent decay of the individual charge state ions in plasma by observing their time dependent loss from ECRIS. Although these measurements are actually carried out in sequential step, they constitute the direct measurement of confinement and ionization time for highly charged ions in plasma of ECRIS. This tecgnique has been applied to the plasma diagnostics of several ECRISs with very promising insight into the plasma parameters. In the present study, the laser ablation of metal sample has been made.

The experimental setup for laser ablation method is shown in Fig.1. The laser beam is generated by an Nd:yttrium-aluminum-garnet (YAG) laser system with a wavelength of 1.06μm. The target sample of aluminum is placed on the biased electrode of SHIVA. The laser beam is focused by a lens of 3000mm focal length, and irradiate the aluminum target across the plasma.

The ejected pulsed neutral atoms were introduced into the ECR plasma and trapped in it.The neutral atoms were ionized by electron impact, and increased their charges step by step. The produced multiply charged ions were extracted by potential difference between the plasma electrode and the extraction electrode. These ions were separated and identified by the analyzing magnet. The beam intensity of each charge state heavy ions was measured by the Faraday cup, and we observed time structures of the beam intensity with use of digital storage oscilloscope.

To determine the plasma parameters as a function of B_{min}, we performed the measurements at B_{min} of 0.24T, 0.3T, 0.4T, and 0.45T, where B_{inj} and B_{ext} were fixed at 1.85T and 1.18T, respectively. Fig.2 shows a typical time structure of alminum ion current.

For analyzing the time structure of aluminum ion current, it is necessary to solve the rate equation[1] as follows:

$$\begin{cases} \dfrac{dn_0}{dt} = -n_e\chi^{ion}_{0\to1}n_0 + n_{gas}\xi^{ex}_{1\to0}n_1 - \dfrac{n_0}{\tau_0} \\ \vdots \\ \dfrac{dn_i}{dt} = +n_e\chi^{ion}_{i-1\to i}n_{i-1} - n_e\chi^{ion}_{i\to i+1}n_i - n_{gas}\xi^{ex}_{i\to i-1}n_i + n_{gas}\xi^{ex}_{i+1\to i}n_{i+1} - \dfrac{n_i}{\tau_i} \end{cases}$$

We carried out numerical calculations to solve the rate equation, taking the electron density n_e, the electron temperature T_e and the ion confinement time τ_c as free parameters. Fig.3 shows an example of calculated results for the time structure of aluminum ion current.

Fig 4. shows the resulting plasma parameters n_e, T_e and τ_c as a function of B_{min}. B_{inj} and B_{ext} were fixed to 1.85T and 1.18T. The electron density n_e gradually increases with increasing B_{min} up to 0.4T and then decreases at B_{min} greater than 0.4T. While the electron temperature T_e increases slowly with

---

[1]The Institute of Physical and Chemical Reserch (RIKEN)

increasing B_{min}, the ion confinement time τ_c decreases slowly with increasing B_{min}.

References

[1] Grigori D.Shirkov and Gönter Zschornack, *Electron Impact Ion Sources For Charged Heavy Ions,* page 134. Vieweg & Sohn Verlagsgesellschaft mbH,1996
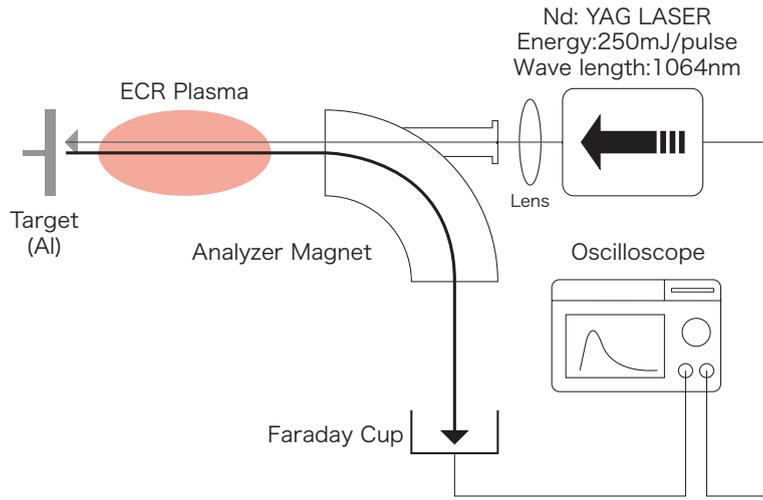
Fig. 1. Set up
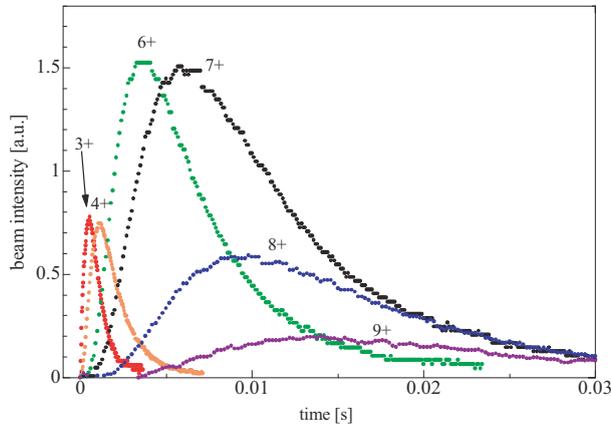
Fig. 2. Time structure of Al ion current

$n_e=2.23(\pm 0.06)e11[cm^{-3}]$
$T_e=582(\pm 46)[eV]$
$\tau_c=9.1(\pm 0.5)[ms]$
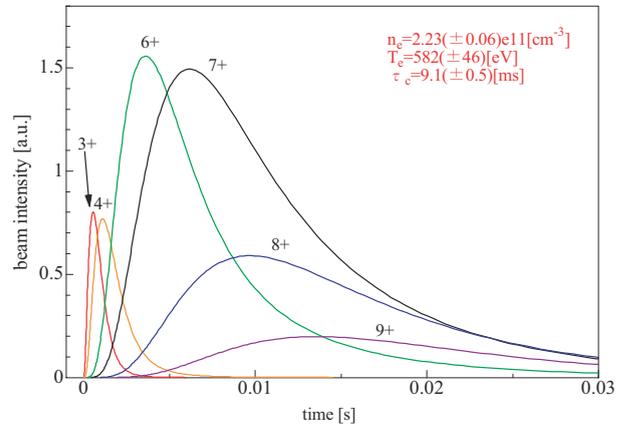
Fig. 3. Calculated results
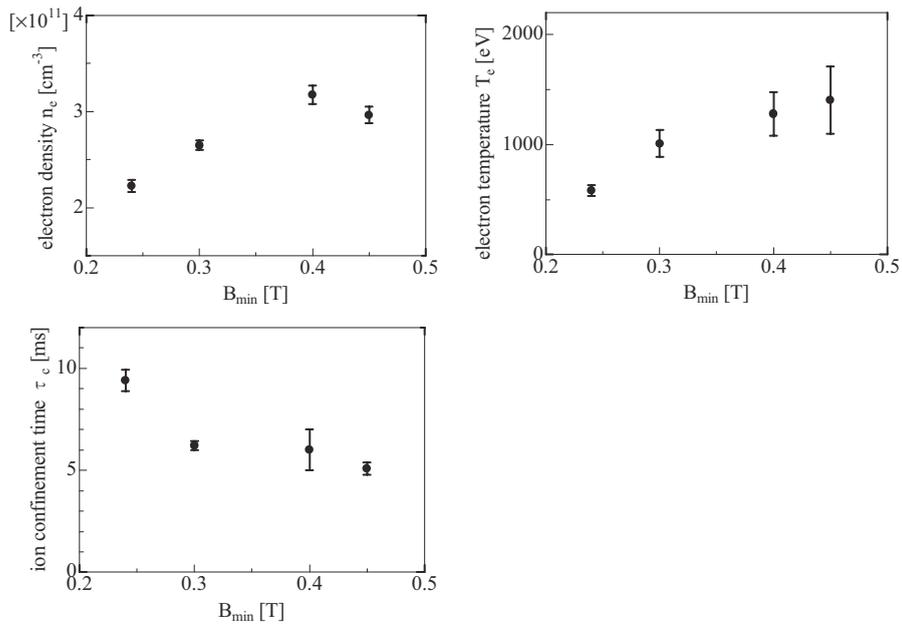
Fig. 4. Resulting of plasma parameter

3.11 The science of 3d transition-metal oxide system

M. Onoda, J. Hasegawa, K. Sekine, T. Ikeda, T. Ohki, T. Harigae, S. Miyasaka and T. Mutoh

We have explored structural and electronic properties of 3d transition-metal oxides and bronzes by means of x-ray four-circle diffraction and through measurements of magnetic resonance (NMR and EPR), magnetization, and electronic transport, in order to extract characteristic properties in the correlated electron system, electron-phonon-coupling system, quantum spin-fluctuation system, and novel materials. At the Tandem Accelerator Center, Varian continuous-wave and Bruker pulse NMR spectrometers have been used.

In 2002–2003, the following investigations were performed and a part of them have been published elsewhere [1–5]:

- Correlated-electron and electron-phonon-coupling systems

    - Metal-insulator transitions in V_6O_{13} and $Cu_xV_4O_{11}$

    - Metallic properties for $Sr_{1-x}M_xVO_3$ (M = Na, K, Tl and vacancy), SrV_2O_4 and $Sr_mV_nO_{m+n}$

- Quantum spin-fluctuation system

    - Geometrical frustrations in $Cd_xZn_{1-x}V_2O_4$ and $LiV_{2-x}M_xO_4$ (M = Al and Ga)

    - Spin-gap states in δ-$M_xV_2O_5$ (M = Ag, Tl, Na, K and Sr)

    - Superexchange interactions in MV_nO_{2n+1} (M = divalent ion; n = 1–5), $CdVO_3$, $Cd_{1-x}Ca_xV_3O_7$, SrV_5O_{11}, etc.

- Composite crystal system

    - Superspace group approach to $Cu_xV_4O_{11}$

- Secondary ion battery system

    - Li inserition effects in $M_{1+x}V_3O_8$ (M = Li, Na and Ag), $Ag_2V_4O_{11}$, $Cu_xV_4O_{11}$ and V_6O_{13}

This report describes briefly recent progress for the geometrically frustrated system, which has been selected for inclusion in IOP Select[1] [4].

Geometrically frustrated spinel system

The normal spinel-type $S = 1$ insulator MV_2O_4, where M is a nonmagnetic divalent ion surrounded tetrahedrally (the so-called A site) and the trivalent V has an octahedral coordination (the B site), exhibits the frustration effect, since the network of the V ions with antiferromagnetic interaction is achieved by the linkage of a regular tetrahedron block that has the V ion at each apex. The compounds with M = Cd, Mg and Zn exhibit the cubic−tetragonal transition due to a Jahn-Teller effect and a jump of magnetic susceptibility at T_{c1}. In addition, at the lower T_{c2}, the temperature dependence of susceptibility shows a kink without significant change of structure, suggesting the transition to the Néel state, in which spins are ordered antiferromagnetically in the chain of the tetragonal c-plane. Here, T_{c1} and T_{c2} are 97 and 35 K for M = Cd; 64.5 and 45 K for M = Mg; and 52 and 44 K for M = Zn. Using the high-temperature series expansion (HTSE) of up to the 8th-order, the Curie constant C and the nearest-neighbour exchange-coupling constant J for the cubic phase are estimated as follows: C = 0.98(2), 0.93(3) and 0.96(6) emu K (mol V)$^{-1}$, and J = 44(1), 92(7) and 92(7) K for M = Cd, Mg and Zn, respectively.

---

[1]http://Select.iop.org

A tetrahedral mean-field (TMF) model was presented previously on the basis of the exact solution of the magnetic susceptibility for a set of four interacting spins with J_{tet} for the spinel B sublattice or the pyrochlore lattice. In the MV$_2$O$_4$ system, this model was applicable at temperatures above $T \approx J_{\text{tet}}$, where J_{tet} apparently corresponds to $2J$. Recently, a modified theory, referred to as the generalized constant coupling (GCC) approximation, has been proposed. It gives essentially exact results for the susceptibility and specific heat of the classical Heisenberg antiferromagnet on the spinel B sublattice. Mechanisms for lifting the frustration through a coupling between spin and lattice of freedom were also investigated.

For the MV$_2$O$_4$ system, neither of the analyses for the crystal structure below T_{c1} and the magnetic susceptibility between T_{c1} and T_{c2} have been performed. In this work, the structures of CdV$_2$O$_4$ at 299 and 85 K (below T_{c1}) are determined by means of x-ray four-circle diffraction to understand the essence of structural and magnetic anomalies at T_{c1}. Using the exchange-coupling constant obtained in the previous work, magnetic susceptibilities above T_{c1} are examined with the GCC for spin-singlet V$_4$-tetramers that are not isolated but interactive to each other, *called pseudotetramers*. On the basis of the low-temperature structure, the tetragonally distorted pseudotetramer model is considered, and it is applied to the susceptibility data between T_{c1} and T_{c2}.

Figure 1(a) shows the crystal structure at 85 K projected on the tetragonal c-plane. Here, the VO$_6$ octahedron has four V−O bonds with 2.041 Å in the c-plane and two bonds with 2.014 Å along the c-axis. Therefore, the d$_{xy}$-character for the ground-state wavefunction is expected to be enhanced slightly, which may be attributed to the Jahn-Teller effect. The average V−O bond is 2.032 Å, which is equal to the value at 299 K within a standard deviation and is normal for V^{3+} ion. The network of V ions is expressed by the linkage of a distorted V$_4$ tetrahedron block consist of four V−V bonds with 3.066 Å and two bonds with 3.085 Å as shown in Fig. 1(b). The CdO$_4$ tetrahedron has equal Cd−O bonds with 2.145 Å in agreement with the values at 299 K and with those expected from the ionic radius of Cd^{2+} coordinated in a similar manner. The crystals used at 299 and 85 K have the occupancy probabilities 0.992(3) and 0.990(5) for Cd, respectively, indicating that both of them are nearly stoichiometric.

The magnetic susceptibilities χ of MV$_2$O$_4$ with M = Cd, Mg and Zn for the cubic phase consist of the d-spin term χ_{d} and the temperature-independent one χ_0 from the Van Vleck and diamagnetic components. Using C and J for the d-spin, and χ_0 determined with the HTSE, the reduced spin-susceptibilities defined as $\chi_{\text{d}}J/C$ are shown as a function of J/T in Fig. 2(a). The dotted curve and the dashed one indicate results of the HTSE ($\chi^{\text{HTSE}}J/C$) and TMF ($\chi_{\text{tet}}J/C$) with $J_{\text{tet}} = 2J$, respectively, calculated following their expressions given in [3]. According to the GCC without next nearest-neighbour interaction, the spin susceptibility is given by

$$\chi^{\text{GCC}} = \frac{C}{T}\frac{1+\epsilon}{1-\epsilon} \tag{1}$$

where $\epsilon = \chi_{\text{tet}}T/C - 1$. The full curve in Fig. 2(a) is drawn with $J_{\text{tet}} = J$ (not $2J$). This model accounts for the data in the cubic phase for CdV$_2$O$_4$ with $J < T_{\text{c1}}$ as well as those at temperatures above $T \simeq J$ for MgV$_2$O$_4$ and ZnV$_2$O$_4$ with $J > T_{\text{c1}}$, taking account of an error in C (2−6 %).

The detailed low-temperature behaviours of the reduced spin-susceptibilities as a function of T/J are plotted in Fig. 2(b). There exists a significant difference between the experimental and calculated results as shown by the dashed curve. This indicates that the exchange couplings for the V network change below
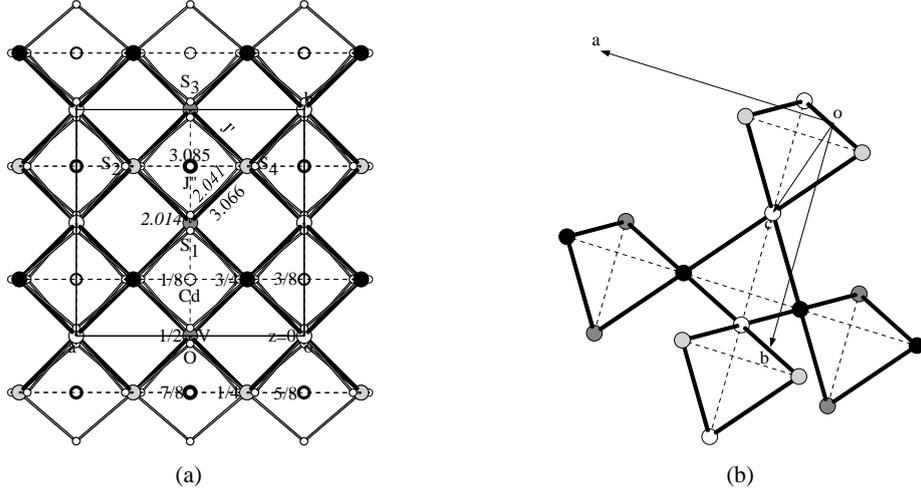
Fig. 1: The crystal structure of CdV_2O_4 at 85 K: (a) the projection on the tetragonal c-plane, where the numbers attached near the lines indicate V−V (roman) and V−O (italic) bond-lengths, respectively, and those near the circles show the z-coordinates; and (b) the network of V ions achieved by the linkage of a distorted tetrahedron block that has the V ion at each apex. The thick lines and the dashed lines denote the direct exchange couplings J' and J'', respectively.

T_{c1}, and the GCC for the *regular* pseudotetramers should be modified. To understand that difference, let us consider a cluster of four spins on the V_4 unit distorted tetragonally as drawn in Figs. 1(a) and 1(b). The Hamiltonian of this cluster is

$$H = J' \left(S_1 \cdot S_2 + S_2 \cdot S_3 + S_3 \cdot S_4 + S_4 \cdot S_1\right) + J'' \left(S_1 \cdot S_3 + S_2 \cdot S_4\right) \tag{2}$$

where J' and J'' are the exchange couplings for the thick lines and the dashed ones in Figs. 1(a) and 1(b), respectively, and S_i is the spin-1 operator. While the ground state for this Hamiltonian is a singlet for any antiferromagnetic J' and J'', the energy-level sequence depends on the ratio of J'/J''. The spin susceptibility for this distorted pseudotetramer is given by

$$\chi_{dt} = \frac{C}{8T} \frac{\sum_{S_t} G_{S_t} S_t (S_t + 1)(2S_t + 1) \exp\left(-E_{S_t}/T\right)}{\sum_{S_t} G_{S_t} (2S_t + 1) \exp\left(-E_{S_t}/T\right)} \tag{3}$$

where S_t is a value of the total spin of the cluster, and G_{S_t} and E_{S_t} are a degeneracy factor and the energy for S_t, respectively. The best fit to equation (1) with $\epsilon = \chi_{dt}T/C - 1$ provides $J' = 33.5(2)$ and $J'' = 55.4(1)$ K, when C and χ_0 are fixed at the HTSE values. An agreement between the experimental and calculated results is satisfactory as indicated by the full curve in Fig. 2(b). The values of $J' = 47.4(1)$ and $J'' = 29.3(3)$ K also give a close fit as drawn by the dotted curve, but this is not the case, since the direct exchange-couplings along the a and b directions are expected to be more effective due to an enhancement of the d_{xy}-character of the ground state. In other words, the V−V spacing dependence of exchange coupling below T_{c1} should differ from that above T_{c1}, where the ground-state wavefunction may not depend significantly on the species of M. The present result explains qualitatively the antiferromagnetic order in the chain of the tetragonal c-plane proposed for the isomorphous compound MgV_2O_4 and ZnV_2O_4. It is also suggested that the spin-orbit interaction and the Van Vleck component do not change significantly at temperatures of interest.

Between T_{c1} and J, the behaviours of the reduced spin-susceptibilities for MgV_2O_4 and ZnV_2O_4 that are independent of the applied field and the measurement time differ significantly from those calculated
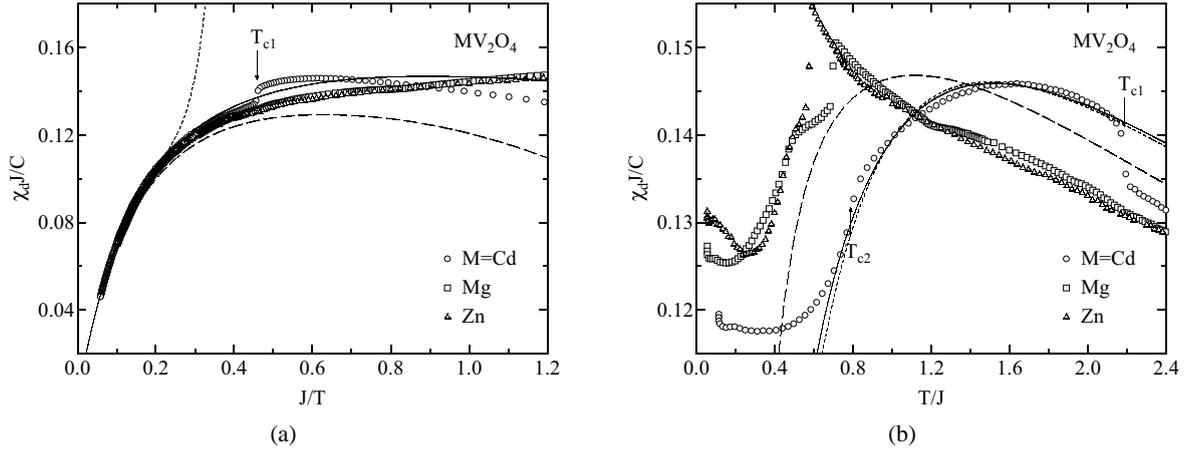
Fig. 2: (a) The reduced spin-susceptibilities $\chi_d J/C$ as a function of J/T for MV_2O_4 with M = Cd, Mg and Zn, where the full and dashed curves indicate fits to the GCC and TMF models, respectively; and the dotted curve denotes result calculated in terms of the HTSE. (b) The reduced spin-susceptibilities $\chi_d J/C$ as a function of T/J for MV_2O_4 with M = Cd, Mg and Zn, where the full (dotted) curve indicates a fit to the GCC for the tetragonally distorted pseudotetramers with exchange couplings $J' = 33.5$ (47.4) and $J'' = 55.4$ (29.3) K, and the dashed curve corresponds to the full curve in (a).

for the pseudotetramer with the GCC. It should be noted that $Zn_{0.5}Cd_{0.5}V_2O_4$ (one of the Zn−Cd solid-solution system), in which the $V^{3+}-V^{3+}$ interaction is modified randomly to give bond disorder, exhibits a transition to spin-glasslike phases at certain temperature T_g without structural change as in the case of the site-disordered system $Mg(V_{1-x}Al_x)_2O_4$. The temperature dependence of the susceptibility between T_{c1} and J is rather similar to that for $Zn_{0.5}Cd_{0.5}V_2O_4$ between T_g and J. Therefore, the deviation from the pseudotetramer model at temperatures below J is considered a common nature for the $S = 1$ spinel B sublattice which does not depend significantly on disordered effects.

Below T_{c1}, the frustration for interchains via J' or excited $d_{yz,zx}$ orbital exists, since preliminary measurements of x-ray diffraction below T_{c2} indicate the crystal symmetry to be tetragonal. As introduced before, the mechanisms of transition to the Néel state have been discussed theoretically.

In conclusion, the structure at 85 K is tetragonal and the d_{xy}-character of the ground state is enhanced due to the usual Jahn-Teller effect, leading to the anisotropy of the exchange-coupling constant J. The magnetic susceptibilities for the cubic phase with $J < T_{c1}$ are explained in terms of the GCC with regular pseudotetramers using the same J as determined by the HTSE. The maximum phenomena for the susceptibilities between T_{c1} and T_{c2} (near to J) are also understood by the GCC for the distorted pseudotetramers with two kinds of exchange coupling. While this phase does not have a spin order, it is accompanied with significant modulation of exchange interaction. For the isomorphous compound MgV_2O_4 and ZnV_2O_4 with $J > T_{c1}$, the GCC with regular pseudotetramers accounts for the susceptibility data at $T > J$. However, contrary to the behaviour expected from the GCC, the susceptibility for the cubic phase between J and T_{c1} increases rapidly with decreasing temperature, which does not depend significantly on the disordered effect. Our scenario for CdV_2O_4 presented here seems to be basically effective for the isomorphous compounds, but in order to understand quantitatively the susceptibility anomalies at T_{c1}, detailed theories for $T < J$ are necessary.

References

[1] M. Onoda and J. Hasegawa: J. Phys.: Condens. Matter **14** (2002) 5045-5059.

[2] N. Nishiguchi, M. Onoda and K. Kubo: J. Phys.: Condens. Matter **14** (2002) 5731-5746.

[3] N. Nishiguchi and M. Onoda: J. Phys.: Condens. Matter **14** (2002) L551-L557.

[4] M. Onoda and J. Hasegawa: J. Phys.: Condens. Matter **15** (2003) L95-L102.

[5] M. Onoda and I. Amemiya: J. Phys.: Condens. Matter in press.

3.12 3D nano-fabrication of rutile TiO$_2$ single crystals with swift heavy ion

K. Awazu[1], M. Fujimaki[1], N. Kobayashi[1], Yoshimichi Ohki[2], Satoshi Ishii, Kunihiro Shima

Recently, many researchers have studied photonic crystals using conventional semiconductor manufacturing. One of the most conventional methods to obtain micro-structures must be the reactive ion etching (RIE), however, roughness and ripple pattern on the side wall of micro-structures, RIE-lag, and etch stop have been frequently observed. We have examined the structure of latent track introduced in solids by the swift heavy ion.[1] In the present paper, we have developed a nano-micro structure fabrication method in rutile TiO$_2$ single crystal by use of swift heavy-ion irradiation. In the method, we have utilized a good etching selectivity induced by the ion irradiation. The area where ions heavier than Cl ion accelerated with MeV-order high energy were irradiated was well etched by hydrofluoric acid, by comparison etching was not observed in the pristine TiO$_2$ single crystal. Noticed that the irradiated area could be etched to a depth at which the electronic stopping power of the ion decayed to a value of 6.2keV/nm. In other words, etching was not observed in TiO$_2$ single crystal received the electronic stopping power below the threshold value of 6.2keV/nm. We also found that the value of the electronic stopping power was increased, eventually decreased against depth in TiO$_2$ single crystal with, e.g. 84.5MeV Ca ion. Using such a beam, inside of TiO$_2$ single crystal was selectively etched with hydrofluoric acid, while the top surface of TiO$_2$ single crystal subjected to irradiation was not etched. Fig.1 shows the cross section view of TiO$_2$ subjected to irradiation of 84.5MeV Ca ion followed by etching with hydrofluoric acid. At a glance, air gap was created in the region of 4-8micron from the top surface subjected to irradiation of 84.5MeV Ca ion at an accumulated dosage of 3×10^{14}cm^{-2} followed by etching. Roughness of the new surface created in the single crystal was within 7nm with the atomic forth microscopy measurement (Fig.2). The X-ray diffraction and high-resolution electron microscope analyses (see in Fig. 3) indicated that the irradiated area was composed from amorphous and the stressed rutile phases, both phases were well dissolved in 20% hydrofluoric acid. In conclusion, it was believed to enable to fabricate 3-dimensional nano-fabrication by use of this etching technique since the surface and aspect shape of rutile TiO$_2$ single crystals after etching was very flat in the order of nanometer. This methods also makes it possible to fabricate rutile TiO$_2$ plates thinner than a few micron with nano order flatness, which has been difficult by the conventional methods. Our method will be available for the processing of solar cells, photonic catalysts, or photonic crystals, which require nano-fabrication technique.

Reference

[1] K. Awazu, S. Ishii, K. Shima, S. Roorda, and J. L. Brebner, Phys. Rev. B **62**, 3689 (2000).

1. Photonic Research Institute, National Institute of Advanced Industrial Science and Technology,

2. Waseda University
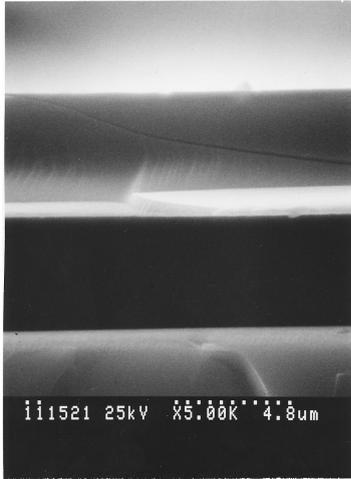
Fig.1 Cross section view of TiO_2 single crystal subjected to irradiation of 84.5MeV Ca followed by etching. Air gap was clearly observed.
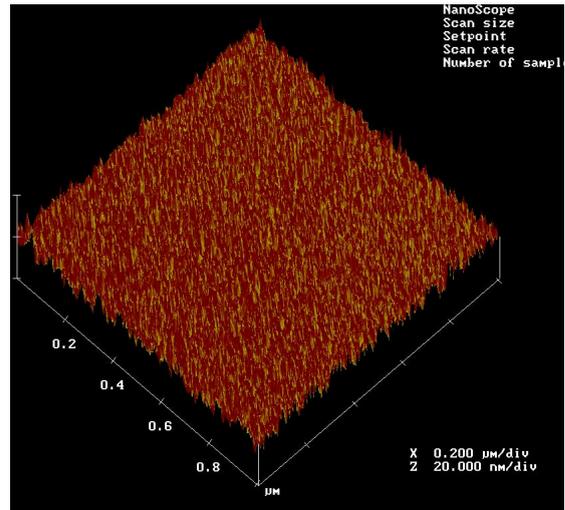

Fig.2 AFM view of the surface below the airgap shown in Fig.1. Roughness was estimated within 7nm.
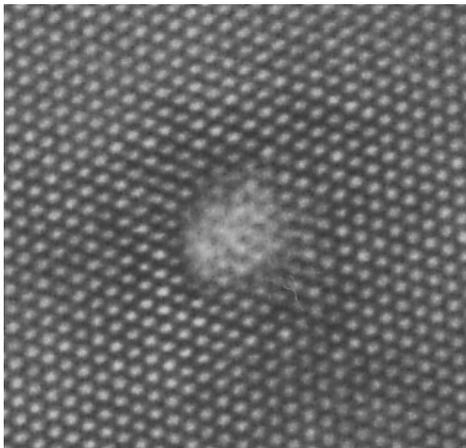

Fig.3 TEM observation of the TiO_2 single crystal irradiated with 84.5MeV Ca. Diameter of the latent track (milky color part) was estimated at 1.8nm.

3.13 Structual trasitions of Au_{55} isomers

M. Kubo, T.X.Li, I.Arai, S.M.Lee

The knowledge of structual and thermodynamic properties of finite atomic system is essential to the application of cluster-assembled materials. By using molecular dynamic simulation, we studied the solid-solid transitions of gold clusters.

Dynamic simulations on Au_{55} reveal the solid-solid structural transitions among different symmetric configulations, from cube-octahedron to icosahedron and disordered structure, at certain temperatures below the melting point. The latter deformation had not been demonstrated in earlier simulations on small clusters. However, Krakow and his colleagues found in their HRTEM(high resolution transmission electron microscope) study that supported gold clusters less than 10Å in size appear to be disordered[1]. The solid-solid transformations are microscopically demonstrated as processes of collective distortion of atoms and migration of partial atoms. In both cases the cohesive energies of the system go smoothly without any significant barrier during transitions.

Multiply twinned particles (MTP) are frequently observed under HRTEM for metal nanoparticles[2]. Our simulation on the thermodynamic properties shows this because of the thermal stimulation in a couple of sticked clusters.

The potential energy of clusters as a function of interatmic distance r_{ij} is modeled by

$$V = \frac{U_n}{2} \sum_{j=1}^{n} \left[A \sum_{i=1}^{n} e^{-p\left(\frac{r_{ij}}{r_{0n}}-1\right)} - \sqrt{\sum_{i(\neq j)=1}^{n} e^{-2q\left(\frac{r_{ij}}{r_{0n}}-1\right)}} \right]$$

In present work, the parametres for Au are set as $A = 0.118438$, $p = 10.15$ and $q = 4.13$,which have been fitted for bulk gold [3]. This potential leads the energy degeneracy of the lowest lying configulation of gold cluster. The structures of Au_{55} are acquired for the most stable configulations, using a genetic algorithm.

To understand the way in which three structual changes (I, II, and III) proceed inside the cluster, we record the atomic behaviour of the system in slow motion. We can see that the transition I from cube-octahedral isomer (CO) to icosahedral isomer (Ih) is a result of collective distortion: the thermal vibration of atoms abruptly causes unrecoverable distortion. The structual transition II happens among a set of metastable states with only a few atoms being rearranged. This process lasts for a relatively long time until the cluster reaches a new structure which, though still high in energy, is more susceptible to a further transition. The transition III is transient and exothermic like the first, but the structural transformation is mainly brought about by the thermal migration of an atom.

Closely related to the present study, one of the interesting studies on gold cluster is an absorption of foreign atoms on its surface possibly associated with its structural change. Actually, a molecular dynamics study for the absorption of silicon atoms on the surface of small gold cluster under the circumference of SiH_4 molecules is in progress.
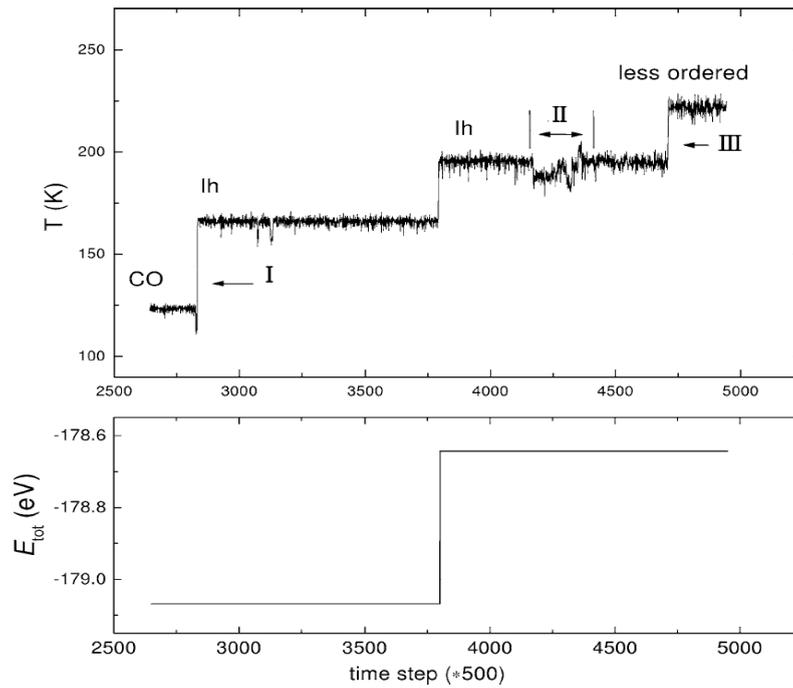
Fig. 1. Time histories of short-time-averaged temperature and total energy of the cluster. The labeled times and interval I, II, and III show the instabilities of the system corresponding to structural rearrangements in the cluster. The abrupt increment at the abscissa 3800 is the result of the artificial heating up by scaling.

References

[1] W.Krakow et al.,Phys. Rev. B49, 10591(1994).

[2] S.Iijima and T.Ichihashi,Phys. Rev/ Lett. 56,616(1986).

[3] F.Cleri and V.Rosato,Phys. Rev. Lett 56,616(1986).

4.1 Impurities in carbon foils produced by means of arc-discharge method

K. Shima, H. Koubai, K.Sasa and He Ming

The amount of impurities in carbon foils is known to depend on the method of fabrication. Since the carbon foils used as a target in our atomic collision experiment are mostly produced by arc-discharge method, the concentration of carbon foil impurities have been investigated by limiting the foils fabricated by arc-discharge method.   It is the characteristics of this work that the concentration of impurities has been investigated as thin as 1.2 $\mu g/cm^2$ of self-supporting carbon foils.

By using the arrangement shown in Fig.1, the impurities of elements Z<10 have been measured by using ERDA method with the incidence of 40 MeV $^{35}Cl^{7+}$, and those of elements Z>10 have been measured by PIXE method with the incidence of 4 MeV H^+. Two sets of self-supporting carbon foils have been prepared.; one is produced in our laboratory and the other is of commercial one, both of which are ranging from 1.2 to about 100 $\mu g/cm^2$ in thickness. In both sets, the carbon foils were detached from slide-glass, floated on distilled water, and were attached on a target holder with 5mm in diameter. Since the foils thinner than about 3 $\mu g/cm^2$ are likely to be broken when they are attached onto a target holder, the vapor of naphthalene was used as a supporting material which sublimates in one hour or so after being attached.

The results for the concentration of elements in commercial carbon foils are shown in Fig.2 in units of atoms/atoms as a function of carbon foil thickness.

Firstly, it is noted that the concentration of impurities is generally higher for thinner foils, and the concentration becomes almost constant at thicker region of foils. This fact indicates that the impurities are mostly attached on the surface of one side or on both sides of a foil.   As the result, the concentration of C of 1.2 $\mu g/cm^2$ is at most 60 % and that of 100 $\mu g/cm^2$ is 92% in units of atoms/cm^3.

Secondly, Fig.2 shows that the impurity of H is the highest in order of concentration, followed by O, Na and other elements such as Mg, Al, Si, S, Cl, K, Ca, Ti, Fe. It is to be noted that the hydrogen concentration has been observed to be higher than 20 % at 1 to 2 $\mu g/cm^2$ of self-supporting carbon foils.

Thirdly, it is confirmed that the above mentioned trend of impurity concentration versus elements or carbon thickness is more or less the same in both sets of commercial foils and home-made ones. In order to seek the origin of the mixture of impurities, the elemental analysis for a carbon rod to be arc-discharged and that of distilled water used in the preparation of self-supporting foil was performed by means of PIXE method. The result shows that purity of the materials themselves of carbon rod or water is so high. Other possibilities such as the mixture of impurities during the arc-discharge, floating on water followed by attaching on a target frame must be investigated.
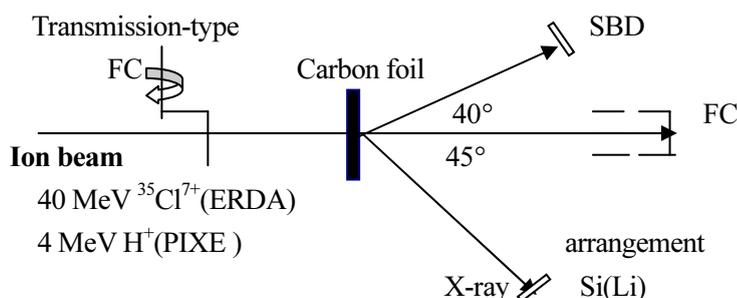

Fig.1. Experimental arrangement
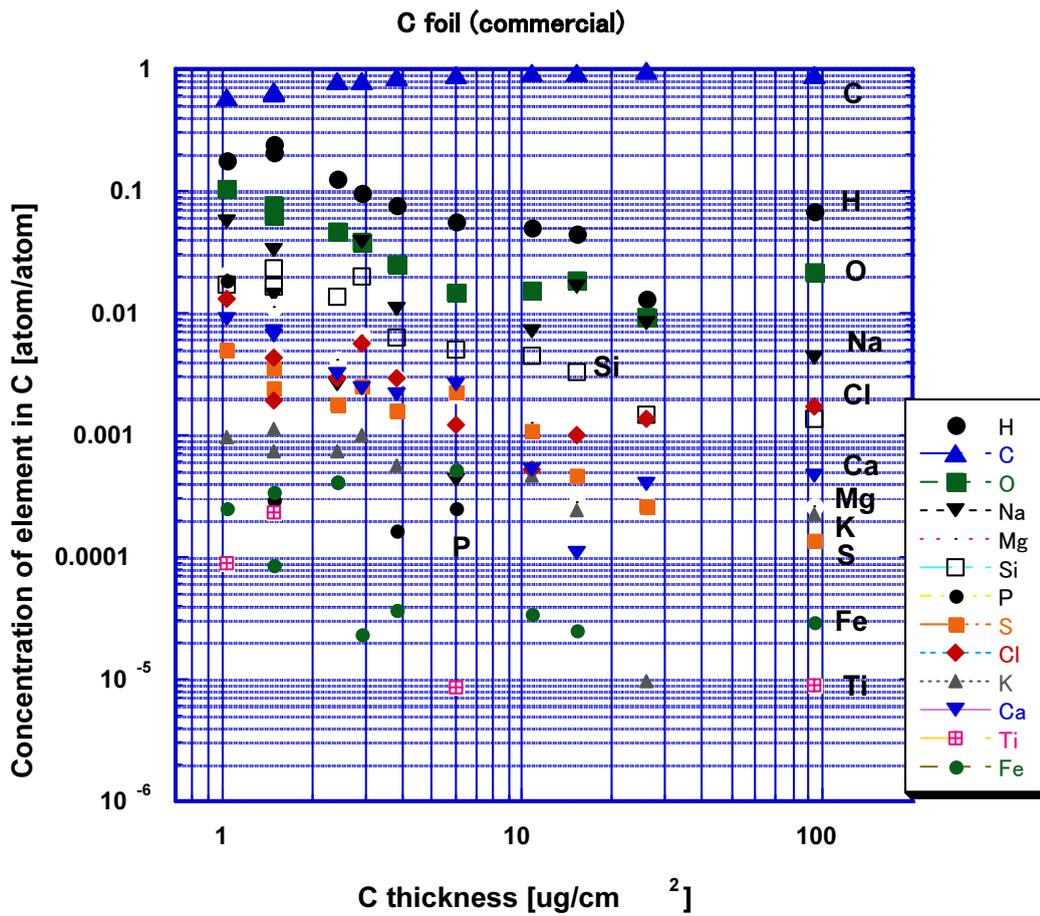
Fig.2. Ovserved concentration of elements in commercial carbon foils in units of atoms/atoms as a Function of carbon thickness.

4.2 Calibration of hydrogen concentration by alpha-gamma angular correlation method

K.Furuno, M.Ishizuka, H.Ohshima, Y.Yamato, K.Sasa and T.Komatsubara

In the hydrogen analysis with the resonant nuclear reaction $^1\text{H}(^{19}\text{F},\alpha\gamma)^{16}\text{O}$ (NRA), the distribution of hydrogen atoms can be derived from an experimental excitation function. The yield of 6~7-MeV γ rays observed at an incident ^{19}F energy E_0 is given by

$$Y(E_0) = \frac{\Omega}{4\pi}\varepsilon\eta Q_0 \int_0^{R_0-R_m} \int_{-\infty}^{\infty} n(x)f(E_0,E_R,E',x)dE'dx, \tag{1}$$

where Q_0 is the integrated charge of ^{19}F ion beam, ε stands for the intrinsic detection efficiency of a γ-ray detector, η denotes the branching ratio of α decays to excited states in ^{16}O. In eq.(1), the function $f(E_0,E_R,E',x)$ is described by

$$f(E_0,E_R,E',x) = \frac{1}{\sqrt{2\pi(\sigma_B^2+\Omega_S^2)}}\sum_i BW(E_R^i)\exp\left[-\frac{\{E_0-\Delta E_x-E'\}^2}{2(\sigma_B^2+\Omega_S^2)}\right]. \tag{2}$$

In this expression, ΔE_x is the energy loss of the incident ^{19}F from the sample surface to a depth x; σ_B is the energy spread of the incident ^{19}F beam; Ω_S means the energy broadening due to energy straggling of ^{19}F in the sample. The cross section of the nuclear reaction is written as $BW(E_R^i)$, which is well known Breit-Wigner formula. Since a few different resonances should be taken into account for thick samples, we write the Breit-Wigner formula of i-th resonance as

$$BW(E_R^i) = \sigma(E_R^i)\frac{E_R^i}{E'}\cdot\frac{\Gamma_{tot,i}^2}{4(E'-E_R^i)^2+\Gamma_{tot,i}^2}. \tag{3}$$

We can estimate σ_B and Ω_S in good approximation for about 10 % precision of measured hydrogen concentration. The cross sections $BW(E_R^i)$ and the branching ratios η are measured with a precision of 10 %. Using these values, we can calculate $f(E_0,E_R,E',x)$ numerically.

The quantity of $\Omega\varepsilon/4\pi$ can be determined from an $\alpha-\gamma$ angular correlation experiment at $E(^{19}\text{F}) = 16.44$ MeV with about $10\,\mu$m-thick hydrogen bearing sample[1]. If we measure the excitation function for the sample with the *same* experimental set up as the $\alpha-\gamma$ angular correlation, the hydrogen distribution $n(x)$ can be obtained from the analysis of the excitation function, since $\Omega\varepsilon/4\pi$ is already known. If once the distribution $n(x)$ is calibrated, we can use this sample as a standard to determine the detection efficiency of any γ-ray detector in other system for hydrogen analysis with NRA.

We prepared a $10\,\mu$m thick n-type silicon disk. It was mounted on a stainless frame with glue, and coated on one side with $400\mathring{A}$ thick gold by vacuum evaporation to make it electrically conductive between the silicon disk and the frame. We implanted negative hydrogen ions into this silicon sample at 100 keV. The area of implantation was defined with an aperture of 4 mm diameter and the beam was swept using a deflector to obtain uniform lateral distribution of implanted hydrogen. The total charge was $8000\,\mu$C, so that the areal density of hydrogen was

$$n_{\text{H}} = \frac{8000\times10^{-6}}{\pi\times(0.2)^2\times1.6021}\times10^{19} = 3.97\times10^{17} \qquad [\text{H/cm}^2]. \tag{4}$$

Since the integration of the negative beam current was not made in a Faraday cup with adequate suppression of secondary electrons, the uncertainty of the beam current integration is estimated to be 10 %.

The angular correlation experiment and the measurement of excitation function were performed using the following experimental set up. A cylindrical target chamber of 100 mm diameter was placed at the center of a goniometer for γ-ray angular-distribution measurements in nuclear physics. In this chamber, the silicon sample was set at the center. A silicon surface barrier detector (SSD) was placed behind of the silicon sample. A $6\,\mu$m thick aluminum foil was inserted between the silicon sample and SSD to stop incident ^{19}F ions and recoil ^{16}O. The distance between the silicon sample and SSD was 13 mm. An aperture of 6mm in diameter was mounted on SSD. From these geometrical arrangement, the emission of α particles was restricted in a cone with a half angle of 16° along the beam direction. Gamma rays were observed with a 76×76 mm BGO scintillation detector. The distance from the center to the front surface of the BGO detector was 61.5 mm.
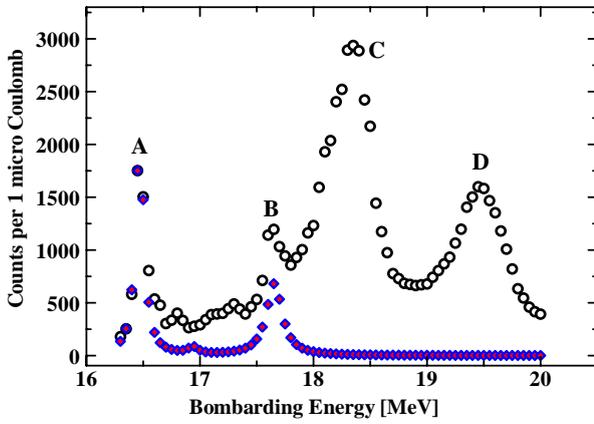
Figure 1: Excitation function(open circles) and calculation assuming a thin hydrogen layer at the sample surface(full diamonds)
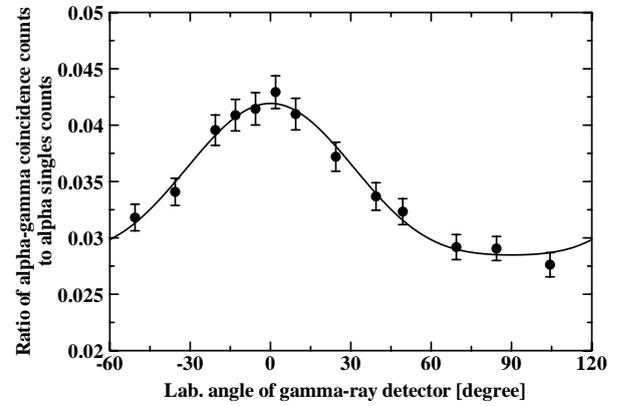
Figure 2: $\alpha - \gamma$ angular correlation

At first, we measured an excitation function to observe 16.44 MeV resonance by placing the γ-ray detector in the beam direction. In Fig. 1, the peak A and B are ascribed to yields from a thin layer of hydrogen adsorbed on the sample surface at energies 16.44 and 17.6 MeV. The peak C and D are ascribable to implanted hydrogen at 16.44 and 17.6 MeV, respectively. To subtract the yield from the surface hydrogen, we calculated γ-ray yields assuming a 50 nm thick hydrogen layer at the surface as indicated by full diamonds in Fig. 1. The concentration of the surface hydrogen was normalized to the experimental excitation function at 16.44 MeV.

In the second place, we performed an $\alpha - \gamma$ angular correlation experiment on the 16.44 MeV resonance. The energy of incident ^{19}F beam was fixed to 18.35 MeV (the peak C in Fig. 1). The experimental results are plotted in Fig. 2. The angular correlation obtained in the present experimental arrangement is in general expressed by Legendre polynomials[2], namely

$$R(\theta_\gamma) = a_0 + a_2 P_2(\cos \theta_\gamma) + a_4 P_4(\cos \theta_\gamma). \tag{5}$$

Its zero-th order term gives the detection efficiency of the γ-ray detector including the solid angle[1]. The solid line in Fig. 2 shows the result of this fit to Legendre polynominals. The statistical errors in γ-ray and

α-particle counts and systematic error due to mechanical movement of the goniometer were taken into account for experimental values. The coefficients in eq.(5) are

$$\frac{\Omega_\gamma}{4\pi}\varepsilon_\gamma = a_0 = (3.15 \pm 0.04) \times 10^{-2} \tag{6}$$

$$a_2 = (0.79 \pm 0.07) \times 10^{-2} \tag{7}$$

$$\text{and} \tag{8}$$

$$a_4 = (0.24 \pm 0.08) \times 10^{-2}. \tag{9}$$

The value of χ^2 was 3.72, so that the present fitting is reasonable for the degree of freedom 10.

The γ-ray singles angular distribution obtained at the same time as the angular correlation experiment was isotropic within 5 %. The excitation function obtained before the angular correlation experiment, therefore, can be used for the analysis of the hydrogen concentration $n(x)$.
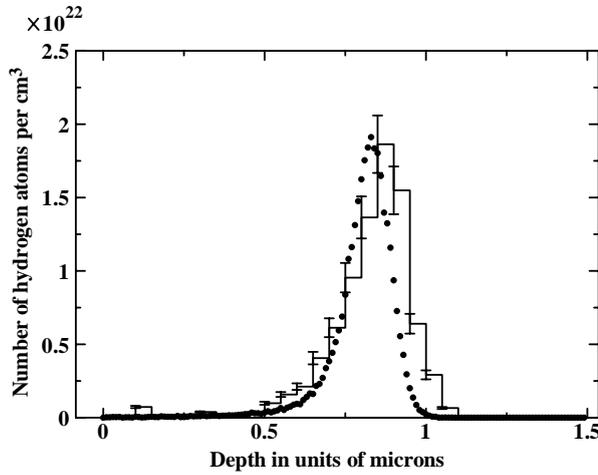
Figure 3: Exracted hydrogen distribution
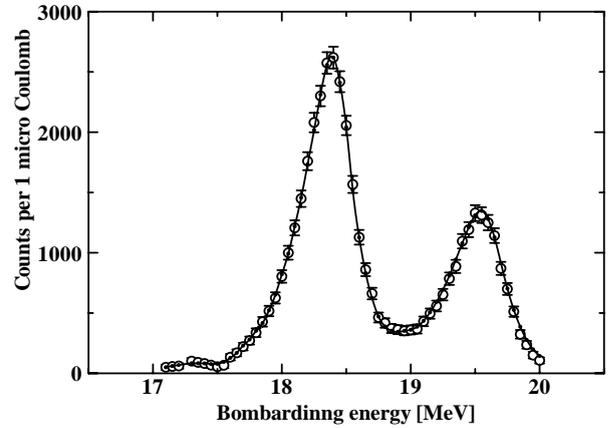
Figure 4: Open circles indicate excitation function corrected for interpolation, background subtraction and data smoothing. The solid line shows the excitation function calculated from the extracted hydrogen distribution.

The procedure of data analysis is as follows. We subtracted the yield due to the surface hydrogen from the experimental data indicated by open circles in Fig. 1. Then we subtracted 308 counts from the above excitation function. The counts is an average of counts between 16.5~17.5 MeV. We assumed that the 308 counts corresponded to the smooth non-resonant term in the cross section on the basis of the experimental data reported by Spyrou *et al.*[3]. Furthermore, we made data smoothing by 3 point moving average.

As regards the hydrogen distribution $n(x)$, we divided the silicon sample into 0.05 μm thick layers and assumed that the distribution is uniform within each 0.05 μm thick layer. Initial values of the distribution was derived by least squares method and negative solutions were put to null. The final derivation of $n(x)$ was performed according to the prescription by McGlone[4] and Smulders[5]. The weight in chi-square minimization was assumed to be a sum of errors in the data correction, background subtraction and data smoothing.

Fig. 3 shows the extracted hydrogen distribution $n(x)$, while Fig. 4 displays the calculated excitation function using the distribution. The value of χ^2 is 23.5, and this extraction seems to be reasonable for the

degree of freedom 28. A depth distribution of implanted negative hydrogen ions was calculated with the computer program SRIM[6]. The total number of implanted ions was assumed to be 1000. The results is shown by small full circles in Fig. 3. The ordinate of this simulation is normalized to the extracted hydrogen distribution. The depth distribution obtained from SRIM calculation is slightly shifted towards surface side in comparison with experimental data, but the shape is in good agreement.

If we sum up $n(x)$ in Fig. 3 from 0.5 to 1.1 μm assuming that these are implanted negative hydrogen ions, we obtain the following areal density:

$$n_{\mathrm{H}} = (4.48 \pm 0.47) \times 10^{17} \qquad [\mathrm{H/cm^2}]$$

The uncertainties was evaluated as the sum of relative uncertainty of 5.7 % in the extraction of $n(x)$, 8.3 % in the cross section on resonance $\sigma(E_{\mathrm{R}})$, 2.7 % in the beam current integration and 1.3 % in the detection efficiency. The overall relative uncertainty is 10.2 %.

As a calibration independent of NRA, the areal density of implanted hydrogen was measured by proton-proton elastic-recoil coincidence spectroscopy at a proton energy of 20 MeV. We employed a 7.5 μm thick Kapton($C_{22}H_{10}N_2O_4$) foil. The results are listed in Table1.

Table 1: Experimetal results of proton-proton elastic-recoil coincidence spectroscopy

samples	yield	relative integrated beam current
Silicon	$Y_S = 338 \pm 11$	$C_S = 1000$
Kapton	$Y_K = 2518 \pm 50$	$C_K = 200$

The areal density of the Kapton foil was estimated to be $\rho_K = 1.188 \pm 0.048\,[\mathrm{mg/cm^2}]$. This density corresponds to the hydrogen density of $\rho_K(\mathrm{H}) = 32.5 \pm 1.3\,[\mu\mathrm{g/cm^2}]$. Since proton-proton elastic-recoil coincidence spectroscopy does not discriminate the surface hydrogen, we estimated the relative ratio λ of the surface to the implanted hydrogen to be 0.21 ± 0.012 from the analysis of the excitation function. With the mass of a hydrogen atom $m_{\mathrm{H}} = 1.673 \times 10^{-18}\,[\mu\mathrm{g}]$, the areal density of the implanted hydrogen is given by

$$n_{\mathrm{H}} = \rho_K(\mathrm{H}) \cdot \frac{Y_S}{Y_K} \cdot \frac{C_K}{C_S} \cdot \frac{1}{1+\lambda} \cdot \frac{1}{1.673} \times 10^{18} \qquad [\mathrm{H/cm^2}]. \tag{10}$$

Substituting each value into this formula, we obtained the following value. $n_{\mathrm{H}} = (4.43 \pm 0.35) \times 10^{17}\,[\mathrm{H/cm^2}]$. The uncertainty includes the statistical errors of 3.3 % and 2 % in Y_S and Y_K, respectively, the uncertainty of 4 % in the estimate of $\rho_K(\mathrm{H})$ and uncertainty of 5.7 % in the estimate of λ. We ignored the uncertainty of current integrations, because 20 MeV protons pass through the silicon sample and the Kapton foil without appreciable energy loss and proton beam current was measured in a sufficiently deep Faraday cup with adequate electron suppression. An overall relative uncertainty was 7.9 %.

Table 2 summarizes the areal densities of the implanted hydrogen obtained from three independent methods. These areal densities are in good agreement within experimental uncertainties. An average weighted by uncertainties and an arithmetic average for these three areal densities are

$$n_{\mathrm{H}} = (4.29 \pm 0.23) \times 10^{17} \qquad \text{and} \qquad n_{\mathrm{H}} = (4.29 \pm 0.41) \times 10^{17} \qquad [\mathrm{H/cm^2}]. \tag{11}$$

Since the three areal densities are all evaluated in one measurement, their uncertainties would not be reasonable as weights. In fact, the uncertainty of weighted average seems to be too small. Thus we

Table 2: Areal densities of the implanted hydrogen obtained from three independent methods

Method	Areal density$\times 10^{17}$H/cm^2
Current integration of implanted negative hydrogen ions	3.97 ± 0.40
Excitation function for the resonant nuclear reaction	4.48 ± 0.47
Proton-proton elastic-recoil coincidence spectroscopy	4.43 ± 0.35

adopt the arithmetic average as the areal density of hydrogen in the silicon sample which can be used as a standard sample for the calibration of γ-ray detector in hydrogen analysis with NRA.

References

[1] K.Sasa, *et al.* Nucl.Instr.Meth.in Phys.Res., B190(2002)287-290.
and
K. Furuno, H. Ohshima, K. Sasa, Y. Sasaki, K. Yamada, S. Yokose, M. Ishizuka and T. Komatsubara, Annual Report of the Tandem Accelerator Center, University of Tsukuba, UTTAC-69, 2001, 96-99 (2001).

[2] A.E. Litherland and A.J. Ferguson, Canadian Journal of Physics, **39** (1961) 788-824.

[3] K. Spyrou, C. Chronidou, S. Harissopulos, S. Kossionides and T. Paradellis, Zeitschrift für Physik **A 357**(1997)283.

[4] V.A.McGlone and P.B.Johnson, Nucl.Instr.Meth.in Phys.Res., B61(1991)201-212.

[5] P.J.M. Smulders, Nuclear Instruments and Methods in Physics Research, **B14** (1986) 234-239.

[6] J.P. Biersack and J.F. Ziegler, Computer code SRIM.

4.3   The unfolding of hydrogen distribution in thick mineral samples from ERCS spectra

K.Furuno

In our previous papers, we have reported that proton-proton elastic-recoil coincidence spectroscopy is a powerful method for the hydrogen analysis of mineral samples with thicknesses up to 0.2 mm[1]. Hydrogen concentrations in melt inclusions, however, were evaluated qualitatively on the assumptions that (1) the hydrogen in the inclusions has uniform distribution; (2) the distribution is constrained in a limited region; (3) the yields depend on the depth x in accordance with an exponential function; and (4) the lateral size of the inclusion is larger than the beam size.

To remove the assumption (1) and to develop a method for extraction of hydrogen distribution, analyses were performed for the sum-energy spectrum observed with an artificial target which consisted of four 50 μm thick non-hydrated artificial-quartz disks alternated with five 2.5 μm thick Mylar foils. For
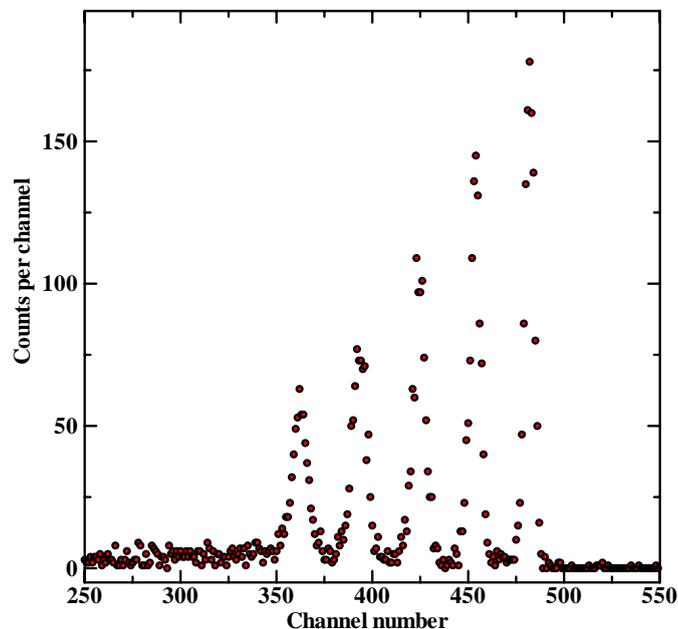
Figure 1: A sum energy spectrum obtained by projecting coincidence events along the line of $E_{left} + E_{right}$=const. in the two dimensional spectrum.

discussions below, a typical spectrum for the artificial target is displayed in Fig. 1 again. The rightmost peak is due to the scattering in the Mylar foil covering the beam exit side, while the leftmost peak is caused by the foil covering the beam entrance side.

The first remarkable feature of this spectrum is that the integrated counts of each peak change in good approximation in accordance with a simple exponential function of the type of

$$N(x) = N(0)\exp\{-\mu(d-x)\}. \tag{1}$$

The symbol μ stands for the attenuation coefficient. The second feature is that spaces between the five peaks are almost same. This implies that the sum energy is proportional to the depth. The third feature is

that the width of peaks becomes wide as the sum energy decreases. The exponential decrease of integrated counts is in agreement with the result reported by Cohen[2], and is ascribed to the decrease of the detection efficiency for scattered and recoil protons due to the multiple scattering in the target. Hofsäss *et al.* also discussed the decrease of coincidence counts on the basis of the multiple scattering[3]. The broadening of peaks is caused partly by the energy straggling and the intrinsic energy resolution of proton detectors, but more seriously by the surface roughness of the sample.

The linear relation between the sum energy and the depth was confirmed with a calculation using Computer code TRIM[4]. The energy broadening was estimated from the spectrum shown in Fig. 1. We may assume a rectangular hydrogen distribution along the depth in Mylar foils in good approximation. If we assume the energy broadening to be a Gaussian form, the resultant sum-energy spectrum is given by convolution of the Gaussian function and the rectangular distribution. The convolution leads to

$$Y_M(E)dE = \frac{d_M}{E_{M2} - E_{M1}} Q_0 \frac{n_M}{2} \left[\mathrm{Erf}\left(\frac{E_{M2} - E}{\sqrt{2}\,\sigma}\right) - \mathrm{Erf}\left(\frac{E_{M1} - E}{\sqrt{2}\,\sigma}\right) \right] dE, \qquad (2)$$

where Erf's stand for error functions, σ is the standard deviation of the energy broadening, d_M is the thickness of the Mylar foil, n_M is the number of hydrogen atoms per unit volume of the Mylar, E_{M2} and E_{M1} are the sum energies at edges of the Mylar and Q_0 is the product of integrated beam current I_0, the cross section $\sigma(\theta)$ of proton-proton scattering at $45°$ and the effective solid angle $d\Omega$ of detectors.

In Fig. 1, the number of channels from the leftmost(lowest) peak to the rightmost(highest) peak is 120, which corresponds to the sample thickness of 200 μm. With this relation, the number of channels corresponding to 2.5 μm thick Mylar foils becomes 1.5. The energies E_{M1} and E_{M2} in eq.(2) were assumed to be the peak channel minus 0.75 and plus 0.75 channel for each peak. Several calculations of $Y_M(E)$ in eq.(2) were repeated to fit the experimental spectrum by adjusting two parameters of σ and a group of all factors in front of square brackets. Two examples of this fit are shown in Figs. 2 and 3.
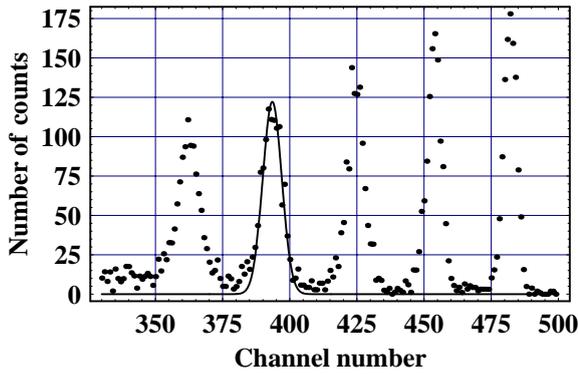
Figure 2: Fit of the second peak to the error function   Figure 3: Fit of the highest peak to the error function
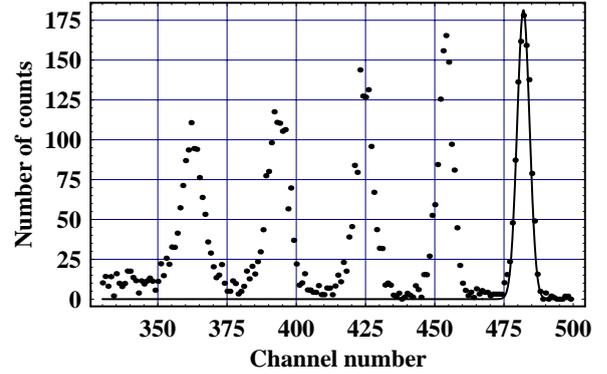
Table 1 summarizes the results of fitting. The parameter σ is a linear function of the channel number in good approximation. Denoting the parameter σ and its peak energy (peak channel) for the Mylar at the beam exit surface by σ_0 and E_0, respectively, the parameter σ at an energy (channel) E is written as

$$\sigma(E) = \sigma_0 \{1 + \alpha(E_0 - E)\} \qquad \text{with} \qquad \alpha = 0.0065. \qquad (3)$$

Table 1: Sammary of the analysis for energy broadening in each peak in Fig. 1

Peak channel number	σ (channel)	σ (realtive)	Peak area (experiment)	Peak area (calculation)
362.0	3.9	1.77	1130 ± 34	1080
393.5	3.5	1.59	1134 ± 34	1080
424.5	3.1	1.41	1140 ± 34	1140
454.0	2.6	1.18	1106 ± 33	1110
482.0	2.2	1.00	1103 ± 33	1020

The calculation of hydrogen concentration $n(x)$ was carried out in the following manner. The exponential decrease is valid for integrated counts of each peak in Fig. 1, and not strictly valid for the spectrum itself. However, if the range of the integration is sufficiently narrow, the decrease of counts in the spectrum can also be approximated by the same exponential function as the integration. Thus the sum energy spectrum was assumed to be

$$Y(E)dE = Q_0 n(x) \exp\{-\mu(d-x)\} dx. \tag{4}$$

Since the sum energy $E(x)$ is a linear function of the depth x, one may express it as

$$E(x) = E_1 + \frac{1}{d}(E_2 - E_1)x, \tag{5}$$

where E_1 and E_2 are the energies at $x = 0$ and $x = d$. Substituting x in the above equation into eq.(4), one may write the exponential part as

$$\exp\{-\mu(d-x)\} = \exp\left\{-\mu \frac{d}{E_2 - E_1} \cdot (E_2 - E)\right\}. \tag{6}$$

The equation (4) reduces to

$$Y(E)dE = Q_0 n(E) \exp\{-\kappa(E_2 - E)\} \cdot \frac{d}{E_2 - E_1} dE, \tag{7}$$

with replacements of $\kappa = \mu d/(E_2 - E_1)$, $dx = \{d/(E_2 - E_1)\}dE$ and $n(x) \to n(E)$.

The experimental sum-energy spectrum is the convolution of the above eq.(7) and the Gaussian distribution with the standard deviation σ given by eq.(3). The explicit form is

$$Y(E)dE = \frac{d}{E_2 - E_1} Q_0$$
$$\times \left[\int_0^\infty n(E') \exp\{-\kappa(E_2 - E')\} \frac{1}{\sqrt{2\pi}\sigma} \exp\left\{-\frac{(E - E')^2}{2\sigma^2}\right\} dE'\right] dE. \tag{8}$$

In this integration, the combination of exponents in two exponential functions and subsequent transformation into a square term after the collection about E' result in a new Gaussian function with a mean value of $\sigma^2\kappa + E$. The calculation results in the following formula;

$$Y(E)dE = \frac{d}{E_2 - E_1} Q_0 \left[\exp\{-\kappa(E_2 - E)\}\right.$$
$$\times \left.\int_0^\infty n(E') \exp\left(\frac{\sigma^2\kappa^2}{2}\right) \frac{1}{\sqrt{2\pi}\sigma} \exp\left\{-\frac{(\sigma^2\kappa + E - E')^2}{2\sigma^2}\right\} dE'\right] dE. \tag{9}$$

The ratio of $d/(E_2 - E_1)$ can be obtained from eq.(5) to be $(dE(x)/dx)^{-1}$, but this is confusing with stopping power. The following notation, therefore, will be used below;

$$\frac{dE(x)}{dx} \longrightarrow \left(\frac{\delta E}{\delta x}\right)_S.$$ (10)

The attached letter "S" means different samples. The final expression for the sum-energy spectrum is given by

$$Y(E)dE = Q_0 \left(\frac{\delta E}{\delta x}\right)_S^{-1} \left[\exp\{-\kappa(E_2 - E)\} \right.$$

$$\left. \times \int_0^\infty n(E') \exp\left(\frac{\sigma^2 \kappa^2}{2}\right) \frac{1}{\sqrt{2\pi}\,\sigma} \exp\left\{-\frac{(\sigma^2\kappa + E - E')^2}{2\sigma^2}\right\} dE' \right] dE.$$ (11)

Numerical calculations of hydrogen concentration $n(x)$ started with the above eq.(11). A raw experimental spectrum was corrected for background suntraction and data smoothing by three-point moving averages. After the correction, the number of counts in each channel was multiplied by $\exp\{\kappa(E_2 - E)\}$, where E_2 was taken to be the highest peak channel number. The energy E was converted to each channel number. The validity of this treatment is easily understood in eq.(11), since $\exp\{-\kappa(E_2 - E)\}$ in the square bracket is independent of the integral variable E'. The number of counts in each channel of this corrected spectrum is written as

$$\hat{N}(E_j) = \exp\{\kappa(E_2 - E)\} Y(E) \Delta E$$

$$= Q_0 \left(\frac{\delta E}{\delta x}\right)_S^{-1} \left[\int_0^\infty n(E') \exp\left(\frac{\sigma^2 \kappa^2}{2}\right) \frac{1}{\sqrt{2\pi}\,\sigma} \exp\left\{-\frac{(\sigma^2\kappa + E_j - E')^2}{2\sigma^2}\right\} dE' \right] \Delta E.$$ (12)

Here, ΔE is the energy corresponding to the width of the window of a pulse height analyzer. The hydrogen concentration $n(E')$ is in general continuous. In the numerical calculation, however, the sample was divided into M thin layers. It was also assumed that the concentration $n(E_i')$ in the i-th layer was constant. Then, the above integration was replaced by the following sum;

$$\left[\sum_{i=1}^M n(E_i') \int_{E_i'}^{E_i' + \Delta E'} \exp\left(\frac{\sigma^2 \kappa^2}{2}\right) \frac{1}{\sqrt{2\pi}\,\sigma} \exp\left\{-\frac{(\sigma^2\kappa + E_j - E')^2}{2\sigma^2}\right\} dE' \right] \Delta E.$$ (13)

Since the above integration is characterized by E_j and E_i', eq.(12) can be expressed as

$$\hat{N}(E_j) \propto \sum_{i=1}^M n(E_i') \Delta E \, F(E_j, E_i'),$$ (14)

where we put the integral simply to $F(E_j, E_i')$. The values of $n(E_i')\Delta E$ were derived from chi-square minimization by Marquardt method[5]. The result is displayed in Fig. 4. The concentration of the lowest peak is split into two parts. Since the number of division is 35 and the thickness of one layer is 6.23 μm, this splitting is too wide in comparison with the thickness of Mylar foils. Two depths corresponding to higher energy peaks shift by 6.7 and 13 μm. In Fig. 5, the spectrum calculated from the extracted hydrogen distribution is compared with the experimental spectrum. The calculated spectrum is in reasonable agreement with the experimental data. The value of chi square is about 250. The number of the data is 138

and the degree of freedom is 131-35=96, so that the chi square is about three times as large as an optimal value of 96. In spite of the shifts of the extracted concentration for higher two peaks, the corresponding peaks in the calculated spectrum exhibit rather good agreement. Further works are necessary although the present analysis is qualitatively reasonable.
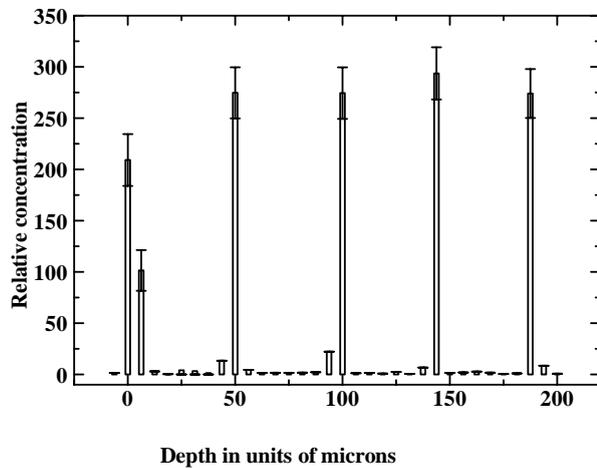
Figure 4: Hydrogen distrubution extracted from the spectrum shown in Fig. 1.
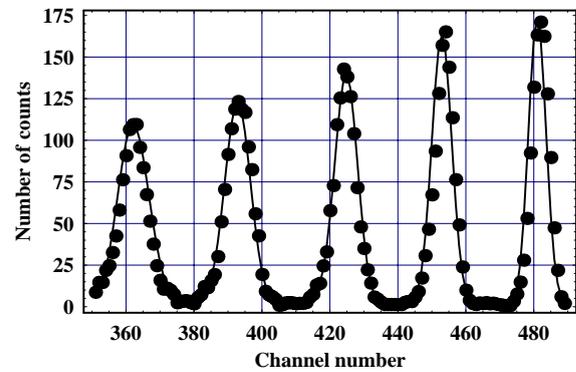
Figure 5: Comparison of the spectrum calculated with the extracted distrubution with the experimental spectrum.

References

[1] K. Furuno, M. Kurosawa, H. Ohsima, T. Komatsubara, K. Sasa, Y. Yamato and N. Kawachi, Measurement of hydrogen concentration in thick mineral or rock samples, Nucl. Instr. and Meth. in Phys. Res. B, (in press).

[2] B.L. Cohen, C.L. Fink, J.H. Degnan, Jour. Appl. Phys. Vol. 43, No.1 (1972) 19-25.

[3] H.C. Hofsäss, N.R. Parkith, M.L. Swanson, W.-K. Chu, Nucl. Instr. Meth. B45 (1990) 151-156.

[4] J.P. Biersack and J.F. Ziegler, Computer code TRIM.

[5] P.R. Bevington and D.K. Robinson, Data Reduction and Error Analysis for the Physical Sciences, 2nd ed., MacGraw-Hill Inc., 1992.

4.4 Development of hydrogen analysis by using proton-proton elastic recoil coincidence method for mineral samples

T. Komatsubara, K. Sasa, H. Oshima, H. Kimura, Y. Tajima, T. Takahashi, S. Ishii, Y. Yamato, M. Ishizuka, T. Kurosawa, K. Furuno

Proton-proton coincidence measurements is one of the quite powerful and convenient methods to analyze hydrogen content with very small radiation damage[1, 2]. Since Cohen[3] developed the method, however, there were very few applications with high energy proton beam. In this report, we will introduce our recent activities which is newly started hydrogen analysis at Tandem Accelerator Center, University of Tsukuba.

When a mineral sample is irradiated by high energy proton beam, the singles spectrum can be very complex including elastic and inelastic scattering with aluminum, oxygen, carbon, silicon and so on. However, the coincidence measurement of two protons can resolve and analyze hydrogen. Singles and coincidence counting rates were typically 2000 and 15 cps, respectively, when a granite sample was irradiated by 20 MeV proton beam with 0.8 nA of beam intensity. The rate of chance coincidence events can be calculated to be 0.2 cps for the 40 ns resolving time.

(1) Hydrogen analysis in granite slices of Motoyasu Bridge

For evaluation of strength of neutron radiation by atomic bomb at Hiroshima, depth profile of ^{152}Eu of residual activities is most important in the granite samples of the Motoyasu Bridge. The bridge is located to be close to the bomb epicenter at Hiroshima. In order to reproduce the depth profile of the activities the atomic ingredient is necessary for the neutron scattering and absorption calculation. However, hydrogen is one of the quite difficult elements for the analysis of content. Previously, Hasai[4] reported the water content by using gravimetric method and Karl Fisher volumetric method. In our present research, proton-proton elastic recoil coincidence measurement has been newly applied to analyze water content.

In the granite samples, major components of minerals are quartz, plagioclase, orthoclase, and biotite. In these components, the biotite is richest for hydrogen in which corresponding water content is about 1.8%wt$^{(H_2O)}$. Furthermore, small amount of chlorite which is metamorphic mineral of biotite exists with more than 5 times of hydrogen content of the biotite. The boundary of the crystal grains may also include some water content which is unknown. Since the hydrogen distribution is not uniform, a number of measurements have been repeated by changing the irradiation positions. As the evaluated water content, the average of all measured results has been calculated.

Thickness of the target slice of granite is 0.2 mm. In Fig. 1, three sample holders are shown. Size of beam spots shown by small circles is 2 mm in diameter. Proton beam of 20 MeV bombarding energy was irradiated with 0.8 nA in the beam current. One measurement has been collected with 500 n Coulomb irradiation. When one measurement was finished, the target holder was moved to change irradiation position and the next irradiation was repeated.

Two Si detectors of 2 mm thick are used. Solid angles of the detectors are 3.4 msr which are defined

by $\phi4$ slits located at 61 mm from the target. In order to reduce edge scattering from the slits buffer slits were located just in front of the Si detectors. Distance from the slit to buffer slit is 66 mm.

As an example of the coincidence measurements, sum-energy spectrum is shown in Fig. 2(a) where the irradiation point could be biotite. In this spectrum, the scattering yield decreases as the energy loss increases, because a secondary scattering occurs when the recoils pass through rest of the sample target. The decreasing yield is calculated by simple exponential function as

$$Y(x) = Y_0 e^{-\mu x}$$

where x denotes distance from exit surface which corresponds to the energy loss. The reduction of the yield can be observed by using mylar foils attached on both entrance and exit surfaces of the granite sample as shown in Fig. 2(c). Since stopping power is rather constant in this energy region, the observed energy loss which is a shift of channels from the high energy edge can be considered as the depth. The coefficient μ' can be calculated as

$$\mu' = \frac{-\log \frac{Y_{in}}{Y_{out}}}{I_{out} - I_{in}}$$

in a unit of [1/channel] where Y_{in} and Y_{out} denote observed yields from the mylar foils of entrance and exit surfaces shown at I_{in} and I_{out} in the Fig. 2(c), respectively. The measured spectrum $Y(I)$ is restored for the reduction of the secondary scattering as shown in Fig. 2(b) by using a formula;

$$Y_{mod}(I) = Y(I) \times e^{\mu'(I_{out}-I)}$$

where a flat distribution of depth profile is observed.

In the following analysis, depth profile is considered as flat. The measured spectra is integrated and multiplied by a factor f;

$$f = \frac{-\log a}{1 - a}$$
$$a = \frac{Y_{in}}{Y_{out}}$$

to correct the secondary scattering.

By changing irradiation positions, 44 measurements have been done in which each irradiation charge of the beam is 5.0×10^{-7} Coulomb. The yield of the coincidence events are widely distributed from a few hundred to the thousands as shown in Fig. 3. Lower part of this distribution can be attributed to quartz. Higher counts can be explained with existence of chlorite. The average of these measurements is 1900 ± 700 counts where the uncertainty is account as $2\,\sigma$ level from consideration of unexpected local concentration of hydrogen.

For the calibration of the scattering yield, standard materials were also irradiated. Measured results are shown in Table 1 where surface densities of corresponding water(H_2O) are shown instead of hydrogen(H).

Calibration factor is determined as 25.7 ± 2.3 counts for 5.0×10^{-7} Coulomb irradiation on 1 μg/cm^2 water content. Reduction factor for the secondary scattering is evaluated to be 2.07 ± 0.04 from the mylar measurements. Surface density of water is deduced as 153 ± 58 μg/cm^2 (H$_2$O). If we use a density of granite reported as 2.64 g/cm^3[4], corresponding water content is evaluated as 0.29 ± 0.11 % wt $^{(H_2O)}$. This result is consistent with previous report[4].

(2) Hydrogen analysis for inclusions in quartz with a micro beam

In geological science, hydrogen analysis of fluid inclusion or glass inclusion in mineral samples is very important for study of magma. Since size of these inclusions are less than several hundred micro meter, nondestructive analysis with micro beam system is quite valuable. The proton proton coincidence spectrometry has been extended by using the micro beam system developed at UTTAC[6] to focus on the inclusions in mineral samples.

For the measurements of the proton proton coincidence, two Si detectors were installed in the focus point of the micro beam facility. Quartz samples of 200 μm in thickness were irradiated. For the detection of the coincidence, the Si detectors of 2mm in thickness are placed at $\pm 45°$ with respect to the beam axis. Defining slits of 3.5 mm in diameter are located in front of the detectors. The distance from the target to the slit is 17.7 mm. Solid angles of the detectors are 30.7 msr. Coincidence time window was adjusted to be 40 nsec by using TAC module.

In order to hold small samples, kapton foils of 1.08$\pm$0.02mg/cm2 (266$\pm$5μg/cm$^{2(H_2O)}$) are used without any glue. Proton yields from the kapton foils are also available for calibration of the scattering yield and correction of the reduction by the secondary scattering.

In Fig. 4, a photograph of a quartz sample is shown. The origin of the quartz sample is Enda, Zao in Fukushima prefecture. Size of the sample is nearly 5mm square and 200 μm in thickness. A glass inclusion of 300 μm in diameter is located nearly the center of the quartz with substructures. The sample is irradiated by a micro beam of 30 μ m in diameter by changing irradiation points. In Fig.5 hydrogen distributions are shown as the results of the irradiation by using micro beam scanning method.

Furthermore, the sample is irradiated by a beam whose spot size is the same as the size of the inclusion. A measured spectrum is shown in Fig. 6 with estimated levels of weight ratio of corresponding water content. The estimated yield corresponding to one weight percent of water content can be calculated as

$$H_{1\%} = \frac{\rho [\text{g/cm}^3] \cdot t [\mu\text{m}] \cdot Y_{out}}{\sigma_{(\text{Kapton})}[\mu\text{g/cm}^2(\text{H}_2\text{O})] \cdot (I_{out} - I_{in})}$$

where ρ and t denote density and thickness of the sample, respectively.

The target position is controlled by a three-axis manipulator. When we measured yield with changing the target position along to the beam axis, strong reduction of the coincidence yield was observed, as shown in Fig. 7. When we move the target about 0.5 mm from the center of the proton detection system, coincidence yield has been reduced to be 80%. When geometrical relation of the detected two protons is considered, the area of the solid angle is estimated to overlap of two circles shown in Fig. 8. The reduction of the detection area is calculated with following formula as a function of z;

$$f = \frac{(\pi - 2|\theta|)r^2 - 2|d|\sqrt{r^2 - d^2}}{\pi r^2}$$

$$\theta = \text{Arcsin} \frac{d}{r}$$

$$d = \frac{z}{\sqrt{2}}$$

where r denote radius of collimator of the detector. The measured value is well reproduced by the calculation which is shown by the solid line in Fig. 7.

References

[1] P. Reichart, G. Dollinger, A. Bergmaier, G. Datzmann, A. Hauptner, H.-J. Körner Nucl. Inst. and Meth. B197 (2002) 134

[2] S.H. Sie, G.F. Suter, A. Chekhmir, T.H. Green, Nucl. Inst. and Meth. B 104 (1995) 261

[3] B.L. Cohen, C.L. Fink, J.H. Degnan, J. Appl. Phys. 43 (1972) 19

[4] H. Hasai, K. Iwatani, K. Shizuma, M. Hoshi, K. Yokoro, S. Sawada, T. Kosako, H. Morishima, Health Phys. 53 (1987) 227

[5] H. Yurimoto, M. Kurosawa, S. Sueno, Geochim Cosmochim Acta 53 (1989) 751

[6] K. Sasa, H. Oshima, Y. Yamato, T. Komatsubara, T. Katabuchi, K. Shima, K. Furuno, M. Kurosawa, N. Yanagisawa, Nucl. Inst. and Meth. B 190 (2002) 287

Table 1 Results of the calibration for the granite sample experiment.

material	thickness [μ m]	H density (weight ratio)	H_2O content [μg/cm^2 (H_2O)]	measured yield for 5.0×10^{-7} C	ratio
polyethylene	30	14.3 %	3030	77751±278	25.6
mylar	5.7	4.2 %	299	7123±38	23.8
mylar	2.5	4.2 %	136	3156±19	23.2
mylar	0.9	4.2 %	48	1362 ± 17	28.4
T-1030[5]	100	15 ppm	3.0	82.7±3.5	27.6
				average	25.7 ± 2.3
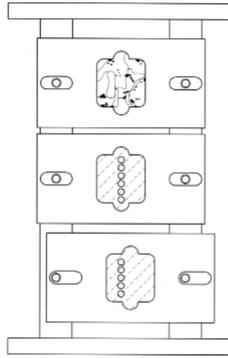
Fig. 1 Three sample holders of granite samples. Irradiation points are shown by small circles.
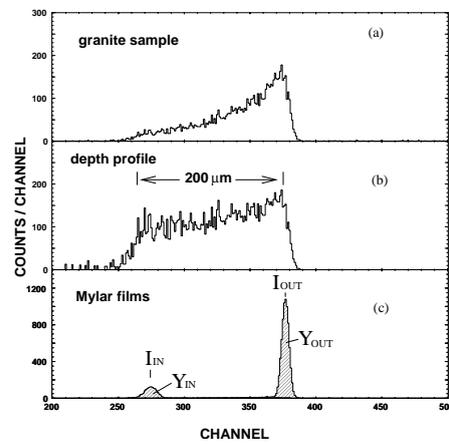
Fig. 2 (a) Sum energy spectrum of the two Si detectors. Irradiation point can be assumed to be biotite. (b) Depth profile modified from the sum energy spectrum. (c) Two peaks from mylar foils attached on entrance and exit surface of the granite.
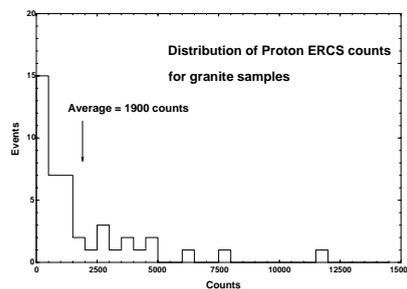
Fig. 3 Distribution of the proton-proton coincidence counts measured for the 44 irradiation points on granite samples.
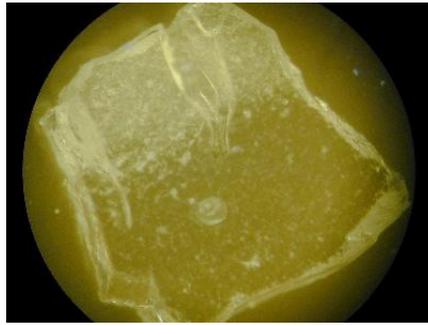
Fig. 4 Picture of quartz sample

Sample : Enda 14

Beam spot : 30 micro m
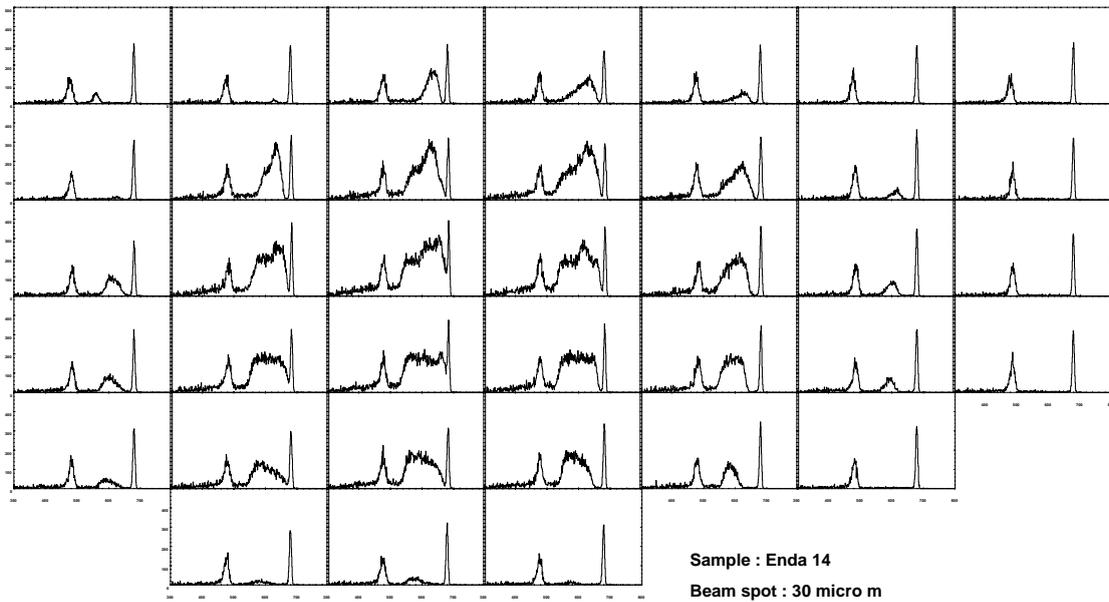
Fig. 5 Depth profiles measured by a micro beam of 30 μ m in diameter.
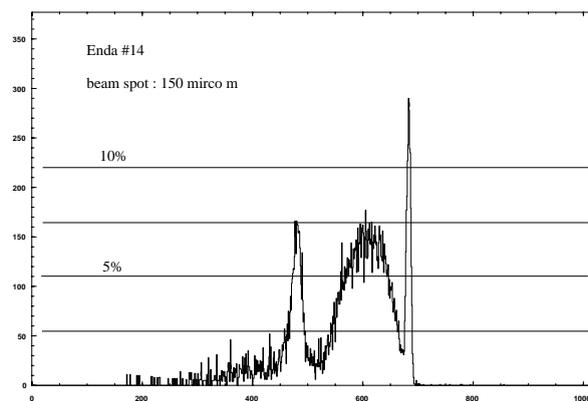
Fig. 6 Measured depth profile for the same sample of Fig. 5 by using 150 μm micro beam. The size of
the beam is nearly same as the glass inclusion. Estimated levels of water content are shown by lines.
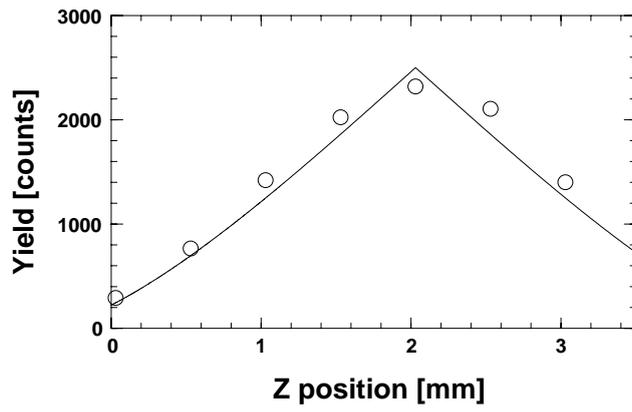
Fig. 7 Z dependence of proton-proton coincidence yield (open circles) and a calculated yield (solid line).
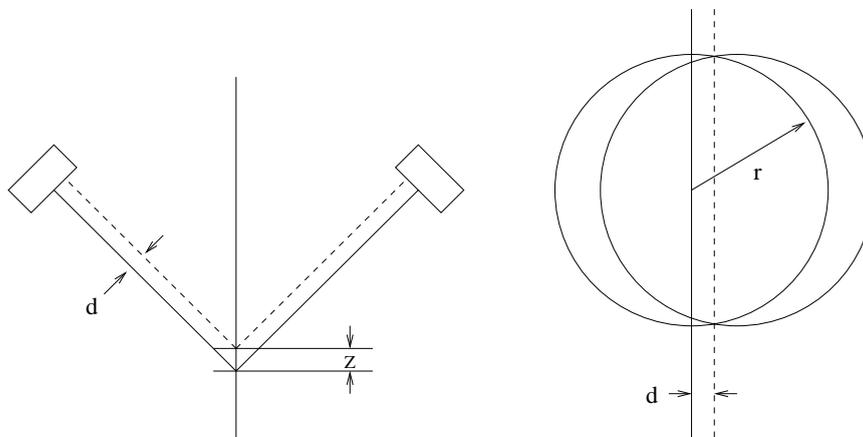
Fig. 8 Schematic view for difference of geometry depending on z position.

4.5　Status of Tsukuba AMS system

Y. Nagashima, R. Seki, T. Takahashi, T. Matsuhiro, K. Sasa, K. Sueki, T. Usui, K. Bessho, H. Matsumura, T. Miura, Q. Wang, and K. Masumoto

The molecular pilot beam method we have developed is a principal of our AMS system. Applying this method to our traditional big, 12MV acceleration voltage, Pelletron tandem accelerator, we have realized successfully an accelerator mass spectrometry (AMS) without any modifications on the tandem system.

In this year, AMS group has made great efforts towards achieving higher precision and reproducibility on the ^{36}Cl measurements as well as several ^{36}Cl AMS measurements. As one of the instrumental improvements, two beam profile monitors are prepared and are going to install into both an exit of an AMS ion-source and the first focus point of an AMS beam line for ^{36}Cl particle detection. The installation work is still going on. These beam profile monitors help us to find the optimum parameters of the optical elements that construct the AMS system and to realize stable ^{36}Cl measurement.

In order to improve the stability of beam transportation in the accelerator, an inner diameter of a charge exchange system at a high-voltage terminal section has been expanded. It was about 5mm in effective diameter. This was too small to get enough stability in beam transportation because the estimated beam diameter is about 7mm at the terminal section. As a preliminary result of the test experiment, it is confirmed that the diameter of it is extended to about 10mm. It is expected that we can see a flattop characteristics with a few mm flat and the reproducibility of the AMS measurements is improved.

A new room for a sample preparation has been opened. A powerful air-conditioning system keeps the room condition dry. Humidity is constantly controlled under 40% even if the rainy season. A small room is constructed in this room. The small room is keeping as clean as possible as well as dry. So, the room has own air-conditioning system and is well shielded. The room air is only ventilated through a ventilator with a HEPA filter system. A filling up in a target holder with samples such as AgCl is performed in this clean room. In order to eliminate contamination at the sample preparation stages, an ultra-pure-water system has been introduced. All of the lab-wares are rinsed with the ultra-pure-water as well as the cleaning with an acid and an alkali solution.

It was estimated that the error of the calculated ^{36}Cl to Cl ratio of the standard material is to be small enough, but we had not yet confirmed. So, this year, we tried to ensure the accuracy of our current standards by comparing with other standards [1]. As a final conclusion of this study, we decided to change a current standard to a new Tsukuba standard with 4.47x10-11 of ^{36}Cl to Cl ratio because it is clearly demonstrated that the current standards have a large error, about 17%.

In order to investigate the influence of nuclear power plants on an environment, ^{36}Cl in soils was continuously studied. The ^{36}Cl is very suitable isotope to see the long-term environmental changes due to such human activities as man made nuclear activities because of both its very long half-life of about 0.3 million years and very low natural abundance less than 10^{-14} in the ratio of ^{36}Cl to ^{35}Cl. In the last year, we

clearly demonstrated that the ratio of ^{36}Cl to ^{35}Cl of Tokai samples are 10 - 100 times as large as that of Tsukuba samples, and that the ratios in the coastal area were much higher than those in the inland area. Many facilities for nuclear research and plant are constructed and are operated in the coastal area of Tokai village, but not so many in the inland area. In order to understand the origin of this high ratio of ^{36}Cl/Cl, we continue to measure the ^{36}Cl contents in many samples taken from Hiroshima, Mie and Fukui prefecture. These samples also contain a lot of Sulfur contamination. We are trying to remove this by several chemical procedures with which we expect high reduction efficiency.

The ^{36}Cl density induced in shielding concretes is going to be measured by the KEK and Tsukuba joint group. Up to now, various shielding concretes that were used in PS counter hall in KEK, in SF cyclotron room in INS, Tokyo University and in LINAC room in LNS, Tohoku University are sampled and measured [2]. The density of ^{36}Cl in the shielding concrete is rather strong because ^{36}Cl has a very long half-life of 3×10^5 year. It is generally too strong to measure by Tsukuba AMS. So, silver-chloride samples are diluted by a suitable amount of ultra pure silver-chloride reagent.

The DS86 dosimetry system has been used for survivors of the Hiroshima and Nagasaki atomic bombs since 1987. In the thermal neutron evaluation, a systematic discrepancy has been observed between ^{152}Eu data measured by Shizuma and Nakanishi and the calculation based on the DS86. As one of the contribution to understand the source of the discrepancy, the measurements of ^{36}Cl in granite samples has been commenced with the Tsukuba AMS system. Seventeen bombed granite samples were chosen and analyzed. These granites are sampled at the location of 146 - 1400m distance from hypo-center. In addition to the bombed granites, 7 un-bombed granite samples were prepared for background estimation because ^{36}Cl was also created in the granite itself as an in-situ formation. Each granite sample was separated into 4 blocks and each block was sent to 4 laboratories. One laboratory at Kanazawa takes the responsibility for ^{152}Eu measurement. Remaining 3 laboratories, Tsukuba, Munchen (Ruehm) and Utah (Straume), bear the responsibility for ^{36}Cl measurement. The ratios of ^{36}Cl to ^{35}Cl of 14 samples have been measured. It seems that there is little discrepancy between the DS86 calculation and the ^{36}Cl measurement. Munchen and Utah have also measured the same samples we measured.

A new dosimetry system named DS02, Dosimetry System 2002, has been developed and released this year [3]. The ^{36}Cl data play very important roles in this development stage. Especially, the ^{36}Cl data clearly settle the systematic discrepancy between ^{152}Eu γ data and DS86 calculation. All of the ^{36}Cl and ^{152}Eu data measured at four laboratories are shown in Fig.1. The results of our ^{36}Cl measurements are consistent with the results of the other three laboratories. And also, the DS02 calculation nicely reproduces the results of four laboratories.

References
[1] T. Matsuhiro, et.al., 3.33, UTTAC (2202).
[2] K.Bessho, et.al., 3.34, UTTAC (2002).
[3] R.Young, et.al., Dosimetry System 2002, (2003), In Press.
[4] Y.Nagashima et.al., Joint Meeting of U.S.-Japan Dosimetry Working Groups, (2001).
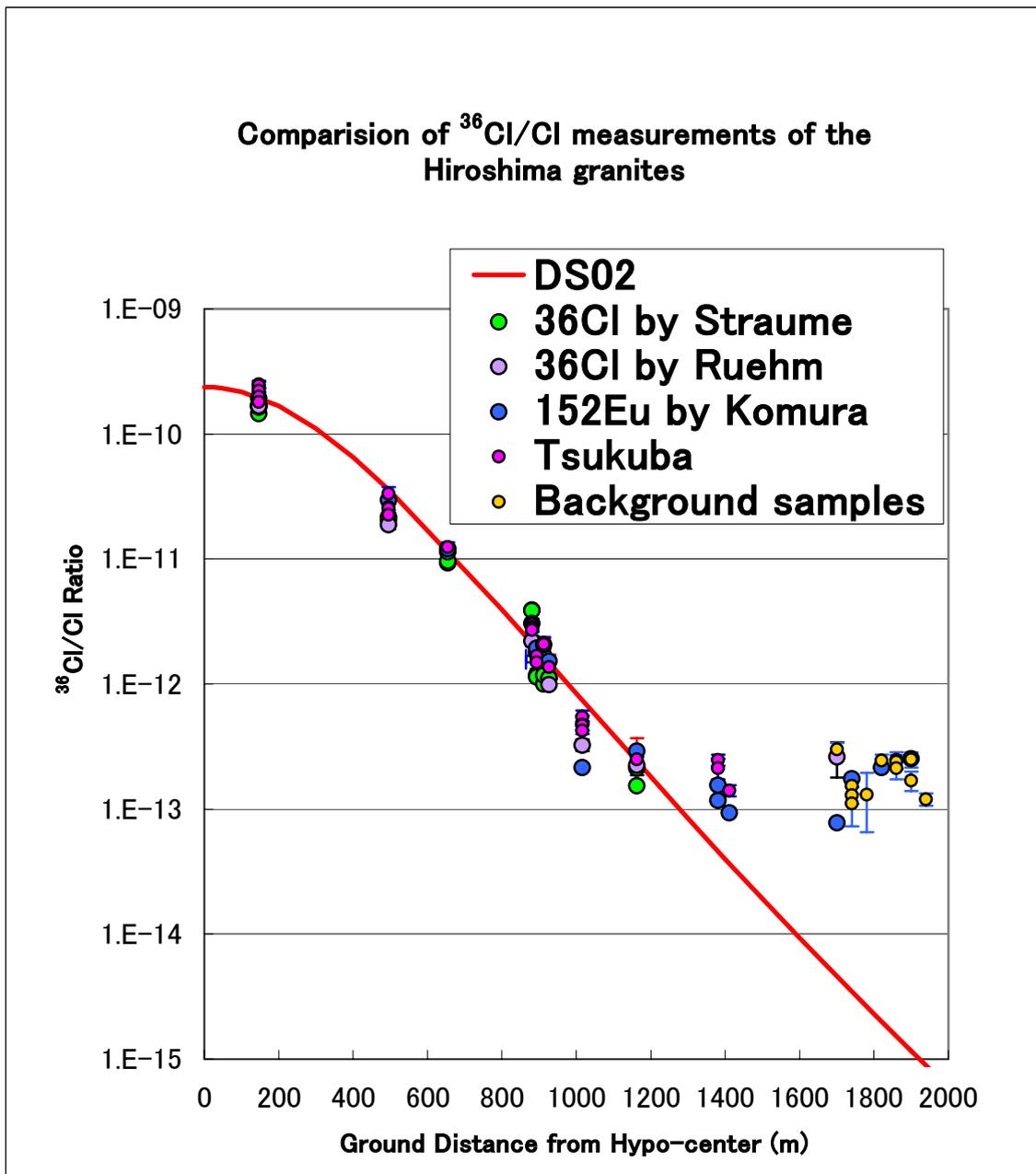
Fig. 1 ^{36}Cl/Cl and ^{152}Eu data measured at four laboratories together with the DS02 calculation, (red line)

4.6 Comparison of Cl-36 standard samples

T. Matsuhiro, R. Seki, Y. Nagashima, T. Takahashi, K. Sasa, K. Sueki, T. Usui, T. Miura[1], K. Bessho[1], H. Matsumura[1], K. Masumoto[1], Q. Wang[1]

A ^{36}Cl standard material plays a very important role in our ^{36}Cl AMS measurements because the Tsukuba AMS system relies strongly on the accuracy of the standard materials to keep a reliability of the ^{36}Cl experimental result. The standard materials we are using were prepared with thermal neutron absorption of ^{35}Cl material. Chrolide-Anmonium reagent, NH_4Cl, was irradiated with neutron in a nuclear reactor of JAERI in 1995 and was diluted with NH_4Cl reagent. The error of the calculated ^{36}Cl to Cl ratio is estimated to be small enough, but we had not yet confirmed it. So, this year, we tried to ensure the accuracy of our current standards by comparing with other standards.

Two kind of new standard materials are prepared for this confirmation. One is the diluted material of a ^{36}Cl standard reference which is distributed commercially from National Institute of Standards and Technology, USA. Another one is the standard samples prepared by Dr. Nishiizum, University of California, Berkley. The Nishiizumi standards are used at more than half of AMS laboratories in the world because the accuracy is well controlled and is keeping high reliable state. These new standards and the current Tsukuba standards are listed in Table 1.

The ^{36}Cl to Cl ratio measurements of the new standards have been alternated with the same measurement of a current one. The ^{36}Cl to Cl ratio of current one is calculated at 1.52×10^{-12}. Therefore, the ratio of the ^{36}Cl to Cl ratio of new one to the same of current one, which is interesting in this study, can be extracted. The results are shown in Fig. 1.

Three kind of the current standard samples, marked with green triangle, are focused on a line of ratio 1. It is difficult to say that the calculated ratios, ^{36}Cl/Cl $= 1.89 \times 10^{-11}$, 1.52×10^{-12} and 1.52×10^{-13}, are absolutely correct, but it is clearly demonstrated that the calculated ration represents the relative ratio between these three standards. On the other hand, all new Tsukuba, red cycles, and Nishiizumi standards, blue rhombs, except one Nishiizumi (^{36}Cl/Cl $= 5.00 \times 10^{-13}$ standard) are well centered on a line of ratio 1.2 (see Fig. 1). It is obvious that there is some difference in ratio estimation between the current standards and the others. In due consideration of the accuracy of Nishiizumi standards, it becomes clear that the calculated ratios of the current standards are overestimated. On the average, the true ^{36}Cl to Cl ratios of the current standards are about 17% smaller than the calculated values.

As a conclusion of the comparison measurements of several ^{36}Cl standards, we decided to change the standard material that is used in the Cl -36 AMS measurement. Both new Tsukuba standards and Nishiizumi standards have no big difference in the accuracy of ^{36}Cl/Cl ratio estimation. So, as a new current standard, the new Tsukuba standard having 4.47×10^{-11} value of the ^{36}Cl to Cl ratio has been selected. Furthermore, in order to ensure the accuracy of the current standard, comparison measurement of the current standard and the Nishiizumi standard with the ratio of 1.00×10^{-11} will be regularly scheduled.

---

[1] High Energy Accelerator Research Organization

Table 1   The estimated ratios of ^{36}Cl to Cl for the ^{36}Cl standard samples.

| Tsukuba Standard samples (Current)	Tsukuba standard samples (New)	Standard samples (Nishiizumi)
1.89×10^{-11}	4.47×10^{-11}	1.00×10^{-11}
1.52×10^{-12}	4.94×10^{-12}	5.00×10^{-12}
1.52×10^{-13}	2.61×10^{-13}	1.60×10^{-12}
		5.00×10^{-13}
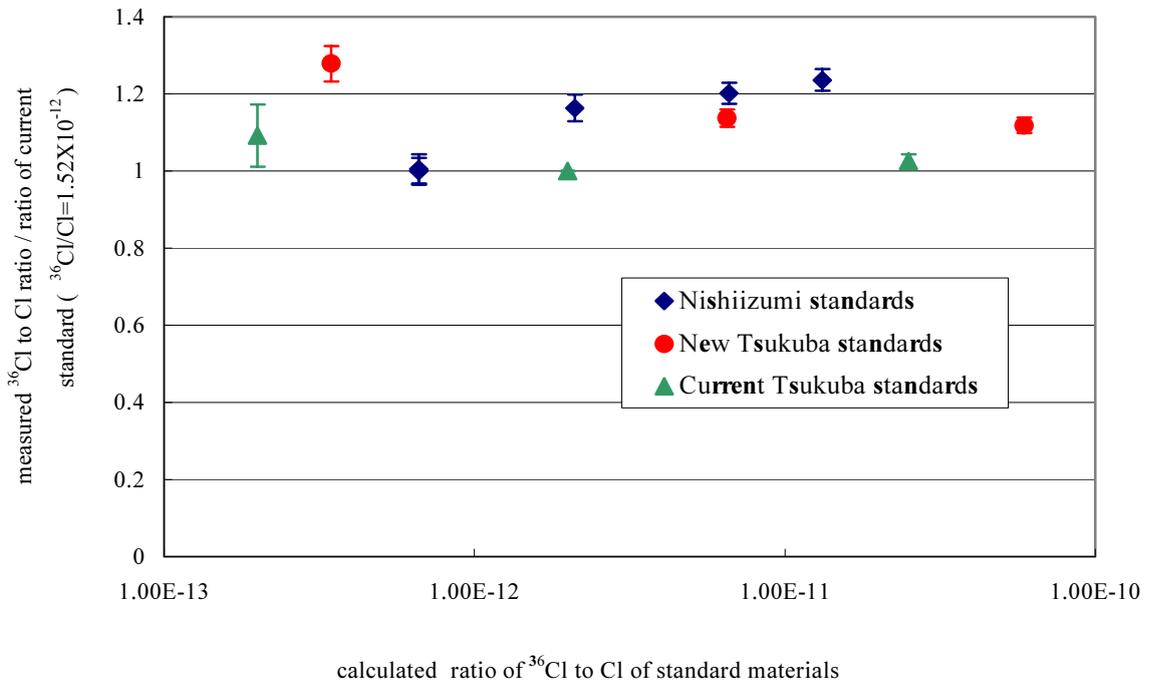
Fig.1   Comparison of ^{36}Cl standard samples. Ratio of measured to calculated value of standard samples   (measurement 2002.12.9)

4.7　Measurement of ^{36}Cl induced in shielding concrete of various accelerator facilities using AMS

K. Bessho[1], H. Matsumura[1], T. Miura[1], Q. Wang[1], K. Masumoto[1], T. Matsuhiro, Y. Nagashima, R. Seki, T. Takahashi, K. Sasa, T. Usui and K. Sueki

At the accelerator facilities, shielding concrete of beam lines is exposed to secondary neutron, and various long-lived radionuclides, such as ^{3}H, ^{22}Na, ^{36}Cl, ^{54}Mn, ^{60}Co, ^{152}Eu and ^{154}Eu are accumulated. Quantitative evaluation of radionuclides induced in the shielding concrete is important for radioactive waste management in reconstruction or decommissioning of accelerator facilities.　The above radionuclides except for ^{36}Cl can be easily measured by Ge detectors for γ-emitters and liquid scintillation counters for ^{3}H, respectively [1].　On the other hand for measuring low concentration of ^{36}Cl, accelerator mass spectrometry (AMS) is advantageous because of extremely high sensitivity.

The AMS system constructed in the 12UD tandem accelerator of UTTAC has been applied to ^{36}Cl analysis in soil and concrete samples related to Hiroshima atomic bomb, JCO critical accident, and other environmental samples.　Chemical procedure for preparing an AgCl target has been investigated and established [2].　However, ^{36}Cl / ^{35}Cl ratios in shielding concrete of various accelerators are considered to be higher than the appropriate range for the UTTAC ^{36}Cl AMS system (10^{-10} - 10^{-13}).　Therefore, dilution of isotope ratios is necessary for ^{36}Cl analysis in shielding concrete samples by the UTTAC AMS system.　Fig. 1 shows the sample preparation scheme developed for ^{36}Cl AMS measurement of shielding concrete.　A part of Cl contained in concrete samples was extracted into dilute nitric acid by heating in pressurized decomposition vessel, and the concentration of the eluted Cl in the solution was determined by ion chromatography.　The ^{36}Cl / ^{35}Cl ratios were diluted by addition of ^{36}Cl free (^{36}Cl / ^{35}Cl below 5×10^{-14}) NaCl solution.　Precipitation of AgCl was formed by addition of AgNO$_3$ solution and purified according to the method developed [2].
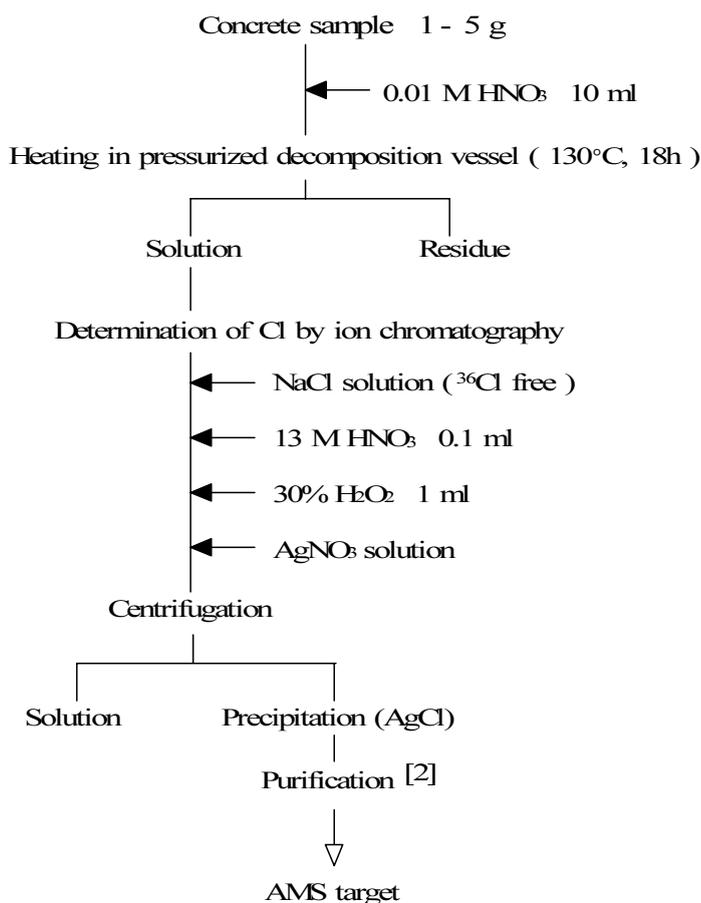
Fig. 1　Sample preparation scheme for ^{36}Cl AMS measument of shielding concrete of accelerators.

Amount of the concrete sufficient for the sample preparation is 1 - 5 g, which is much smaller than the conventional method (100 g or more) [2]. Reliability of the procedure was proved by reproducibility of the analytical results and independence of determined ^{36}Cl / ^{35}Cl ratios of original samples (before dilution) on diluting isotope ratios.

For three kinds of accelerator facilities, SF cyclotron (Center for Nuclear Study, the University of Tokyo), 300 MeV electron LINAC (Laboratory of Nuclear Science, Tohoku University), and 12 GeV proton synchrotron (High Energy Accelerator Research Organization), the depth profiles of ^{36}Cl / ^{35}Cl ratios in shielding concrete of beam lines were analyzed. Figs. 2(a) and (b) show the depth profiles of ^{36}Cl / ^{35}Cl ratios together with the specific radioactivity of ^{152}Eu and ^{60}Co in the shielding concrete of SF cyclotron and 300 MeV electron LINAC, respectively. The depth profiles of ^{36}Cl / ^{35}Cl are in good agreement with those of ^{152}Eu and ^{60}Co, which are formed by thermal neutron capture reactions. The maximum ^{36}Cl / ^{35}Cl ratios were observed at about 10 cm in depth from the inside surface, and similar depth profiles were observed for 12 GeV proton synchrotron. These results imply that ^{36}Cl formed in shielding concrete of these accelerators is mainly formed by thermal neutron capture of ^{35}Cl. The maximum ^{36}Cl / ^{35}Cl ratio of 3x10^{-8} (300 MeV electron LINAC, depth of 8cm) corresponds to the specific radioactivity of 3x10^{-3} Bq/g, which is not important for radioactive waste management in reconstruction or decommissioning of accelerator facilities, compared with specific radioactivity of ^{3}H, ^{152}Eu and ^{60}Co.

References

[1] T. Miura, K. Bessho, S. Ishihama and N. Ohtsuka, J. Radioanal. Nucl. Chem., 255(2003)543-546
[2] Y. Nagashima, R. Seki, T. Takahashi and D. Arai, Nucl. Instr. Meth. B172(2000)129-133
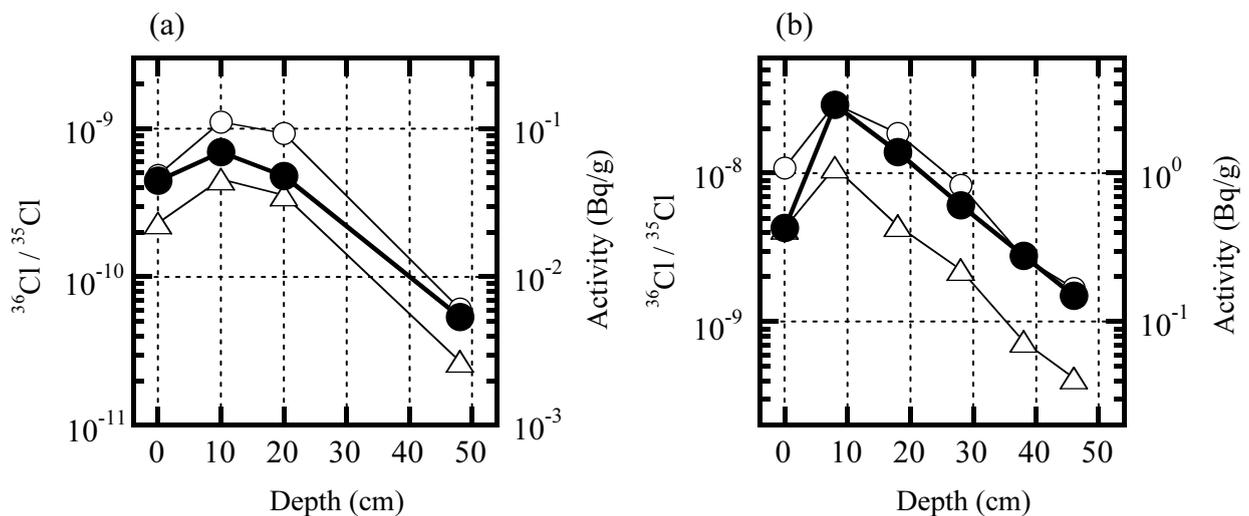
Fig. 2   Depth profiles of ^{36}Cl / ^{35}Cl ratios and specific radioactivity of ^{152}Eu and ^{60}Co induced in the shielding concrete of   (a) SF cyclotron (Center for Nuclear Study, the University of Tokyo) and   (b) 300 MeV electron LINAC (Laboratory of Nuclear Science, Tohoku University) .

● ^{36}Cl / ^{35}Cl   ○ ^{152}Eu   △ ^{60}Co

5. LIST OF PUBLICATIONS

NUCLEAR PHYSICS – EXPERIMENT

Y.H. Zhang, Y.J. Ma, Y. Sasaki, K. Yamada, H. Ohshima, S. Yokose, M. Ishizuka, T. Komatsubara, K. Furuno, A new level scheme of I-127 High Energy Physics and Nuclear Physics-Chinese Edition 26 (2): 104-107 (2002)

Y.H. Zhang, T. Hayakawa, M. Oshima, J. Katakura, Y. Hatsukawa, M. Matsuda, H. Kusakari, M. Sugawara, T. Komatsubara, K. Furuno, Experimental study of high-spin states in deformed odd-odd Ir-180 High Energy Physics and Nuclear Physics-Chinese Edition 26 (6): 582-588 (2002)

C.B. Moon, T. Komatsubara, Y. Sasaki, T. Jumatsu, K. Yamada, K. Satou, K. Furuno, Signature inversion in the yrare band of Xe-119 Eur.Phys.J. A 14, 13-16 (2002)

J.H. Ha, J.C. Kim, C.S. Lee, J.H. Lee, J.Y. Huh, C.B. Moon, S.J. Chae, K. Furuno, T. Komatsubara, T. Schizuma, K. Matsuura, K. Kato, Y. Sadaki, H. Ishiyama, Y. Gono, T. Morikawa, S. Mitarai, M. Shibata, H. Watanabe, M. Miyake, E. Komatsu, A. Odahara, E. Ideguchi, X.H. Zhou, High-spin states in odd-odd Lu-168 Journal of the Physical Society of Japan 71 (7):1663-1671 (2002)

C.B. Moon, S.J. Chae, J.H. Ha, T. Komatsubara, Y. Sasaki, T. Jumatsu, K. Yamada, K. Satou, K. Furuno, Signature anomaly in the yrare band of Xe-119 Journal of the Korean Physical Society 41 (2): 188-194 (2002)

Y.H. Zhang, F.R. Xu, J.J. He, Z. Liu, X.H. Zhou, Z.G. Gan, T. Hayakawa, M. Oshima, T. Toh, T. Shizuma, J. Katakura, Y. Hatsukawa, M. Matsuda, H. Kusakari, M. Sugawara, K. Furuno, T. Komatsubara, T. Une, S.X. Wen, Z.M. Wang Signature Inversion Phenomena in Odd-Odd ^{1}82Au Eur.Phys.J. A 14, 271-274 (2002)

Z. Liu, Y.H. Zhang, Y.J. Ma, Y. Sasaki, K. Yamada, H. Oshima, S. Yokose, M. Ishizuka, T. Komatsubara, K. Furuno High Energy Physics and Nuclear Physics-Chinese Edition 26 (12): High-spin states of the neutron-rich nucleus Sb-125 1195-1200 Dec (2002)

N. Kawachi, T. Katabuchi, M. Yamaguchi and Y. Tagishi Real-time measurement of implanted deuterons by using the nuclear reaction ^{2}H(d,p)^{3}H, Nuclear Inst. and Methods in Physics Research, B 190, 195-198, 2002

S. Hirowatati, Syafarudin, F.Aramaki, A.Nohtomi, G. Wakabayashi, Y. Uozumi, N. Ikeda, M. Matoba, Y. Aoki, K. Hirota, N. Okumura, T.Joh, ^{100}Mo($\vec{p}$,d)^{99}Mo reaction at 21 MeV and direct reaction analysis of the low-lying continuum spectrum, Nucl. Phys. A714, 3-20 page , (2003)

HIGH ENERGY NUCLEAR PHYSICS

K. Adcox, S. Esumi, Y. Miake, et.al., Centrality Dependence of π^+/π^-, K^+/K^-, P and anti-P production from $\sqrt{s_{NN}}$ = 130-GeV Au+Au Collisions at RHIC, Phys. Rev. Lett. 88: 242301, 2002

M.M. Aggarwal, Y. Miake, et.al., Event-by-Event Fluctuations in Particle Multiplicities and Transverse Energy Produced in 158-A-GeV Pb+Pb Collisions, Phys. Rev. C65: 054912, 2002

K. Adcox, S. Esumi, Y. Miake, et.al., Measurement of the Lambda and Anti-Lambda Particles in Au+Au Collisions at $\sqrt{s_{NN}}$ = 130-GeV, Phys. Rev. Lett. 89: 092302, 2002

L. Ahle, Y. Miake, et.al., System, Centrality, and Transverse Mass Dependence of Two Pion Correlation Radii in Heavy Ion Collisions at 11.6-A-GeV and 14.6-A-GeV, Phys. Rev. C66: 054906, 2002

K. Adcox, S. Esumi, Y. Miake, et.al., Event-by-Event Fluctuations in Mean P(t) and Mean E(t) in $\sqrt{s_{NN}}$ = 130-GeV Au+Au Collisions, Phys. Rev. C66: 024901, 2002

K. Adcox, S. Esumi, Y. Miake, et.al., Net Charge Fluctuations in Au+Au Interactions at $\sqrt{s}$ = 130-GeV, Phys. Rev. Lett. 89: 082301, 2002

K. Adcox, S. Esumi, Y. Miake, et.al., Measurement of Single Electrons and Implications for Charm Production in Au+Au Collisions at $\sqrt{s_{NN}}$ = 130-GeV, Phys. Rev. Lett. 88: 192303, 2002

K. Adcox, S. Esumi, Y. Miake, et.al., Transverse Mass Dependence of Two Pion Correlations in Au+Au Collisions at $\sqrt{s_{NN}}$ = 130-GeV, Phys. Rev. Lett. 88: 192302, 2002

M. M. Aggarwal, Y. Miake et.al., One, Two, and Three Particle Distributions from 158-A-GeV/c Central Pb+Pb Collisions, Phys. Rev. C67: 014906, 2003

I. G. Bearden, S. Esumi, et.al., Particle Production in Central Pb+Pb Collisions at 158-A-GeV/c, Phys. Rev. C66: 044907, 2002

I.G. Bearden, S. Esumi, et.al., Deuteron and Triton Production with High Energy Sulphur and Lead Beams, Eur. Phys. J. C23: 237-247, 2002

D. Adamova, S. Esumi, et.al., Universal Pion Freezeout in Heavy Ion Collisions, Phys. Rev. Lett. 90: 022301, 2003

D. Adamova, S. Esumi, et.al., Beam Energy and Centrality Dependence of Two Pion Bose-Einstein Correlations at SPS Energies, Nucl. Phys. A714: 124-144, 2003

ATOMIC AND SOLID STATE PHYSICS, AND CLUSTER SCIENCE

H. Kudo, K. Takeda, T. Suguri, W. Iwazaki, C. Sakurai, I. Arano, S. Numazawa and S. Seki, Electron loss from fast partially stripped C and O ions incident on crystal targets, Nuclear Instruments and Methods in Physics Research Section B 207 pp.283-290 (2003)

M. Onoda and J. Hasegawa, The spin-gap state and the phase transition in the δ-phase $Tl_xV_2O_5$ polaronic bronze, Journal of Physics: Condensed Matter, Vol. 14, No. 19, pp. 5045-5059 (2002)

N. Nishiguchi, M. Onoda and K. Kubo, Superexchange interactions in the two-dimensional $S = \frac{1}{2}$ system MV_3O_7, Journal of Physics: Condensed Matter, Vol. 14, No. 23, pp. 5731-5746 (2002)

N. Nishiguchi and M. Onoda, A pseudotetramer in the geometrically frustrated spinel system CdV_2O_4, Journal of Physics: Condensed Matter, Vol. 14, No. 28, pp. L551-L557 (2002)

M. Onoda and J. Hasegawa, A distortion of pseudotetramers coupled with the Jahn-Teller effect in the geometrically frustrated spinel system CdV_2O_4, Journal of Physics: Condensed Matter, Vol. 15, No. 3, pp. L95-L102 (2003) *IOP SELECT*

S. Sakai, H. Tanimoto, E. Kita and H. Mizubayashi, Characteristic Creep Behavior of Nanocrystalline (n-) Metals Found for High Density n-Gold, Phys. Rev. B, 66(2002), 214106 (9 pages)

H. Tanimoto, S. Sakai and H. Mizubayashi, Anelasticity Study on Motions of Atoms in the Grain Boundary Regions in Nanocrystalline Gold, Mater. Trans., 44 (2003) pp.53-58

H. Tanimoto, S. Sakai, E. Kita and H. Mizubayashi, Characterization and Elastic Property of High-Density Nanocrystalline Gold Prepared by Gas-Deposition Method, Mater. Trans., 44(2003) pp.94-103

M. Imanaka, T. Kurita, M. Tsukada, I. Arai, S. M. Lee, and T. Nakagawa, Effect of a biased electrode on operation of ECR ion source using liquid He freesuperconduction solenoid coils, Rev. Sci. Instrum. 73, (2002) 592

T. Nakagawa, T. Kurita, M. Kidera, M. Imanaka, Y. Higurashi, M. Tsukada, S. M. Lee, M. Kase, and Y. Yano, Intense beam production from RIKEN 18 GHz ECRIS and liquid He free SC-ECRISs, Rev. Sci. Instrum. 73, (2002) 513

M. Imanaka, T. Kurita, T. Nakagawa, H. Sasaki, S.G. Lee, I. Arai and S.M. Lee, Highly-charged Ion beam for study of cluster physics, Transactions of MRS-J, 27, (2002) 181

I. Arai, H. Sasaki, J. Hirose, K. Teranishi and S.M. Lee, Abundance Spectra of Clusters for Various Metals in Sputtering and Their Formation Mechanism, Transactions of the Materials Research Society of Japan, 27, (2002) 193

M. Imanaka, T. Kurita, M. Tukada, T. Nakagawa, M. Kidera and S.M. Lee, Effect of Magnetic Field Strength on Beam Intensity of Highly Charged Xe. Ions from Liquid-He-Free Superconducting ECR Ion Source, Jpn. J. Appl. Phys. 41, 6A, (2002) 3926

T. Kurita, M. Imanaka, M. Tsukada, T. Nakagawa, M. Kidera, I. Arai and S.M. Lee, Performance of an ECR ion source using liquid-helium-free superconducting solenoid coils (SHIVA), Nucl. Instrum. Methods Phys. Res. B192, (2002) 429

H. Arai, M. Imanaka, S.M. Lee, Y. Higurashi, T. Nakagawa, M. Kidera, T. Kageyama, M. Kase, Y. Yano and T. Aihara, Effect of minimum strength of mirror magnetic field (Bmin) on production of highly charged heavy ions from RIKEN liquid-He-free superconducting electron cyclotron resonance ion source (RAMSES), Nucl. Instrum. Methods Phys. Res. A491 (2002) 9-41

T.X. Li, S.M. Lee, S.J. Han and G.H. Wang, Structural transitions of Au55 isomers, Phys. Lett. A, Vol.300, (2002) 86

T. Matsuhiro, Cl-36 Measurements of Hiroshima A-Bombed Granites, Proceedings of the Third Workshop on Environmental Radioactivity, KEK-Proceedings 2002-7, pp.69-73 (2002)

K. Sasa, H. Ohshima, Y. Yamato, T. Komatsubara, T. Katabuchi, K. Shima, K. Furuno, M. Kurosawa, N. Yanagisawa, Hydrogen analysis of mineral samples at University of Tsukuba Nucl. Inst. Meth. B 190: 287-290 (2002)

6. THESES

Ph. D. Theses

| Naoki Kawachi | Real-time measurement of implanted deuterium density by using the ^{2}H(d,p)^{3}H reaction |
| Mitsutaka Yamaguchi | Measurement of Proton Polarization in ^{208}Pb(d,p)^{209}Pb Reaction at Incident Deuteron Energy of 20 MeV |

M. Sc. Theses

Makoto Ishizuka	Developement of Standard Samples for Hydrogen Analysis by using Resonance Nuclear Reactions
Kouichi Teranishi	Production of Clusters from Low Melting Temterature Metals by Xe Atom Sputtering
Masatoshi Tsukada	Diagnostics of Plasma in ECR Ion Source by Laser Ablation Method
Hiroshi Masui	Elliptic Azimuthal Anisotropies of High pT Particles in Au+Au collsions $\sqrt{s_{NN}} = 200$ GeV
Shingo Sakai	Elliptic Azimuthal Anisotropies of pions, kaons and protons in Au+Au collsions at $\sqrt{s_{NN}} = 200$ GeV
Yoshiaki Kuroki	Directed Azimuthal Anisotropies of Particle Production in Au+Au collsions at $\sqrt{s_{NN}} = 200$ GeV
Wataru Iwazaki	Secondary Electron Emission from Solids Bombarded by Fast Clusters
Takuya Suguri	Low-Energy Electron Emissionfrom Solids by Fast Heavy Ion Impact
Isamu Arano	Observation of Distorted Crystal Lattices with Ion-Induced Electron Spectroscopy
Shuhei Numazawa	Analysis of H and D Contents in Synthesized Polymer Films
Chizuko Sakurai	Binary-Encounter Electron Emission by Grazingly Incident Ions
Kazuhiko Sekine	NMR for the composite crystal $Cu_xV_4O_{11}$ and the application to the secondary ion battery

7. SEMINARS

Date		Speaker and Title
2002		
May	23	Hans Paetz gen. Schieck (Univ. of Koln, Germany); Few-Body Research Programme at the Cologne FN Tandem Accelerator
June	31	Y. H. Zhang (Institute of Modern Physics, Lanzhou); Study of Semi-Decoupled Bands in odd-odd Nuclei
		X. H. Zhou (Institute of Modern Physics, Lanzhou); Brief Introduction on the Identification of New Isotopes at IMP and Level Structure Study of ^{169}Re
Sept.	25	Jiang Shan (China Institute of Atomic Energy); ^{41}Ca & ^{36}Cl Measurements and their Applications
Oct.	10	M. Kamimura (Kyushu Univ.); The Latest Determination of Antiproton Mass by Precision 3-body Calculation of Antiprotonic Helium Atoms
Nov.	6	H. Ishiyama (KEK); Direct Measurement of (α, n) Reaction Cross Sections using Light Neutron-Rich Radioactive Beams
Dec.	11	M. Tsukada (Univ. of Tsukuba); Diagnostics of Plasma in ECR Ion Source by Laser Ablation Method
		K. Teranishi (Univ. of Tsukuba); Production of Clusters from Low Melting Temterature Metals by Xe Atom Sputtering
Dec.	18	M. Ishizuka (Univ. of Tsukuba); Developement of Standard Samples for Hydrogen Analysis by using Resonance Nuclear Reactions
		H. Masui (Univ. of Tsukuba); Elliptic Azimuthal Anisotropies of High pT Particles in Au+Au collsions $\sqrt{s_{NN}} = 200$ GeV
Dec.	25	M. Imanaka (Univ. of Tsukuba); Effect of Magnetic Field Configuration on the Plasma of Liquid-He-Free Superconducting ECR Ion Source
2003		
Jan.	15	Y. Kuroki (Univ. of Tsukuba); Study of Azimuthal Directed Anisotropy of Charged Particle Emission in $\sqrt{s_{NN}} = 200$GeV Au+Au Collisions
		S. Sakai (Univ. of Tsukuba); Azimuthal Anisotropy of pions, kaons and protons Emission in $\sqrt{s_{NN}} = 200$GeV Au+Au Collisions
Feb.	19	S. Takeuchi (JAERI); Development of Accelerating System for JAERI-Tandem Accelerator
March	7	K. Sagara (Kyushu Univ.); Experimental and Theoretical Aspects for Three Nucleon System
March	19	M. Igashira (Tokyo Institute of Technology); Fast-Neutron Capture by Light Nuclei relevant to Nucleosynthesis in the Universe

8. SYMPOSIUM

<div align="center">

**Workshop on Nuclear Synthesis
and Radiactive Nuclei**
3rd July 2002
Tandem Accelerator Center, University of Tsukuba

</div>

Openning address, *K. Furuno (Univ. of Tsukuba)*
Present Status and Perspective of Nucleosynthesis Studies – New Paradigm in Cosmology and Nucleosynthesis –, *T. Kajino (National Astronomical Observatory of Japan)*
Perspectives of Nuclear Synthesis by using Accelerators, *S. Kubono (CNS, Univ. of Tokyo)*
Nuclear Structure with Radiactive Nuclei, *K. Yabana (Univ. of Tsukuba)*
Future Plans of RI Beam Factory, *T. Suda (RIKEN)*
A KEK-JAERI RNB Facility Project and Recent RNB Experimental Works at JAERI-Tandem, *H. Miyatake (KEK)*
Reaserches on Unstable Nuclear Structure at RIKEN, *A. Ozawa (RIKEN)*
Study on Nuclear Symthesis at RIKEN, *S. Nishimura (RIKEN)*
Coulomb Break Up and CDCC, *Y. Aoki (Univ. of Tsukuba)*
Study of Unstable Nuclear Structure with Transition Magnetic Field, *T. Komatsubara (Univ. of Tsukuba)*
Study of p-precess at Supernova, *T. Hayakawa (JAERI)*
Study of High Spin States by using Low Energy Secondary RI Beam, *E. Ideguchi (RIKEN)*
Nuclear Physics conbind with RI Beam Factory and Tandem van de Graaff, *I. Tanihata (RIKEN)*

9. LIST OF PERSONEL

Accelerator Center

K. Furuno	Director, Professor
K. Shima	Associate Professor
T. Komatsubara	Assistant Professor
K. Sasa	Assistant Professor
S. Ishii	Mechanical Technician
H. Kimura	Computer Technician
H. Oshima	Electric Technician
Y. Tajima	Mechanical Technician
T. Takahashi	Electric Technician
Y. Yamato	Electric Technician
T.X. Li	Research Fellow
K. Taga	Administrative Stuff

Steering Committee

K. Furuno	Chairperson, Tandem Accelerator Center
Y. Kajiwara	Inst. of Geoscience
R. Kanzaki	Inst. of Biological Science
T. Komatsubara	Tandem Accelerator Center
H. Kudo	Inst. of Applied Physics
Y. Miake	Inst. of Physics
M. Onoda	Inst. of Physics
R. Seki	Inst. of Chemistry
K. Shima	Inst. of Applied Physics
Y. Tagishi	Inst. of Physics
K. Yabana	Inst. of Physics
K. Yasuoka	Inst. of Physics

Scientific Guests and Fellows

K. Awazu	National Lab. Advanced Industrial Science and Technology
M. Fujimaki	Waseda Univ.
K. Nomura	Waseda Univ.
Y. Nagasawa	Waseda Univ.
N. Horikawa	Nagoya Univ.
I. Daito	Nagoya Univ.
T. Inagaki	Nagoya Univ.
T. Kobayashi	Nagoya Univ.
Li Wang	Nagoya Univ.
M. Iio	Nagoya Univ.
T. Mizota	Tsukuba Nano-Tech.
H. Ishiyama	KEK
H. Miyatake	KEK
M. Tanaka	KEK
M. Yoshikawa	KEK
S.C. Jeong	KEK
T. Miura	KEK
K. Masumoto	KEK
K. Bessho	KEK
H. Muramatsu	KEK

Q.B. Wang	KEK
Y. Watanabe	KEK
He Ming	China Institute of Atomic Energy
Jiang Shan	China Institute of Atomic Energy
Y. H. Zhang	Institute of Modern Physics, Lanzhou
X. H. Zhou	Institute of Modern Physics, Lanzhou

Research Members
Inst. of Physics

Y. Aoki	I. Arai	S. Esumi	K. Furuno	S. Katoh
T. Komatsubara	S.M. Lee	Y. Miake	N. Okumura	M. Onoda
K. Sasa	Y. Tagishi	T. Une		

Inst. of Applied Physics

| K. Akimoto | E. Kita | H. Kudo | T. Murakami | K. Shima |
| A. Uedono | | | | |

Inst. of Material Science

| H. Ikeda | T. Koyano | H. Mizubayashi | K. Takita | H. Tanimoto |
| R. Yoshizaki | | | | |

Inst. of Geoscience

| R. Anma | T. Katou | M. Kurosawa | M. Sugita |

Inst. of Chemistry

| R. Seki | K. Sueki |

Inst. of Basic Medical Science

Y. Nagashima

Tandem Accelerator Center

T.X. Li

Graduate Students
Doctoral Degree Programs of Physics

| J. Hasegawa | M. Imanaka | N. Kawachi | S.G. Lee | K. Satoh |
| M. Yamaguchi | | | | |

Doctoral Degree Programs of Engineering

| T. Hao | B. Hou | N. Ookubo | N. Umeda |

Doctoral Degree Programs of Pure and Applied Science

A. Hatanaka	T. Harigae	T. Ikeda	W. Iwasaki	M. Konno
H. Masui	M. Nakazumi	M. Nagata	S. Sakai	H. Sasaki
J. Sawahata	K. Sekine	M. Shimomura	T. Suguri	T. Suzuki
S. Takagi	H. Tokano	H. Tsuruoka	N. Yagi	T. Yamada

Doctoral Degree Programs of Agriculture Science

S. Kaburagi

Master's Degree Programs of Science and Engineering

H. Arai	I. Arano	T. Handa	H. Ishiguro	M. Ishizuka
S. Kaminaga	K. Kondo	M. Kubo	Y. Kuroki	T. Matsuura
S. Miyasaka	T. Muto	T. Nomiyama	S. Numazawa	T. Ooki
C. Sakurai	H. Sato	Y. Takanashi	K. Teranishi	N. Yoshimaru

Master's Degree Programs of Education

T. Tsukada

Master's Degree Programs of Environmental Science

T. Matsuhiro

Under Graduates

Y. Goto	S. Hamajima	T. Himuma	Y. Ishibashi	T. Kawagishi
K. Kitazato	H. Kobai	N. Matsuda	Y. Nagata	T. Shimada
T. Shojo	T. Suzuki	A. Ueki	T. Usui	